University of Wollongong
Research Online

University of Wollongong Thesis Collection 2017+
University of Wollongong Thesis Collections

2018

High Resolution Radiation Therapy Dosimetry in Magnetic Fields using Novel Silicon Array Dosimeters: A Pilot for MRI-linac Applications

Maegan A. Gargett
University of Wollongong

Follow this and additional works at: https://ro.uow.edu.au/theses1

University of Wollongong

Copyright Warning

You may print or download ONE copy of this document for the purpose of your own research or study. The University does not authorise you to copy, communicate or otherwise make available electronically to any other person any copyright material contained on this site.

You are reminded of the following: This work is copyright. Apart from any use permitted under the Copyright Act 1968, no part of this work may be reproduced by any process, nor may any other exclusive right be exercised, without the permission of the author. Copyright owners are entitled to take legal action against persons who infringe their copyright. A reproduction of material that is protected by copyright may be a copyright infringement. A court may impose penalties and award damages in relation to offences and infringements relating to copyright material. Higher penalties may apply, and higher damages may be awarded, for offences and infringements involving the conversion of material into digital or electronic form.

Unless otherwise indicated, the views expressed in this thesis are those of the author and do not necessarily represent the views of the University of Wollongong.

Recommended Citation

Gargett, Maegan A., High Resolution Radiation Therapy Dosimetry in Magnetic Fields using Novel Silicon Array Dosimeters: A Pilot for MRI-linac Applications, Doctor of Philosophy thesis, School of Physics, University of Wollongong, 2018. https://ro.uow.edu.au/theses1/252

Research Online is the open access institutional repository for the University of Wollongong. For further information contact the UOW Library: research-pubs@uow.edu.au

Centre for Medical Radiation Physics, School of Physics
Faculty of Engineering & Information Sciences

High Resolution Radiation Therapy Dosimetry in Magnetic Fields using Novel Silicon Array Dosimeters: A Pilot for MRI-linac Applications

Maegan A. Gargett
Bachelor of Medical Radiation Physics (Honours)

This thesis is presented as part of the requirements for the
Award of the Degree of
Doctor of Philosophy
of the
University of Wollongong
May 2018

Declaration

I, Maegan A. Gargett, declare that this thesis, submitted in fulfilment of the requirements for the award of Doctor of Philosophy, from the Faculty of Engineering & Information Sciences, University of Wollongong, is wholly my own work unless otherwise referenced or acknowledged. The document has not been submitted for qualifications at any other academic institution.

Maegan A. Gargett, May 15, 2018

Abstract

The integration of online magnetic resonance imaging with linear accelerators presents an exciting new era for radiation therapy. A hybrid MRI-linac machine provides improved soft-tissue contrast enabling the target to be visualised at the time of treatment rather than a surrogate, as is currently common practice. With this advancement comes a number of unique challenges related to the presence of a magnetic field during treatment, one of which is the change in the dose distribution. The magnetic field's associated force vector, the Lorentz force, influences the trajectory of charged particles within it. Dose-depositing secondary electrons are no exception. Using Monte Carlo simulations, point spread dose arrays have been modelled to demonstrate on a fundamental level how dose distributions are perturbed by magnetic fields as a function of magnetic field strength, orientation with respect to the primary beam and the density of the medium. For the case of inline magnetic fields, the point spread distribution maintains its symmetry, but lengthens and becomes more narrow laterally. In the most extreme case, for a low density medium such as lung and a high (3 T) magnetic field strength, there is a maximum in-depth lengthening of (45.0 ± 0.3) mm and narrowing of (6.1 ± 0.3) mm. For a perpendicularly-oriented magnetic field, the dose distribution is shifted laterally and has a decreased depth penetration. There is a complex interrelationship between magnetic field strength and density as to the maximum perturbation seen; the magnetic field strength at which the maximal lateral shift occurs decreases with the density of the material, due to the corresponding increase in electron path length.

The perturbed trajectories of secondary electrons not only causes changes to the dose distribution, but also to the response of the detector systems used to characterise the beam. As such, there is not only a need for a detector that is capable of measuring the subtle, and sometimes not so subtle, changes to dose distributions in a magnetic field, but also one with functionality that is not compromised by the magnetic field. At this point in time, the literature has primarily focused on the characterisation of ionisation chambers in magnetic fields. This is justified by their common utility. This thesis investigates the appropriation of two novel silicon array dosimeters, designed at the Centre for Medical Radiation Physics (CMRP), as magnetic field compatible dosimeters: the MagicPlate-121 and the MagicPlate-512. The MagicPlate-121 is an 11 x 11 epi-diode array with 10 mm pitch. The MagicPlate-512 is a high resolution monolithic silicon array, with 512 active elements placed with 2 mm pitch over a 46 mm x 46 mm detection area. The advantage of utilising high resolution array dosimeters at MRI-linac facilities is that they are appropriate for beam profile constancy monitoring in a solid phantom, and provide high resolution sampling in real time. This is significantly easier to integrate into a regular quality assurance schedule than a point detector and scanning water tank combination.

High resolution Monte Carlo simulations using the Geant4 toolkit have demonstrated the ability of the MagicPlate-121 and MagicPlate-512 to measure megavoltage radiation beam profiles in perpendicular and inline magnetic-field-to-photon-beam orientations. Both detectors were able to measure the penumbral asymmetry characteristic of the perpendicular magnetic field orientation. Beam characteristics such as $80\% - 20\%$ penumbral width and field size were able to be resolved with an accuracy of 0.5 mm compared to that of a homogeneous water-equivalent geometry. The MagicPlate-512 was demonstrated to successfully model radiation beam profiles for small fields down to 0.8 cm x 0.8 cm in dimension, as per its intended purpose as a small field array detector. This was further confirmed through experimental validation on a clinical accelerator, using a purpose-built permanent magnet device that could be configured in both inline and perpendicular magnetic field orientations. The implication of small air-gaps on the response of silicon array dosimeters was also investigated, showing that the electron-return-effect reduces the magnitude of the dosimeter's response in the perpendicular magnetic field orientation (23% at 1 T). However, for air gap layers up to 2 mm in thickness above the dosimeter, the shape of the beam profile is preserved. The detectors are expected to play a valuable role in beam characterisation and ongoing quality-assurance activities at the Australian MRI-linac facility.

Acknowledgements

First and foremost, I would like to thank my supervisors. Professor Peter Metcalfe, your guidance began well before postgraduate study, with small research projects early in my undergraduate degree – these inspiring experiences gave me a passion for academic research and led me towards larger endeavours. Thank you for your counsel over the many years you have acted as my supervisor. To Dr Brad Oborn – your enthusiasm towards this project has been an incredible source of motivation. Thank you for sharing your knowledge and experience with me, particularly with regards to Geant4; I could not imagine having become proficient in the (sometimes frustrating) art of Monte Carlo simulation without your instruction. I would also like to extend my thanks to Distinguished Professor Anatoly Rosenfeld, director of the Centre for Medical Radiation Physics. Your willingness to provide advice is a constant source of encouragement to all your students. Dr Marco Petasecca, thank you for sharing with me your vast knowledge on the detector systems used in this thesis, your time and assistance is very appreciated.

I would also like the thank my fellow students, in particular Sarah Alnaghy. Thank you for being a great soundboard for ideas, and for always being willing to give your time and assistance in preparation for our experiments, particularly during the tedious task of constructing detectors. It has been a pleasure working alongside you. Trent Causer, thank you for your assistance during experimental measurement sessions. To my fellow undergraduate classmates – Saree, Claire, Vanja and Matt, your friendship helped make my experience at the University of Wollongong a rewarding one.

Thank you to my colleagues at Royal North Shore Hospital, particularly Dr Jeremy Booth, for providing the time and support required for me to complete this thesis.

To Mum, Dad, Andrew and David – thank you for your unwavering love and support. You have given me the encouragement I needed to persist through the sometimes difficult times. I am grateful to be able to share the rewarding times with you too.

This research has been supported by an Australian Government Research Training Program Scholarship.

Contribution of Collaborators

Dr Brad Oborn contributed the phase-space files for a Varian 2100c accelerator used for Monte Carlo simulations. Dr Oborn also conceptualised and designed the magnetic apparatus which was used for experimental validation of the detector systems considered in this thesis.

Professor Anatoly Rosenfeld and Dr Marco Petasecca of the Centre for Medical Radiation Physics (CMRP) provided the proprietary dosimeters investigated in this thesis, MagicPlate-121 and MagicPlate-512. Sarah Alnaghy and Trent Causer assisted with the assembly of the electronics of these dosimeters and the associated magnetic field compatible casings. Trent Causer also verified the magnetic field map of the MARDOS device used for experiments.

Dr Martin Carolan allocated time on a clinical accelerator at the Illawarra Cancer Care Center for experimental results to be performed.

Contents

List of Figures

List of Tables

Chapter 1

Introduction

1.1 Overview

According to current estimates, based on data collected by the Collaboration for Cancer Outcomes Research and Evaluation (CCORE), approximately 48.3% of cancer cases would benefit from utilising radiation therapy as part of the course of treatment[1]. Radiation therapy is used in both radical and palliative contexts, to irreparably damage the DNA of cancer cells. The most common form of radiation therapy used in Australia, external beam radiation therapy (EBRT), employs ionising radiation beams produced by a machine called a linear accelerator. The linear accelerator, or linac as it is commonly referred to, rotates around the patient to deliver the therapy as they lie on the treatment bed in a fixed position. By creating specific beam shapes and angles of delivery, treatments are formulated to maximise dose to the tumour volume and minimise normal tissue damage.

Image guided radiation therapy (IGRT) provides a means to more accurately localise the treatment volume before (and even during) treatment delivery. Without image guidance, external landmarks must be relied upon to align internal target structures to the treatment beam - this is not always a safe assumption. Hence, image guidance is particularly advantageous when changes to the treatment volume location, as well as size and shape, are to be expected. This may include, but is not limited to, physical anatomical changes during course of treatment (e.g. tumor shrinkage, patient weight loss) or due to movement of the tumour volume, for example with respiration. Currently, image guidance systems are predominantly kV-photon based. Standard linear accelerators have inbuilt kV and MV photon imaging technology to image the patient before, during and after treatment. A relatively new form of IGRT is one that provides real-time Magnetic Resonance Imaging (MRI) with EBRT in one hybrid system, named an MRI-linac. The combination of MRI machine and linear accelerator provides superior soft tissue contrast over other imaging techniques used for on-line imaging, including the aforementioned kV and MV imaging systems, without the additional imaging dose.

The integration of MRI systems and linacs is non-trivial, not just with respect to engineering but also with respect to dosimetry. The dose deposition mechanism of MV photon beams is through the production and subsequent interaction of secondary electrons with human tissue. As electrons are charged particles, their trajectory is influenced by the presence of a magnetic field. This in turn has the potential to affect the dose distribution in varying ways, depending on the orientation of the magnetic field with respect to the treatment beam, as well as the physical properties of the tissue involved. The impact of the magnetic field on secondary electrons is not only problematic in terms of the radiation dose distribution, but also for the functionality of the radiation detectors that are used in the commissioning and day-to-day quality assurance activities performed on linear accelerators to characterise and maintain their operability. This is particularly true of detectors which perturb the homogeneity of the density of the medium, such as air-filled ionisation chambers.

This thesis will focus primarily on investigating the suitability of silicon array dosimeters for beam profile measurements for any MRI-linac design. The silicon array dosimeters investigated are those designed by the Centre for Medical Radiation Physics (CMRP, Wollongong, Australia). The tissue-equivalence of these dosimeters is superior to that of gas-filled detectors due to their physical state and density, which inherently negates “density effects” where they relate to mass collision stopping power. The relative tissue equivalence of the silicon dosimeters, coupled with their novel slimline and high resolution design, is expected to make them a promising radiation detector system in magnetic field environments. The primary intended site of use for these devices is the Australian MRI-linac facility located at the Ingham Institute, Sydney, Australia; the prototype system is being commissioned at the time of writing. Once fully commissioned the facility will be able to be configured in both inline and perpendicular magnetic-field-to-photon-beam orientations. When the experiments included in this thesis were conducted, the MRI-linac was not ready for measurements to be performed in either orientation. The experimental work for this thesis was performed using a permanent magnet device that easily converted between the two magnetic field orientations, and could be used on a standard clinical linear accelerator. By taking this approach, the silicon array dosimeters considered in this thesis could be characterised in both magnetic field orientations prior to the complete commissioning of the Australian MRI-linac facility.

1.2 Aims and Objectives

The aims of this thesis are:

Aim 1: Compare dose spread array distributions for a combination of magnetic field orientations and strengths, as well as in different media.
Research Question: How does the dose deposition distribution of secondary electrons change in a magnetic field? How does it depend on the medium?
This research question will be addressed by generating dose spread arrays in water, lung and silicon using a pencil beam source with a spectral distribution representative of a linac-generated 6MV photon beam. Results will be given for uniform magnetic fields applied in both the perpendicular and inline orientation, for strengths between 0.5 - 3 T. The results are presented in Chapter 3.

Aim 2: Use a Monte Carlo model of silicon array dosimeters designed by CMRP to model their radiation response.
Research Question: Do the silicon array dosimeters accurately measure beam profiles in inline and perpendicular magnetic field orientations?
This research question will be addressed by comparing Monte Carlo simulations of each dosimeter geometry to a homogeneous water phantom. This will reveal magnetic field induced dose changes, and the accuracy with which the dosimeter can be expected to model them. The two dosimeter systems investigated include the MagicPlate-121, an epitaxial silicon detector array system, and the new generation MagicPlate-512, a higher resolution monolithic silicon detector array designed for small field dosimetry. The MV photon source is generated from phase space files modelled on a clinical linear accelerator. Magnetic fields of strength 1 T and 3 T will be applied, in both inline and perpendicular magnetic-field-to-photon-beam orientations (reflective of current MRI-linac research systems). The results are presented in Chapters 4 & 5.

Aim 3: Experimentally assess the radiation response of a high resolution silicon array dosimeter in a custom designed permanent magnet system.
Research Question: Does the dose response of a novel 2D silicon array dosimeter make it an appropriate choice for beam profile collection in magnetic field environments?
This research question will be answered by performing experimental measurements of the M512 in a permanent magnet system designed to be used in conjunction with a clinical linear accelerator. To enable these measurements, the electronics system of the detector was constructed with a slightly modified design, to be magnetic field compatible. The permanent magnet system allows measurement in both inline (0.95 T) and perpendicular (1.2 T) magnetic-field-to-photon-beam orientations for small photon field sizes. The results are presented in Chapter 6.

1.3 Contributions and Publications

Publications:

M Gargett, B Oborn, P Metcalfe and A Rosenfeld, Monte Carlo simulation of the dose response of a novel 2D silicon diode array for use in hybrid MRI-LINAC systems, *Medical Physics*, vol. 42, no. 2, pp. 856-865, 2015.

M Gargett, B Oborn, S J Alnaghy, T Causer, M Petasecca, A B Rosenfeld and P Metcalfe, A high resolution 2D array detector system for small-field MRI-LINAC applications, *Biomedical Physics & Engineering Express*, vol. 4, no. 3, 2018.

S J Alnaghy, **M Gargett**, G Liney, M Petasecca, J Begg, A Espinoza, M K Newall, M Duncan, L Holloway, M L F Lerch, M Lazea, A B Rosenfeld and P Metcalfe, Initial experiments with gel-water: towards MRI-linac dosimetry and imaging, *Australasian Physical and Engineering Sciences in Medicine*, vol. 39, no. 4, pp. 921-932, 2016.

B M Oborn, **M Gargett**, T J Causer, S J Alnaghy, N Hardcastle, P E Metcalfe and P J Keall, Experimental verification of dose enhancement effects in a lung phantom from inline magnetic fields, *Radiotherapy and Oncology*, vol. 125, no. 3, pp.433-438, 2017.

P Metcalfe, S J Alnaghy, M Newall, **M Gargett**, M Duncan, G Liney, J Begg, B Oborn, M Petasecca, M Lerch and A Rosenfeld, Introducing dynamic dosimaging: potential applications for MRI-linac, *Jounal of Physics: Conference Series*, no. 777 012007, 2017.

Conference presentations:

M Gargett, M Petasecca, B Oborn, S J Alnaghy, A Rosenfeld and P Metcalfe, WE-AB-BRB-04: A novel monolithc silicon 2D detector array for use in stereotactic applications, *American Association of Physicists in Medicine Annual Meeting*, July 2015.

M Gargett, B Oborn, P Metcalfe and A B Rosenfeld, Monte Carlo simulation of the effects of a 1 T transverse magnetic field on a clinical IMRT dose distribution, *MMND-IPCT Conference 2014*, October 2014.

M Gargett, B Oborn, P Metcalfe and A B Rosenfeld, Point spread kernel distortion by in-line and perpendicularly aligned magnetic fields typical of MRI-linacs, *Combined Scientific Meeting of ACPSEM, RANZCR and AIR*, September 2014.

M Gargett, B Oborn, P Metcalfe and A B Rosenfeld, Monte Carlo simulation of the dose response of a novel 2D silicon diode array for use in hybrid MRI-Linac systems, *Engineering anf Physical Sciences in Medicine Conference*, November 2013.

T Causer, B Oborn, **M Gargett**, A B Rosenfeld and P Metcalfe, Experimental verification of the magnetic field of a new apparatus for performing experiments in MRI-Linac dosimetry, *Engineering and Physical Sciences in Medicine Conference*, November 2016.

Chapter 2

Literature Review

This chapter will provide a review of current literature relating to the integration of magnetic resonance imaging (MRI) with radiation therapy. A brief overview of the utilisation of MRI will be given, including a summary of current MRI-linac facilities, followed by an in-depth review of the dosimetric challenges associated with the use of current commercial radiation detection systems in magnetic field environments. Common Monte Carlo toolkits used for radiation therapy applications are also considered, with particular attention paid to GEANT4 − the toolkit used in this thesis to model radiation transport through magnetic fields.

2.1 Image guidance for external beam radiation therapy

Image guidance modalities are a vitally important part of adaptive radiation therapy treatments. Most modern linacs are equipped with on-board kV and MV image guidance for this application. However, they can lack image quality in terms of soft tissue contrast and image artefact, are potentially invasive because of the sometimes-necessary use of fiducial markers to localise the target (due to image quality limitations) and also contribute some radiation dose. MRI presents a desirable alternative, providing superior soft tissue contrast to x-ray based modes, without contributing extra dose. Advantages (and disadvantages) of MRI-guided radiation therapy (MRIgRT) will be addressed in this section. This section will be brief, with the inclusion of references to direct the reader to more detailed reflections on the topic.

2.1.1 MRI and radiation therapy

MRI has a history with radiation therapy that precedes its use for image guidance. MRI scans are commonly used as a secondary image set to the planning (simulation) CT, to aid the oncologist and/or treatment planner in the accurate segmentation of target volumes and critical structures. For example, it is considered the superior imaging modality for delineating cervical cancer[2], and is also routinely used in prostate and brain segmentation. MRI-only planning strategies have been formulated and are an active area of research[3], for example, the formulation of atlas-based approaches to allocate electron densities to MR images[4,5]. To date, CT remains the most common primary imaging acquired during the simulation process because of the electron-density information inherently provided for the calculation of dose. It is also highly accessible, with modern radiation therapy centres maintaining their own CT scanners. The advantage of the integration MRI in radiation therapy lies in its ability to provide superior soft tissue contrast to CT, that is further enabled by the variety of possible imaging sequences, without adding imaging dose. Common imaging sequences and their application in different anatomical sites is summarised by Metcalfe et al[6].

The benefits of further integration of MRI into the treatment workflow seems obvious; to harness the superior image quality in real time, monitoring the target and organs at risk (OARs) themselves, rather than a surrogate structure/marker as is commonly done for kV-based imaging. Further to this, functional information inferred from the MRI may eventually be used to adapt the treatment.

While there is significant benefit to integrating MRI into the radiation therapy setting, the technique is not without its limitations. This includes a slower acquisition time and associated imaging artefacts due to movement, as well as financial cost. It is also important to choose imaging sequences with a high level of geometric accuracy - this is not necessarily of paramount importance for diagnostic imaging applications, but is certainly so for radiation therapy planning[7–9]. These limitations are being addressed and adaptive workflows are being devised to allow the full advantages of MR integration in the radiation therapy setting to be utilised[10–13].

Reviews by Metcalfe et al[6] and Lagendijk et al[14] delve deeper into the pros and cons of the role of MRI in radiation therapy, to which readers are referred for more details.

2.2 MRI-linac hybrids

There are a handful of prototype MRI-guided radiation therapy (MRIgRT) systems worldwide[15–18] investigating the feasibility of the hybrid IGRT technique. The first patient treatment was performed in early 2014[19] on a Co-60 machine, with low-field integrated MR imaging. In 2017, the first patient treatment was performed on the Elekta Unity MRI-linac machine[20], which is a 1.5T MR scanner integrated with a modified linac. Each institution is adopting its own unique configuration of imaging orientation (inline and/or perpendicular), bore design and field strength. This is summarised in Table 2.1, for both prototype and clinical systems worldwide.

As summarised in the previous sections, there are compelling hypotheses about the ad-

Table 2.1: Facilities with combined EBRT - MRI capabilities.

Institute	Machine type	B strength	Bore design	Orientation
Ingham Institute, Sydney, Australia[21]	6MV Linatron	1 T	Split	In-line & perpendicular[a]
UMC Utrecht, The Netherlands[18]	Elekta Unity 7 MV Linac	1.5 T	Closed	Perpendicular
Cross Cancer Institute, Alberta, Canada[17]	6MV Linac	0.6 T	Split	Inline & perpendicular
ViewRay, OH, United States[16]	ViewRay MRIdian Co-60	0.35 T	Closed	Perpendicular
ViewRay OH, United States[22]	ViewRay MRIdian 6MV Linac	0.35 T	Closed	Perpendicular
Princess Margaret Cancer Centre, Ontario, Canada[15]	Varian 6MV Linac	1.5 T	Closed, rail mounted	Perpendicular

---

[a] Designed to enable perpendicular orientation, but this orientation has not yet been commissioned.

vantages of an MR approach to IGRT; but the combination also presents a number of unique engineering and dosimetric challenges.

2.2.1 Engineering challenges

The challenges related to the engineering of a MRI-linac hybrid primarily stem from magnetic interference on the linac, radiofrequency interference on the MRI and beam transmission through the MRI bore. All of these challenges require some form of modification to either the accelerator or the MRI scanner to compensate for the others' presence.

Magnetic interference in components of the linac due to the fringe field of the scanner can result in output losses, for example if the waveguide current is disrupted by electrons being deflect by the magnetic field[23]. Magnetic interference can be resolved by using appropriate shielding[24], or through redesign of the electron gun to negate the need for shielding all together[25].

Radiofrequency interference can be introduced to the MRI scanner due to the close proximity of linac components. To quote some examples, the MLC components can contribute to MRI field distortion[26], and radiation induced currents can be generated in the magnetic coils of the scanner[27]. Increasing the source-to-isocentre distance, introducing buildup material around RF coils, shimming techniques, as well as a cleverly designed Faraday cage can manage radiofrequency interference. For example, the UMC Utrecht system has an aluminium cryostat wall that forms part of the Faraday cage, so the accelerator components do not interfere with the scanner radiofrequency[28].

Beam transmission through the MRI bore is a consideration only for scanners in the perpendicular orientation. Beam penetration through the cryostat can harden the primary beam. Additionally, beam attenuation through the cryostat can vary owing to its dependence on the level liquid helium filling, which can be inconsistent. These issues can be minimised by essentially splitting the magnet, by removing a small section of coils, in order to create a beam "portal"[29].

2.2.2 Dosimetric effects

Of particular importance to magnetic field dosimetry are the implications relating to the behaviour of dose depositing secondary electrons. Considering that the interaction of primary photons in the MV energy range is dominated by Compton scattering, the trajectories of secondary electrons produced within the medium are susceptible to perturbation by the magnetic force. Hence, so is the expected dose distribution.

$$\vec{F_B} = q\vec{v} \times \vec{B} \tag{2.1}$$

$$r = \frac{mv}{qB} \tag{2.2}$$

Magnetic fields exert a magnetic force, commonly referred to as the Lorentz force (see equation 2.1), on moving charged particles that acts perpendicularly to their velocity, affecting the direction of the particle's trajectory. When a particle (charge q, mass m) with velocity ($\vec{v}$) enters a perpendicularly oriented uniform magnetic field ($\vec{B}$) the Lorentz force directs it into a circular trajectory of gyration radius r (see equation 2.2). In the case that the velocity has a component parallel to the magnetic field, the charged particles traverse a helical trajectory. When the velocity and magnetic field directions fully align, the Lorentz force becomes zero. The three cases considered so far apply to the movement of a charged particle in a vacuum. When we consider the behaviour of an electron within a tissue, the extent to which the circular/helical trajectories can be fulfilled depends on the density of the medium in question, because the electrons involved scatter from interaction to interaction. When in a uniform magnetic field, the trajectories of electrons travelling between collisions become arced in the direction of the Lorentz force. The effect of the magnetic field on the trajectory will only be significant for gyration radii smaller than the electron range within the medium[30].

Perpendicular orientation

When considering magnetic field induced effects on a fundamental level, individual dose kernels subject to a perpendicular magnetic field see a lateral shift in dose, less depth penetration and a smaller surface area of the dose kernel as field strength increases[31]. The changed shape of kernels mean there is a reduced build-up distance, and field profiles are asymmetric in the penumbral regions according to the direction of the magnetic force in relation to the primary beam. The interaction also leads to a characteristic phenomena described by Raaijmakers et al as the Electron Return Effect (ERE)[32]. ERE occurs at high-low density interfaces. When electrons leave a high density medium such as water for a low density medium, such as air or lung, the electrons can more easily fulfil the helical trajectory induced by the magnetic force, because they have a longer path length between collisions. This means that (in a perpendicularly oriented magnetic field) the Lorentz force directs electrons back towards the boundary, resulting in some re-entrant dose. These characteristic features of magnetic field dosimetry will be further explored in this section, including how they impact the final dose distribution.

In 2004, Raaymakers et al[33] pioneered a study of the effects of a 1.5 T perpendicularly oriented magnetic field on dose deposition for 6 MV photons, in preparation for the construction of the Utrecht collaboration's MRI-linac. Using GEANT4 simulations, the authors looked at the effect of the magnetic field on pencil beam dose deposition kernels, as well as 1 x 1 cm^2 and 5 x 5 cm^2 beams (convolved from the kernels). Some experimental data to support simulations was produced by measuring beam profiles (1 x 1 cm^2 field size) using film, with a 1.1 T magnetic field produced by a permanent magnet. For a pencil beam, they noted a shift in depth dose profile of 3 mm (towards surface) at 1.5 T. The penumbral size also increased at one side of the beam and decreased at the other. For the 5 x 5 cm^2 beam, the FWHM was unaffected, but the field position shifted 0.7 mm (for all depths beyond D$_{max}$). For the same field size, the penumbral width (80% - 20%) on both sides were equal, but larger than the 0 T case (approx 2 mm at 0 T vs 3.5 mm at 1.5 T). For a 1 x 1 cm^2 field size, opposing penumbra were unequal in width, due to a lack of lateral electron equilibrium. The decrease in D$_{max}$ for these field sizes was approximately 5 mm. In summary, as field size increases the penumbral asymmetry decreases, but the asymmetry in dose deposition remains.

The Utrecht group next evaluated the effects of ERE at various water-air interfaces due to a 1.5 T transverse magnetic field[32]. Raaijmakers et al used GEANT4, as well as experiments with an electromagnet (0.8 T) to confirm the existence of ERE. The beam source was produced by convolution for a 4 x 4 cm^2 field size. Two different simulation geometries were investigated: a water phantom with a horizontal layer (2 cm width) of air, and a water phantom with a cylindrical tube of air (2 cm diameter). For the first geometry there was an obvious increase in dose in water abutting the entrant side of the air interface due to ERE (see Figure 2.1). The increase in dose also appeared to be shifted from the central axis of the primary beam, in the direction of movement of electrons under the influence of the magnetic force. The shift was approximately 4 mm, which corresponds to theoretical calculations of the radius of curvature of electrons at 1.5 T (about 2.2 mm for 0.5 MeV electrons, assuming the average electron energy is one quarter of the average photon energy, this being approx. 2 MeV for a typical 6 MV photon spectrum). There is then a decrease in the dose deposition at the water interface directly after the air, due to a lack of electrons traversing the full length of the air cavity - the magnetic force is deflecting electrons in the air cavity from what would normally be a forward-directed (on average) trajectory, to a lateral and back directed trajectory. Therefore in the magnetic field case there is less dose at this interface because initial build-up has to re-occur, whereas this is not the case when B = 0 (there is still some build up due to lateral spread of electrons in the air cavity), see Figure 2.1. The authors investigated whether the resultant hot and cold spots at the cavity interfaces could be counteracted using opposing fields. While a more uniform distribution can be achieved, the dose increases/decreases do not completely cancel each other out. This is not surprising, since the physics behind the respective dose increase and decrease are different. A similar effect was seen for the second geometry, the 2 cm diameter cylinder of air, although the region of dose increase (and decrease) is slightly cyclic, with its location corresponding to the region with the highest flux of electrons entering the cavity in an already lateral direction, hence aiding their deflection from a forward-projected trajectory. In the case of the cylindrical cavity, a singular pair of opposing beams did not cancel out the hot and cold spots, but the addition of another opposed pair (i.e. four beams spaced by 90°) negated the effect.

As is alluded to by the above-mentioned paper by Raaijmakers et al, there can be an increase in exit dose in a perpendicular magnetic field. For the most extreme case, a singular field, the exit dose was shown to be 40% higher in a 1.5 T magnetic field than the zero field case. The effect is minimised through the use of multiple beams. This effect is of course dependent on the strength of the magnetic field, with Kirkby et al[34] reporting exit dose increases of 5% in 0.2 T perpendicularly aligned magnetic fields. Oborn et al[35] have used high resolution simulations where dose is scored in 10 μm voxels to more accurately estimate increases to skin dose (defined to be at a depth of 70 μm by the International Commission on Radiation Units and Measurements (ICRU)[36]) for a 6MV divergent beam. The authors report that the effect is worst for intermediate field strengths (101.7 - 106.3% higher than the 0 T case at 0.75 T, for field sizes 5 x 5 - 10 x 10 cm^2) compared to high field strengths (37.9 - 40.6% higher than the 0 T case for 3 T, for field sizes 5 x 5 - 10 x 10 cm^2), due to a higher proportion of exit electron fluence than for the higher field strengths.

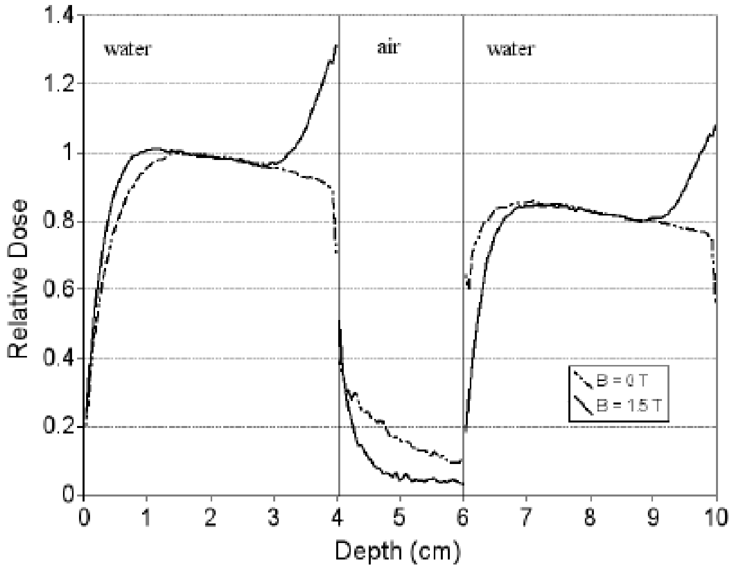

Figure 2.1: A graphical depiction of ERE occuring at water-air interfaces. Figure taken from Raaijmakers et al 2005[32].

Raaijmakers et al[37] show that in a magnetic field the surface orientation in relation to beam entry angle can affect the surface dose, build-up distance and exit dose more compared to the zero field case. Taking the example of a magnetic force that directs charged particles in a clockwise trajectory: for a negative surface angle, the electrons are curving into the phantom, away from the surface (where 0 deg is perpendicular to direction of photons); for positive surface angles, electrons in the phantom are curving back towards the surface. Thus as angles go from negative to positive the build-up distance decreases. The minimum surface dose was found to be at -30°. A similar trend occurs in terms of changing exit dose, where exit dose increases as the surface angle goes from positive to negative, with the exception that when the surface edge gets to -60° (i.e.approaching parallel to photon beam) the exit dose starts to decrease again. In the most extreme cases, the build-up distance was observed to vary from 0 mm to 35 mm, the surface dose varied from 25% to 142% of the dose at d_{max}, and exit doses varied from a 56% increase to a 16% decrease.

Raaijmakers et al further investigated the exit dose, lateral ERE, ERE around cavities and at lung interfaces in a later publication[31] for a range of magnetic field strengths (from 0.2 T to 3 T). They reported that the size of the radiation beam also determines the level of exit dose increase. If the field size is small, returning electrons will deposit dose outside the primary beam. If the field size is large enough such that the radius of returning electrons is small in relation to it, the in field exit dose will increase. That is, ERE dose increases with field size for field widths (in the direction of the magnetic force) smaller than the sum of the maximum electron trajectory diameter and the penumbral width. Dose hotspots due to ERE at the exit side of the beam were reported highest at 0.75 T, then decreased for higher strengths. This is due to the changes occurring to the shape of dose kernels with increasing field strength. As the field strength increases there is a decrease in penetration depths of the kernels - thus electrons at the exit side originate from a smaller volume, which means that the electron fluence decreases in this area and ERE is reduced. Also, the spectrum of electrons are harder in this region, since low energy electrons with smaller trajectory radii cannot penetrate as far into the tissue so they contribute less to the spectrum at the distal side of the phantom.

The change in the shape of the kernel not only means decreased penetration depth, but a more laterally directed spread of electrons, which leads to lateral ERE dose increases at the edge of a phantom (given the field size covers the entirety of the phantom) and a consequent dose decrease at the opposite side. Where air cavities are concerned, the size of the cavity and the magnetic field strength will determine whether ERE will occur. Results showed that ERE around air cavities is more severe the larger the cavity and the stronger the field strength. Once the cavity approached a size such that the radius of the electron trajectory is large in comparison to it, ERE will not occur; the electron fluence will not be perturbed by its presence. It was also observed that as the magnetic field strength changes, so did the location of the hot/cold spot - this can be accounted for when considering the radius of curvature of the electron tightens as magnetic field strength increases, and hence there is a change in average trajectory. A slab phantom with a lung-density inhomogeneity showed changes to the dose distribution similar to that of an air gap[32], as discussed earlier. The dose increase at the water-lung boundary due to ERE was as high as 49%, and the dose decrease at the lung-water interface was as high as

36%. Both extremes occurred at 1.5 T field strength. The effects are insignificant for a 0.2 T field strength.

Expanding on the fundamental dose changes induced by the presence of the magnetic force, there have been some studies into the effects of magnetic fields on total dose distributions representative of typical radiation therapy treatment plans. Kirkby et al[34] looked at glioblastoma (brain) as well as lung treatment plans. The brain plan was a 4-field opposed arrangement (anterior-posterior and lateral), and the lung plan was a 5-field arrangement. Both were planned using a 6MV 3DCRT technique with all fields equally weighted. The plans were modelled in a magnetic field environment using an in-house EGSnrc Monte Carlo treatment planning dose verification system. They show that there are changes to the dose distribution caused by magnetic field, even at field strengths as low as 0.2 T (albeit small). For the brain case, where the medium is relatively homogeneous, only small changes to the dose distribution were observed with the introduction of 0.2 T and 1.5 T magnetic fields. The change was primarily to surface dose, with a maximal increase of 4% for the 0.2 T field strength, and 10% for the 1.5 T field strength due to re-entrant dose originating from ERE. In the case of the 1.5 T field strength, there were also hot and cold strips visible along opposing field borders in the direction of the magnetic force (approx. 5%); a result of the asymmetric field penumbra characteristic of field profiles produced in a perpendicular magnetic-field-to-photon-beam orientation. For the lung case, where the medium is significantly more inhomogeneous, there were up to 30% increases in dose and 15% decreases in dose at at lung-tissue interfaces for the 1.5 T field strength. For the lower 0.2 T field strength, the variation was within ±12%. These effects need to be compensated for in some manner during the plan optimisation process; the authors suggest that a Monte Carlo solution may be required.

The results presented by Kirkby et al[34] are in specific reference to static, unmodulated plans. Raaijmakers et al[38] further investigate the dosimetry-related impacts of perpendicularly oriented magnetic fields for IMRT plans. The authors considered the extent to which ERE effects limit the homogeneity of dose distributions, and whether the IMRT optimization algorithm can compensate for expected inhomogeneities. To do this they custom designed an inverse treatment planning system that was based on 1.5 T beamlet dose distribution kernels, which were calculated via Monte Carlo methods. Three cases were considered, including prostate, laryngeal and oropharyngeal cases. The prostate was classed as the most basic, being the most homogeneous case (in terms of tissue density variation). The laryngeal case was included because of the proximity of air pockets to the PTV and the oropharyngeal site was included as a more complex case, with multiple target structures, to push the limits of IMRT optimisation capabilities. To evaluate the distributions, comparisons were drawn between the dose volume histograms (DVH) for a 1.5 T magnetic field strength and zero field scenario.

First considering the prostate case, the tissue homogeneity meant that there was little difference in the dose distribution for 0 T and 1.5 T. However, the skin dose did increase for some beams, due to build-up distance dependence on surface orientation. Suggested solutions to minimise the effect are to use a bolus build-up material, model skin as OAR in optimization process and/or use more beams to spread out surface dose. The skin dose increases were most severe at the entrant side of the beam. Re-entrant dose at exit side was small by comparison, in part due to attenuation through the patient.

For the second, laryngeal case, to plans were created - one with 6 paired opposed beams, and a 5 field non-opposed arrangement. This was to test the theory that opposing beams will be necessary to counterbalance the hot and cold spots resultant of ERE. Better correspondence of DVHs was seen for the plan with non-opposing beams, which indicates that opposing beams are not necessary for IMRT planning in magnetic fields. The last case considered, the oropharyngeal case, also showed good agreement in terms of DVH comparison to the zero field plan. This further solidifies the theory that IMRT optimization is capable of correcting for magnetic field-induced dose effects without the specific need for opposing beams.

Inline orientation

The literature on dosimetry for inline MRI-linac systems is significantly less than for those of the perpendicular orientation. Considering magnetic forces for a field inline with the direction of the primary beam, the changes in dose distribution are perceived to be less dramatic. It has been shown in early publications presenting both Monte Carlo simulation[30,39] and experimental[40] data, that the symmetry of dose kernels will be preserved and lateral scatter minimised, with energy deposition focused parallel with the primary direction of the beam. More recent publications, which will be discussed below, show that the inline configuration may aid higher target dose and lower peripheral dose for specific geometries. While an increase in exit dose due to ERE is not a concern in this orientation, there is potential for a higher entrant surface dose due to focusing of electron contamination (electrons generated in components of the linac head and air) before reaching the surface.

The effects of an inline magnetic field orientation on MV photon dose distributions has been shown to be less substantial, and even advantageous when it comes to low density tissues[41,42]. In a simulation study published by Kirkby et al in 2010[41], it was shown that there was little change to the dose distribution in water in the presence of inline magnetic fields, and in low density material such as lung, lateral dose confinement due to the magnetic field resulted in dose distributions that were more focused and delivered a higher dose to the target. Additionally, as expected from the change in direction of the magnetic force relative to the primary beam, dose hot spots at high-low density interfaces characteristic of the perpendicular orientation were absent. This was demonstrated first for a pencil beam incident on water and lung slab geometry, then for a divergent 5-field lung plan (conformal) using patient geometry. The pencil beam simulations show that for homogeneous water geometry, a 1.5 T field strength results in negligible change to the dose distribution (1% increase in central axis dose, little visible narrowing). A 3 T field strength results in substantial narrowing of the distribution in the forward direction and a 3.8% increase in central axis dose. For the lung geometry, the beam-focusing effect is obvious. For 1.5 T and 3 T field strengths, the dose increase at the central axis is 2.7% and 14.9% respectively. The distribution is far less broad in the penumbra, with the magnetic field restricting the lateral scatter that is encouraged by the low density medium in the 0 T scenario. For the 5-field lung plan calculated on patient geometry, differences in dose distribution relative to the 0 T case are less than 5% for field strengths up to 0.5 T. For a 1.5 T field strength, hot spots of 15% are seen along the beam axis in low density regions, and cold regions can be seen at field edges. At 3 T, a similar pattern is observed, however over a smaller volume. This is attributed to the smaller gyration radius at 3 T relative to 1.5 T. No ERE was observed at tissue-lung interfaces, an effect which becomes apparent at field strengths as low as 0.5 T for the perpendicular orientation; this is as is to be expected, from an understanding of the fundamental physics underlying ERE.

The impact of inline magnetic fields on lung dosimetry was further investigated by Oborn et al in 2016[42], who considered 8 clinical lung cancer cases for field strengths 0.5 T, 1 T and 3 T in a simulation study. Both 3DCRT and IMRT plans were considered, and were not reoptimised for the magnetic field case. The authors reported dose enhancement effects in the target, the magnitude of which depended on their size and density. The origin of this effect is most simply explained by considering that for a singular beam, dose enhancement occurs along the central axis; this effect is enhanced at the superposition point of these beams i.e. at the target. The dose enhancement is up to 23% higher at 1 T than 0 T for small tumour volumes (here considered <15 cm^3), and reduces to 5-10% for larger tumour volumes. This can be explained considering that small tumour volumes are typically treated with equally small field sizes, which lack lateral electronic charged particle equilibrium. Hence, it can be expected that the effect of the magnetic force on lateral spread will be relatively greater than for larger fields. The dose enhancement was seen to be higher for tumours where the average density of the planning target volume was lower, since the lower density medium facilitates more focused dose deposition. It should be noted that these best case scenarios consider geometry where the tumour volume is surrounded by lung tissue; the authors reported that the dose enhancement effect will be minimised for tumour volumes in contact with the higher density chest wall, for obvious reasons. When comparing dose enhancement effects for the different field strengths, it was found that the dose increase to the target (reported in terms of dose covering 98% of the planning target volume) was larger for the 3 T field strengths, and lower for the 0.5 T field strength, relative to 1 T. As was reported by Kirkby et al[41], at 3 T the dose increases are more localised and smaller in volume. Across the 8 plans considered, no significant change to the dose received by non-target structures was observed.

Of dosimetric concern in the inline orientation are potential increases in skin dose due to focusing of electron contamination. Due to the orientation of the magnetic field, electrons generated by interactions of the primary beam with the head of the linac (and air) are forced toward the patient surface, therefore contributing to a higher surface dose than for a zero-field setting. Oborn et al[43] present results of simulations modelling the effect of the MR and fringe field on contamination electrons and their contribution to skin dose, finding that for a 6MV beam and magnetic field strength ranging as small as 0.25 T, the skin dose (modelled as the first 70 μm of the surface of a water phantom) increases to up to 80% of D_{max}. The skin dose increased with field size, as the surface area for collimator scatter increases. This result refers to a magnetically shielded collimation system; without magnetic shielding, the increase in skin dose was as much as 1000% of D_{max}. The skin dose was affected by design aspects of the system, such as coil systems, fringe field strength and isocentre distance, indicating that careful MRI-linac design will play a crucial role in the minimisation of this effect. This is further indicated by Keyvanloo et al[44], who presented results on skin dose increases by specifically modelling the Alberta rotating biplanar MRI-linac system (0.56 T), configured in the inline orientation. Results showed that for this system design, skin dose was 8% higher than the zero field case for a 10 x 10 cm^2 field size. This shows that although the increased skin dose effect is unlikely to be mitigated altogether, it can be reduced to a clinically acceptable range. Design-specific simulations of the Australian MRI-linac system (1 T), later presented by Oborn et al[45], included an assessment of the efficiency of a proposed “electron contamination deflector”, as well as a helium gas “contamination purger”, to reduce the production of electron contamination in the system and hence decrease skin dose. Results showed that implementing these systems was effective in reducing skin dose, which ranged from 12% to 65% of D_{max} depending on field size.

2.3 Detector magnetic field compatibility

This section will summarise the available literature relating to detectors which have been investigated in magnetic fields. These include both Monte Carlo and experimental studies.

Magnetic field compatible dosimeters will be necessary for MRI-linac commissioning, routine quality assurance (QA) and patient specific QA. Not only do the components of detectors themselves need to be non-ferromagnetic, the detector response needs to be reliable in a magnetic field. As is discussed in the following sections, literature is available investigating possible changes in detector response in a magnetic field. It has been found that corrections are necessary for a number of point detectors in magnetic fields. These corrections have been shown to be dependent on the magnetic field strength and orientation with respect to the incident photon beam, the detector orientation with respect to the photon beam and the detector geometry.

2.3.1 Point detectors

Ionisation chambers

Mode of operation: Ionisation chambers are considered the “gold standard” of dosimetry, being arguably the most versatile of the dosimeters. They can be used for reference and relative dosimetry of photon, electron and proton fields in radiotherapy; and can be operated in air, water or solid phantoms. Ionisation chambers are commonly used for commissioning and routine dosimetry quality assurance of linacs. Ionisation chambers are commonly air-filled, with two electrodes in either a cylindrical/spherical or parallel plate arrangement. A potential difference is applied between the electrodes. The effective point of measurement (EPOM) of chambers is not centred within the chamber; for cylindrical chambers it is shifted by three-fifths of the inner radius towards the source for MV photon beams, and is on the inner surface of the entrance window for parallel plate chambers[46,47]. Charge is collected in the chamber and converted to dose using the relationship between charge, stopping power ratio (water-air) and the energy required to produce an ion pair in air.

While ionisation chambers are capable of very accurate and reproducible measurements, they are not a perfect dosimetric solution. They can be subject to volume averaging effects, which is of particular concern for small fields and the steep dose gradients often found in modulated fields. In addition to this, a chamber is only able to provide a single point dose measurement at a time. Adequate sampling often requires repositioning the ionisation chamber several times, which can be a time consuming process. Measurements with ionisation chambers can also be subject to post-irradiation leakage and voltage drifting. Drifting can be monitored by comparing a standard reading taken at the beginning and end of the measurement session.

Magnetic field compatibility: Ionisation chambers were the first recorded dosimeters to be investigated for MRI-linac applications, and remain the most widely so. The altered secondary electron dose deposition at tissue-air interfaces, as reported by Raaijmakers et al[32], poses the question as to whether ionisation chamber dose measurements will be affected in the MRI-linac environment. It was shown by this group previously that dose depositing secondary electron trajectories are changed at tissue-air interfaces (ERE), which could change the fluence distribution to the ionisation chamber cavity and in effect change the detectors dose response in a magnetic field.

The University Medical Centre (UMC) Utrecht evaluated the feasibility of using a Farmer

NE2571 chamber in the presence of a 1.5 T magnetic field[48]. This was done through a simulation study, as well as experimental measurements to verify simulation results where possible, using a 1.25 T electromagnet and a 6MV linac beam. The magnetic field was oriented perpendicular to the photon beam, and two different chamber orientations were considered - one perpendicular and one parallel to the incident photon beam. The experimental setup assumes the dose is unchanged by the presence of the magnetic field at the chamber location. Dose response changes were measured at different field strengths, as a ratio of the zero field case.

In the perpendicular chamber-to-photon-beam configuration the chamber response first increases (max. 8.3%), then decreases (in a field strength range 0 - 2 T). For the parallel configuration, the response first decreases (max. 11.3%), then increases. The point of inflection for both cases is about 1 T. This indicates that a magnetic field strength dependent correction is necessary for ionisation chamber dosimetry in a magnetic field.

The origin of the change in dose response of the chamber is a change in the dose deposition to the cavity itself, since the number of electrons entering the chamber and their path length is changed by the magnetic field. For the perpendicular configuration, the number of electrons reaching the chamber decreases continuously as the field strength is increased, and the average path length increases up until 1 T. For the parallel configuration, the number of electrons remains constant and the average path length decreases until 1 T.

Changes to the number of electrons reaching the chamber can be explained by considering the change in dose distribution of point spread kernels. As the field strength increases (in the perpendicular orientation) the depth penetration becomes shorter and there is more lateral stretch, so the number of electrons reaching the anterior surface is less. The change in path length is due to helical trajectories, the length of which spent in the air cavity depends on the cavity shape (and therefore its orientation in field).

A study into the basic operational characteristics of the chamber was later published by Smit et al[49]. These tests included linearity (with MU delivered), repeatability and the influence of chamber orientation. They also investigated the impact of the presence of the magnetic field on ionisation chamber correction factors used to calculate dose from the raw ionisation chamber reading - P_{ion} and P_{pol}. Measurements were performed in the prototype MRI-linac system, with a field strength of 1.5 T at isocentre.

The chamber response was determined to be both linear (to within 0.2% in the range 200 - 1000 MU) and reproducible in the 1.5 T field. The chamber orientation was sensitive to rotation about the photon beam CAX, as expected from previous findings[48]. The chamber was least sensitive to small changes in position when its axis was perpendicular to the magnetic field, and thus this setup was deemed the best for dosimetry measurements.

P_{ion} is a correction factor applied to the raw charge reading to account for incomplete ion collection. P_{pol} is also a multiplicative correction factor, which accounts for polarity effects. Since the magnetic field affects the path of electrons in the chamber, the ion collection efficiency could be influenced. Changes to the polarity of the chamber also have the potential to change the associated correction factor. Polarity effects were tested by taking 10 measurements and switching the polarity of the chamber (and letting it equilibrate) in between each measurement. The calculated ion recombination factor and polarity corrections saw negligible change within the magnetic field relative to 0 T.

The total influence of the 1.5 T perpendicular magnetic field was assessed by calculating the ratio of ionisation chamber reading with and without the field, which can be used as a correction factor ($M_0/M_{1.5}$). There was an average increase in chamber reading of (4.9% ± 2.5%), which corresponds to a correction factor of 0.953. It was deemed feasible to use this chamber (with corrections) in a magnetic field.

The position of the EPOM of cylindrical chambers has been reported to deviate from the 0 T case in a 1.5 T perpendicular magnetic field[50]. The position shifts down stream, and laterally according to the Lorentz force vector. For a 0.6cc farmer chamber, the offset of the EPOM from the central axis of the chamber was halved when the chamber was operated within the magnetic field; the EPOM position went from 0.6x the radius of the chamber at 0 T to 0.3x the radius of curvature at 1.5 T in the vertical direction. Laterally, the EPOM shifted off the central axis of the chamber by 0.38x the radius.

Ionisation chamber dose response in an inline magnetic-field-to-photon-beam orientation has also been investigated by the Cross Cancer Institute in Canada, where they have a bi-directional setup[51]. A Farmer NE2571 chamber and PR06C chamber (both of similar geometry) were investigated through a simulation study, up to a field strength of 1.5 T. Results showed little change in response (2% higher above 1 T, when chamber parallel to photon beam) for both chambers. This is not unexpected considering the geometry of dose kernels in this field orientation remain symmetric, unlike the perpendicular case.

An MRI-compatible scanning water phantom has been used to perform measurements at the UMC Utrecht's facility[52]. It is a PTW-MP3T scanning water phantom which has been adapted to be magnetic field compatible. The tank itself sits inside the bore of the magnet, and the control unit is outside (but still in the fringe field). Some components needed to be replaced to be compatible with the magnetic field, for example the electronic motors were replaced with ultrasonic motors. The geometric accuracy and precision of the tank was assessed with no issue, with or without a magnetic field present, and was benchmarked against another unmodified tank. Effects on the measurement capabilities of a moving ionisation chamber were also tested, with no issue.

The impact of the size of the sensitive volume of ionisation chambers on response in a magnetic field has also been investigated[53]. In a simulation study (EGSnrc), the dose to the sensitive volume per unit incident fluence was compared for chambers with sensitive volume ranging from 0.0146 cm^3 to 0.607 cm^3, for a magnetic field strength range of 0 T - 2 T in the perpendicular orientation. Both a Co-60 and 7MV photon source were considered. A dependence of chamber response on the sensitive volume size of a chamber showed significant variation. It was found that chambers of a larger radii demonstrated a peak in response at lower magnetic field strength than for chambers of a smaller radius, as secondary electrons have a larger radius of path length curvature at weaker magnetic field strengths. The chamber response peaks, then decreases with increasing magnetic field strength due to decreasing gyration radius of secondary electrons and therefore complete rotations occurring within the chamber volume. For all chambers, decreasing the sensitive volume from the stem end resulted in an increase in chamber response; indicating that in magnetic fields the tip of the chamber has a higher average dose. The authors suggest this may be due to the direction of rotation of the secondary electrons, in this instance in the direction away from the sensitive volume and towards the stem. Thus chamber and magnetic field orientation may affect the change in response; this however has not been investigated. The findings of this study indicate that the accurate definition of the sensitive volume of an ionisation chamber will be crucial in the modelling of detectors for the calculation of MC derived correction factors, for example when calculating chamber perturbation factors for reference dosimetry.

A Monte Carlo-generated correction factor, which converts the beam quality correction factor at 0 T conditions to one that applies in 1.5T conditions, has been investigated for the Elekta MR linac[54]. The authors modelled in GEANT4 farmer-type ionisation chambers commonly used for reference dosimetry, under reference conditions (following TG51/TRS398 protocol), and scored absolute dose with and without a 1.5 T perpendicularly-oriented magnetic field. A chamber specific magnetic field correction, k_B, was calculated based on the ratio of the difference in absorbed dose with and without the magnetic field (respectively relative to water). The correction was calculated for several ionisation chamber orientations, including variations on the chamber axis being parallel and perpendicular to the magnetic field. The magnitude of the Monte Carlo correction was confirmed by comparing it to a directly measured one on Elekta MR linac, in 0 T (i.e. quenched magnet) and 1.5 T conditions. There was a clear dependence of the correction factor on chamber orientation. The smallest correction was when the chamber was parallel with the field direction, being less than 1%. On average, in the orientation where the magnetic field directed electrons away from the sensitive volume and towards the stem, the correction was largest at 3.9%.

Difficulty has been reported in the use of solid phantoms for magnetic field dosimetry with ionisation chambers[54–57]. This is due to the presence of submillimeter air gaps that exist around the chamber due to milling of the solid phantom. In a simulation study by O'Brien et al[56], the authors showed that a 0.2 mm air gap resulted in a 1.6% change in measured dose. This is for a so-called asymmetric gap, where the chamber abuts one side of the chamber insert but not the other. If the air gap is symmetrically distributed around the chamber, the effect reduces to less than 0.5% for air gaps up to 1.4 mm. The authors suggest this effect is not a consequence of ERE, but due to a loss in contribution of electrons generated in the air gap, which would otherwise be compensated for in 0 T conditions due to the longer range of secondary electrons.

Diode detectors

Mode of operation: When a semiconductor is exposed to ionising radiation, negative electrons are excited from the valence to the conduction band of the crystal leaving positive holes in the valence band. The valence and conduction bands are separated by a so-called band gap, to introduce a minimum energy at which recombination occurs (1.1 eV for silicon). Silicon diodes are a widely used semiconductor detector. They can be either n- or p- type, depending on whether they have been doped to create an abundance or deficit of free electrons, respectively. The fundamental operation of diodes is based on the diffusion of charge carriers in an electric field created by a p-n junction. A p-n junction refers to the abutment of p-doped (excess of holes) and n-doped (excess of electrons) substrates, one of which is more heavily populated with majority carriers, such that natural diffusion of the charge carriers occurs across the boundary until an equilibrium is reached. The charge gradient creates an electric field, in a region defined as the depletion region. When exposed to radiation, the mobilised minority carriers in each substrate diffuse towards the junction and, if they reach the depletion region, are swept across the junction by the intrinsic potential and measured as charge. The charge created is linearly proportional to dose. A reverse bias may be applied across the junction to increase sensitivity and improve response time. However, this also increases the leakage current contribution, which is temperature dependent. For this reason diodes are commonly used in practice without external bias.

The advantages of using p-Si diodes include high sensitivity, small volume, good spatial resolution and real time response[58].The small geometry of silicon detectors is possible due to the materials relatively high density and low energy production per charge pair compared with air ($W_{silicon} = 3.68$ eV, $W_{air} = 33.97$ eV), giving it 18000 times higher signal per volume[59]. A short charge carrier lifetime of approximately 5 μs is conducive to fast response times. However, there are a number of corrections required to facilitate accurate measurements (e.g. energy, temperature, sensitivity) and they have poor energy resolution. Indirect recombination prevents complete charge collection in the diode. The rate of indirect recombination is related to the presence of defects in the substrate; radiation induced defects mean diodes have a finite lifetime. The density of electron-hole generation also has bearing on sensitivity and indirect recombination rates. At changing instantaneous dose rates a correction is required due to excess carrier concentration. This specifically relates to the increased population of minority carriers, which creates an imbalance in recombination rate (lack of recombination centres) and hence a change in sensitivity due to the collection of these excess minority carriers. For example, dose-per-pulse correction factors are required if measurements are performed away from the nominal SSD at which the diode was calibrated. Note that due to the relatively short carrier lifetime in relation to the pulse frequency, changes in average dose rate do not need to be corrected.

New diodes exhibit a sharp decrease in sensitivity as a function of accumulated dose; it is therefore recommended that diodes be pre-irradiated before use[58,60]. This decrease in sensitivity is a result of the production of new recombination (defect) centres within the diode crystal. Pre-irradiation aims to induce enough radiation damage such that the generation of these recombination centres reaches an equilibrium state. Thus, the pre-irradiation also decreases temperature and dose per pulse dependencies[60].

p-Si diode measurements taken at depths or in fields where low energy scattered radiation supplies a majority of the dose exhibit an energy dependence as the diodes are not tissue equivalent at energies used for radiotherapy[58]. This can be seen in the deviation between mass energy absorption coefficients for silicon and water at these energies, which can be up to a factor of 7 times different[59].

Diodes can exhibit directional dependence, according to their geometry. This is somewhat mitigated for cylindrically designed diodes, due to better symmetry of the active volume in relation to beam angle of incidence. Diodes are designed to be used in a specific orientation, with a directional dependence correction applied when there is deviation in measurement setup. This correction is dependent on energy and field size[58].

The small volume of the diodes allows them to be placed in large arrays. The small detector size also has the advantage of reduced volume averaging effects. This is of particular advantage in highly modulated fields, where it is not uncommon for there to be steep dose gradients.

Diodes are not absolute dosimeters, and require calibration against an appropriate ionisation chamber (i.e. one calibrated at a primary standards dosimetry laboratory). Diodes should be calibrated at the dose rate and in the energy spectrum which they are to be used, for reasons of dependency mentioned above.

Magnetic field compatibility: Like ionisation chambers, solid state detectors are also subject to corrections according to the magnetic field orientation, strength and detector orientation/geometry. Two solid state point detectors, a PTW 60003 diamond detector and a IBA PFD diode have been investigated by the Cross Cancer Institute in Canada[61]. The same approach was used as for ionisation chambers, with both inline and perpendicular magnetic fields (in range 0 - 1.5 T) and multiple detector orientations with respect to the photon beam tested via Monte Carlo simulation (with some experimental measurements for validation). Dose response was again assessed relative to the zero field case. In the inline magnetic field orientation (for all detector orientations) there is little change to dose response (max. 1% at 1.5 T), however in the perpendicular magnetic field the response was affected by up to 20%.

It appears the dose response is less dependent on detector geometry in the inline field - both the diamond detector and diode had modified geometries tested (e.g. no air gap for diamond detector, no tungsten shield for diode) with no change. In the perpendicular magnetic field, both detectors' response varied depending on geometry. The group also compared measurements to water, and found that the detectors did not accurately model water dose in the penumbra (approximately 7% difference).

O'brien et al reported on the use of diamond (PTW 60019 microDiamond) and diode detectors (PTW 60016 Diode P and PTW 60018 Diode SRS, shielded and unshielded respectively) for relative dosimetry in a 1.5 T perpendicular magnetic field[50]. PDD measurements for 10 cm x 10 cm field size showed consistent result for ionisation chamber, diode and diamond detectors. When the field size was reduced to 2 cm x 2 cm the diode and diamond detectors behaved similarly, however the ionisation chambers measured a slightly less shallow PDD for depths greater than 5 cm, by approximately 1%.

The detectors were also used to measure beam profiles. There was an apparent lateral shift in field position when measuring field profiles for the farmer chamber, which was 2.16 mm. This apparent lateral shift can be attributed to the lateral shift in EPOM of ionisation chambers in a magnetic field. Diode detectors showed a much smaller shift, 0.54 mm and 0.82 mm for the shielded and unshielded diodes respectively. Monte Carlo simulations indicate that the true shift is 1.55 mm; hence the diode detectors underestimate the lateral shift in field position in a 1.5 T perpendicular magnetic field, and ionisation chambers overestimate it. The underestimation in the case of the diodes can be attributed to their higher density, particularly in the case of the shielded diode. Due to their higher density, there is a higher probability of scatter interactions and more likelihood of electrons experiencing a shorter helical trajectory because of it. The authors do not recommend the use of shielded diodes for relative dosimetry measurement in magnetic fields, however the unshielded diode is suitable for PDD and beam profile measurements (although a shift correction may be required for lateral field position).

2.3.2 Array detectors

A 2D detector array has been reported in the literature for magnetic field applications, the IC PROFILER^{TM} (Sun Nuclear Corporation, Melbourne, FL, USA), as well as a quasi-3D detector, the ArcCHECK-MR^{TM} (Sun Nuclear Corporation, Melbourne, USA).

IC Profiler^{TM}

Mode of operation The IC Profiler^{TM} (Sun Nuclear Corporation, Melbourne, USA) is an array of 251 vented parallel plate ionisation chambers (sensitive volume 0.05 cm^3). The chambers are arranged along four axes: radial (Y), transverse (X), positive diagonal and negative diagonal (see Figure 2.2). The detector pitch is 0.5 cm along the primary axes and 0.71 cm along the diagonal axes. The array forms a total detection area of 32 x 32 cm^2. Chambers along the diagonal axis differ in shape from the primary axes, being slightly curved in shape. Prior to commencing a measurement session the device collects a "background" reading for each chamber, whereby electrical current present in the absence of radiation is quantified and subtracted from the subsequent measurements. The devices power supply was substituted for an external one, that could be placed outside the high field strength region of the MRI system.

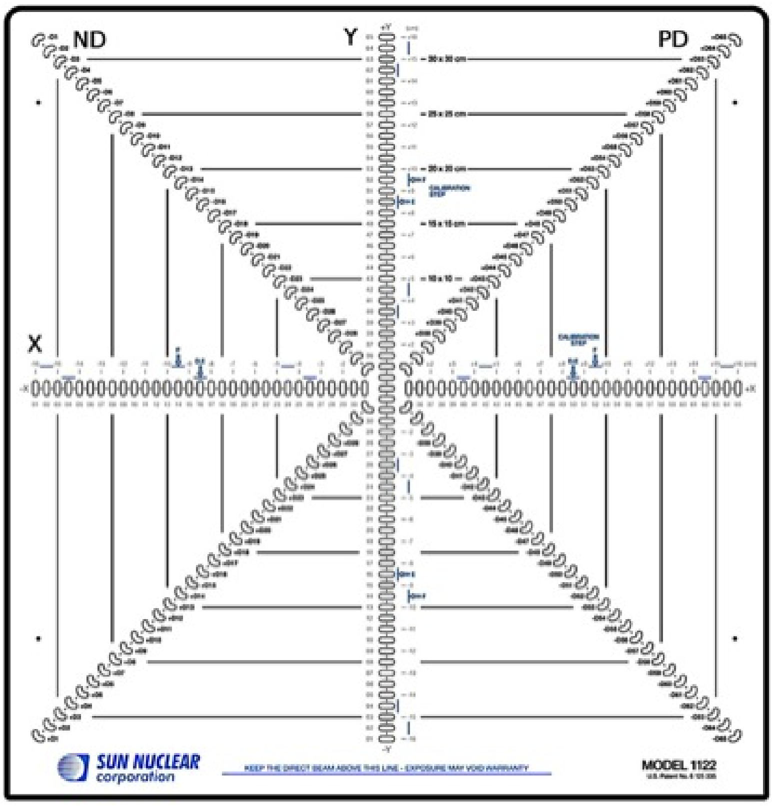

Figure 2.2: Schematic of the IC PROFILER^{TM} geometry, top view. Figure taken from Smit et al 2014.[52]

Magnetic field compatibility The performance of the IC PROFILER^{TM} has been characterised in a 1.5 T perpendicularly oriented magnetic field[52]. The ionisation chamber array was characterised to assess short term reproducibility, linearity, output factors, pulse rate frequency (PRF) dependence, leakage current, panel orientation and ionisation chamber shape. Profile measurements collected with the device were validated with Gafchromic EBT2 film measurements. The panel's array calibration was performed in 0 T conditions on a conventional linac.

Short term reproducibility was assessed by determining the coefficient of variation of 10 consecutive measurements. Possible warmup effects were also investigated by comparing data points collected for the initial 15 seconds of beam on time to the remainder of the measurement period. There was found to be no difference in the reproducibility of the device in the MRI-linac system, compared to a conventional linac, nor any warmup effects.

The linearity was assessed by delivering a range of monitor units to the device, from 20-500MU (no dose range specified). A separate, reference ionisation chamber was used to rule out machine output variation. The response of the device was linear to within 0.2% in both 0 T and 1.5 T conditions.

Output factors were calculated for field sizes 5.6 x 5.6 cm^2 to 23.8 x 23.8 cm^2 for ionisation chambers in the central 3 cm of the panel, as well as with a reference NE2571 chamber for comparison. Output factors deviated less than 0.4% than from those calculated using a the NE2571 chamber in the MRI-linac.

PRF dependence was assessed at two frequencies, 240 Hz and 120 Hz; variation in linac output was corrected for with a reference NE2571 chamber. There was approximately 0.5% observed variation in response with the change in PRF between 0 T and 1.5 T conditions.

The impact of a 5° panel rotation was quantified and found to be small, with less than 0.2 % average difference with and without a magnetic field. There was a slightly larger change (1%) in the penumbral regions, but it was attributed to a possible lateral shift in position from imperfect rotation.

It was observed that the leakage current of chambers was larger in a magnetic field. This was minimised by recalculating background and dark current corrections 15 mins after the panel was placed in the magnetic field.

The influence of ionisation chamber shape was quantified by rotating the panel 45°, such that the diagonal axes composed of rounded chambers were sampling the primary axes of the beam. The influence of ionisation chamber shape was minimal but could not be neglected completely, as there was a noticeable change in profiles when the chamber orientation and/or shape was inconsistent through the profile (i.e. the central chamber is shaped and oriented differently to those on the diagonal axes, see Figure 2.2).

Validation with film using 2%/2mm gamma criteria shows generally good correspondence, although there was a tendency for more points to fail along the diagonal axis (1% of points failing vs. 4% on diagonal), where the chamber shape differs.

Overall, the magnetic field affected the panel in a limited manner. Its use as a relative dosimeter, where results are normalised to the response of one detector, negated the need for magnetic field correction factors typical of absolute dosimetry measurements. However, comparing the unnormalised values of ionisation chambers on more than one axis was not recommended.

ArcCHECK-MR^{TM}

Mode of operation The ArcCHECK-MR^{TM} (Sun Nuclear Corporation, Melbourne, USA) is a magnetic field compatible modification of the original ArcCHECK^{TM} device, such that the power supply to the device is able to be situated outside the high-strength magnetic field. It is comprised of an array of 1386 diodes arranged with 1 cm pitch in a spiral pattern, in a hollow cylindrical PMMA phantom (see Figure 2.3) at 3.3 cm water-equivalent depth. It also has a removable insert that can be fitted to the central hollow of the device to house an ionisation chamber. The device is designed for patient-specific QA, an important part of clinical workflow to ensure the planned and delivered dose are comparable within a pre-defined tolerance.

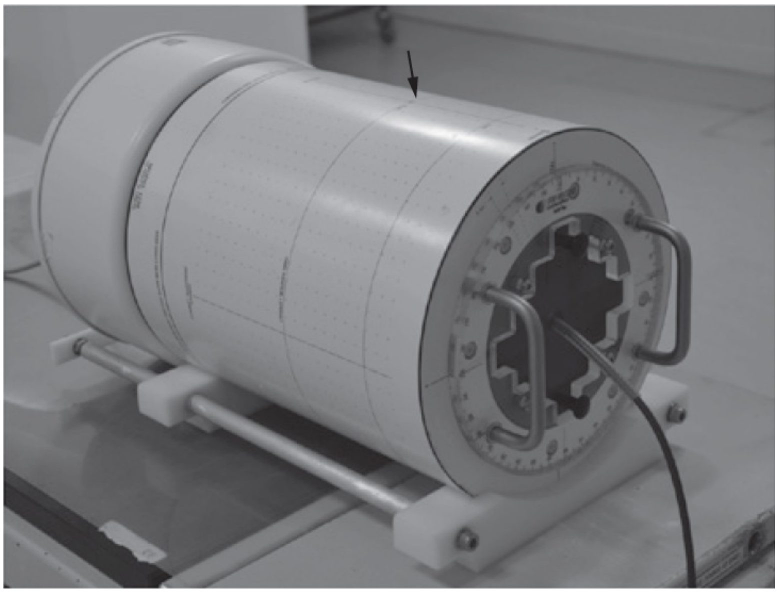

Figure 2.3: The ArcCHECK-MR^{TM} patient specific QA device. The arrow indicates the reference diode. Figure taken from Houweling et al 2016[64].

Magnetic field compatibility The ArcCHECK-MR^{TM} was first used as a patient specific QA device in the ViewRay MRIdian system, a 0.35 T strength MRI machine combined with a Co-60 source, in a perpendicular magnetic-field-to-photon-beam orientation[62]. The device was presented as one component of a five-pronged approach to IMRT QA. A representative set of modulated plans were delivered to the device. Gamma analysis was used to compare planned and measured dose distributions, using a 3% dose difference (relative, global normalisation) and 3 mm distance to agreement criteria. High gamma pass rates were observed. A 2%/2 mm criteria did not yield appropriate pass rates, which the authors attribute to to the inability to apply angular dependence corrections to the device, since the MRIdian delivers dose simultaneously from three Co-60 sources. The device was further investigated in the MRIdian system, with corrections proposed to correct for magnetic field effects suspecting to be causing ArcCHECK to measure a response higher than that predicted by the treatment planning system[63]. However, the corrections applied proved inadequate, because it is an intricate combination of dose deposition and diode response changes that contribute to the change in response.

The magnetic field compatibility of the modified ArcCHECK device was also tested at the UMC Utrecht MRI-linac facility, which is a 8MV linear accelerator configured with a MRI device of 1.5 T magnetic field strength in a perpendicular orientation to the primary radiation beam[64]. The group did a comprehensive radiation characteristic comparison, including short term reproducibility, dose linearity, dose rate dependence and inter-diode dose response variation. Characterisation of the device on the MRI-linac were compared to that on a conventional 6MV linac. The array calibration collected on the conventional linac was applied in both circumstances.

The short term reproducibility of the device was evaluated from consecutive readings of one diode in the array, with no significant difference found between 0 T and 1.5 T conditions.

Dose linearity of the same diode was assessed for a range of 2 - 500 MU (no absolute dose range given), and was observed to be better than 0.5% in both 0 T and 1.5 T conditions. The dependence increased for monitor unit deliveries below this, however it is unclear whether this was due to output stability of the linac itself (authors quote an expected 0.1% stability); an ionisation chamber could have been used as an external reference to further investigate this effect, however the magnitude of the effect (max. 2.1%) is unlikely to affect the recommendations regarding appropriateness of the device for use in a 1.5 T magnetic field.

The dose rate dependence of the same diode was assessed by varying the monitor units delivered per minute. The authors were unable to compare exactly the same dose rate for each system, as the MRI-linac and conventional linac do not have identical beam generation systems; the MRI-linac is an unflattened beam compared to the flattened conventional linac, which inherently deliver different dose rates. A similar trend in dose rate dependence was observed for both conventional and MRI-linac, with a maximum deviation of 1% from the nominal dose rate on both machines.

Field size dependence was assessed for field sizes 2.9 x 2.9 cm^2 to 28.5 x 28.5 cm^2 by normalising the response of the same diode to a 10 x 10 cm^2 field size. Due to differences in the SSD and collimation systems of the MRI-linac and conventional linac, exactly the same field sizes were not able to be used in each setup. Instead, a trend in field size dependence was compared rather than a direct comparison of output factors. A similar trend in variation of response with field size was seen on both conventional and MRI-linac, with the maximum change in response with field size differing by 0.1% for the two machines for field sizes greater than 5 x 5 cm^2. For field sizes smaller than this, the MRI-linac over-responded by approximately 1%; this result was not investigated further; if the device is to be used for verification of small fields, this effect warrants further investigation.

The dose per pulse dependence was assessed by comparing the reading of opposing diodes in the array. This is a somewhat limited assessment, due to the inability to adjust table height in the MRI-linac. Interdiode dependence was ruled out by rotating the array to interchange the position of the diodes. The dose per pulse dependence was determined to be of insignificant difference between the two machines. This is difficult to definitively assess given the method, due to the different beam qualities of the two machines and possible effect of the magnetic field on the depth dose distribution.

Interdiode dependence was assessed by performing several rotations of the device so a different diode was placed in the position of the reference diode, and irradiated at a fixed gantry angle. The paper does not specify how the array calibration is performed for the device, so it is unclear whether the diodes evaluated are a true test of the individual sensitivity calibration and hence the interdiode dependence. The standard deviation in the measurement on both machines was of similar magnitude.

The authors recommend the ArcCHECK-MR^{TM} device suitable for use as a patient specific QA device in the 1.5 T MRI-linac system. It should be noted however that no patient plans (or plans of dynamic/modulated nature) were delivered to the device as part of the reported study.

2.4 CMRP dosimeters

This section details the silicon array dosimeters, designed by the CMRP, that will be investigated in this thesis for their suitability for use in magnetic field environments. Both dosimeters have previously been characterised in terms of radiation response in the zero magnetic field scenario.

2.4.1 MagicPlate-121

The MagicPlate-121 was originally designed as a transmission detector, to measure 2D fluence maps of radiation beams when mounted to the linac head. The consequently thin, minimally-perturbative design of the dosimeter is expected to be an advantage for MRI-linac applications, which are arguably more sensitive to density changes. It is pictured in Figure 2.4.

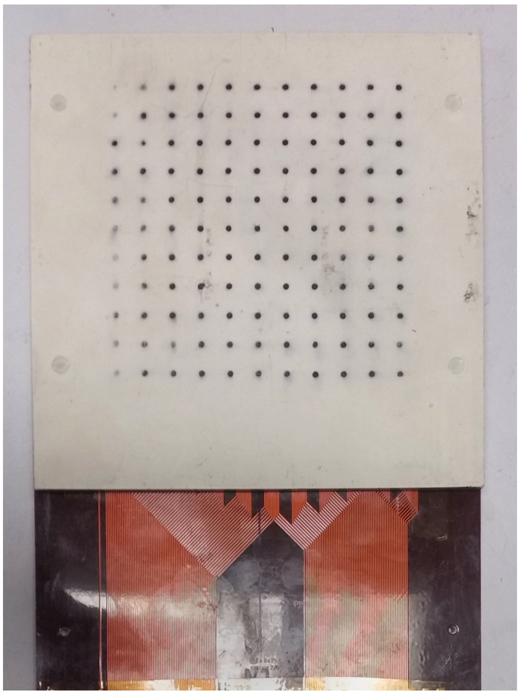

Figure 2.4: The MagicPlate-121 dosimeter.

The Magic Plate 121 is an array consisting of 121 silicon diodes (1.5 x 1.5 x 0.38 mm^3) embedded in a kapton substrate 650 μm thick. The diodes are mounted using a "drop-in" technology developed at the CMRP. They are epitaxial, with a 50 μm thick layer grown on a low resistivity p+ substrate. The diodes are spaced evenly in an 11 x 11 square matrix formation, 1 cm apart, covering a total detection area of 10 x 10 cm^2. The design avoids the use of heavy metal contacts above the sensitive area, to minimise energy dependence, by using thin aluminium contacts on the periphery instead. The diodes are also pre-irradiated, to resolve sensitivity issues due to radiation damage. The detector is operated in passive mode, where no bias voltage is applied.

The radiation response of the array has been characterised by Wong et al[65]. The array shows good reproducibility (2.1%), dose linearity and dose per pulse rate independence at typical IMRT delivery dose rates, but showed a decrease in response at higher dose rates. Depth dose plots agreed to ionisation chamber measurements to within 0.7%. There was some over-response at low photon energies, as well as some angular response dependence (but within 3.5% for gantry angles smaller than 75°), both of which are characteristics consistent with other silicon detectors.

The array had a transmission factor of 1%. The thin, radiation "transparent" nature of the array means that in addition to in-phantom uses, it has also been deemed appropriate for transmission measurements when placed in the accessory slot of the linac head.

For clinical implementation it is suggested that a uniformity correction be applied, to correct for slight differences in the response of individual diodes. This is determined by the ratio of an individual detectors' response to that of a reference diode, when each is placed at the centre of a flat radiation field. For robustness, this process may be repeated to determine the final uniformity correction from an average of corrections calculated using several different reference detectors.

Alternate applications of the array include high dose rate brachytherapy quality assurance[66,67].

2.4.2 MagicPlate-512

The MagicPlate-512 (M512), also designed at CMRP, is a new-generation radiation dosimetry system. It is pictured in Figure 2.5. It consists of a thin monolithic p-type silicon wafer (52 x 52 x 0.47 mm^3) with 512 ion-implanted diodes (0.5 x 0.5 mm^2). Diodes are spaced evenly with 2 mm pitch, covering a maximum detection area 46 mm wide. The pitch of the diodes provides a higher density of measurement points than other commercial diode/chamber array dosimeters currently available. As is further described in the following section, the dosimeter has a fast FPGA-based read-out system with 8 x 64-channel AFE0064 (Texas Instruments) chips, and is synchronized with the linac to allow read out of all pixels pulse-by-pulse[68,69]. Like the MagicPlate-121, the M512 operates in passive mode.

Aldosari et al[70] characterised the radiation response of the M512, finding it to be appropriate for photon beam dosimetry. It showed good dose linearity, reproducibility and depth dose measurement agreement to within 1.3% of ionisation chamber measurements. There is some dose per pulse dependence (up to 5% at dose rates below 1.5 x $10^{-}5$ Gy/pulse). The detector measures FWHM well (compared to film), but slightly over estimates penumbral width (by 0.4 mm on average). For field sizes less than 1 x 1 cm^2, output factor measurements are overestimated (4%), due to scattering occurring within the silicon die. A small air gap is used to

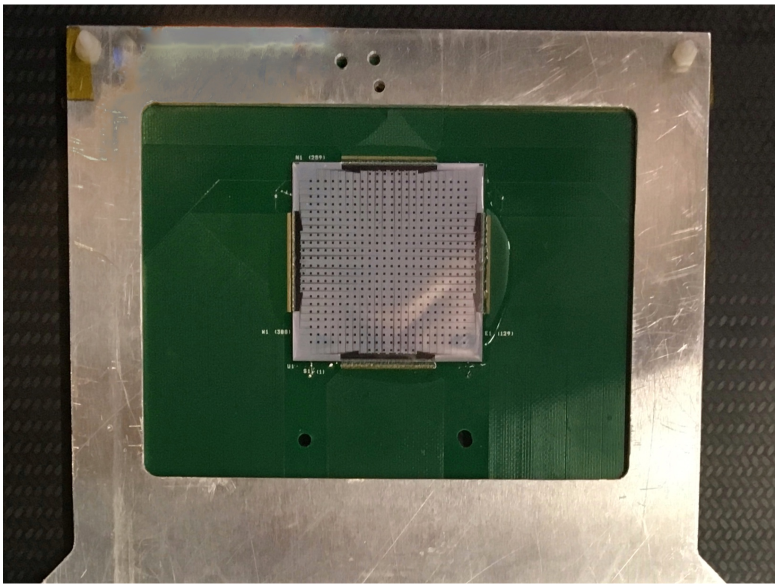

Figure 2.5: The MagicPlate-512 dosimeter.

counteract this dose enhancement. Otherwise, output factor measurements agree to within 2% of diamond, diode and MOSKIN detectors.

Uniformity correction is necessary, to adjust for small inherent variations due to diode sensitivity and gain of preamplifier channels. The array response is equalised by calculating a uniformity correction factor, based on the mean response of all pixels in a flat-field scenario, when the detector is placed at 10 cm depth in a water phantom and irradiated by a 20 x 20 cm^2 photon beam.

Stansook et al[71] have characterised the angular response of the detector. The M512 is insensitive to small angular deviations, with corrections for angular response not exceeding 1% for angles ±30° from orthogonal incidence, for field sizes in the measurable range.

The M512, with its closely pitched diodes, is specifically designed for small field applications, and has been used in the quality assurance of motion adaptive stereotactic radiotherapy[72]. Its high density of measurement pixels is expected to be useful for profile reconstruction and 2D dose mapping for the MRI-linac.

2.4.3 Read-out electronics

The data acquisition system (DAS) used for both the MagicPlate-121 and MagicPlate-512 are similar in their principles of design. The details of the system can be found in a publications by Fuduli et al[68,69]. A picture of the electronics as it is configured for the MagicPlate-512 is shown in Figure 2.6. Both systems are multichannel, to accommodate data from the 121 and 512 detection channels of the two detectors, respectively. The DAS is required to be fast; the system read-out in synchronised with the beam pulses of the linac such that the detectors integrate only while the beam is on, to minimise dark current effects. The integration time is typically set to approximately 52 μs (minimum selectable time is 14 μs) to encompass the entire beam pulse.

The DAS analogue chip used is an AFE0064 (Texas Instruments), coupled with a 16-bit quad (64 total) channel ADC. The system is equiped with 2 chips in the case of the MagicPlate-121, and 4 chips in the case of the MagicPlate-512 in order for all channels to be read out simultaneously. The DAS communicates with a Field Programmable Gate Array (FPGA) master board, which uses a USB2.0 connection to relay information to the graphical user interface (GUI). The system has a dead time of 70 μs for read out. This occurs in the time between beam pulses.

Acquisition is controlled through a custom-designed GUI. Integral and frame-by-frame data can be visualised on the GUI. The GUI also has the ability to apply post-processing algorithm, such as apply a gain equalisation matrix. Dose profiles can also be analysed immediately following an acquisition.

The raw charge collected by the detector needs to be scaled according to the selected gain range used for acquisition. This is done by multiplying the raw “counts”, which are normalised to the AFE0064-specific range factor, by the maximum charge for the corresponding range. This charge can then be used to establish a linear relationship to dose, by irradiating the detector by known amounts (in a similar fashion as is used for the film net OD - dose conversion).

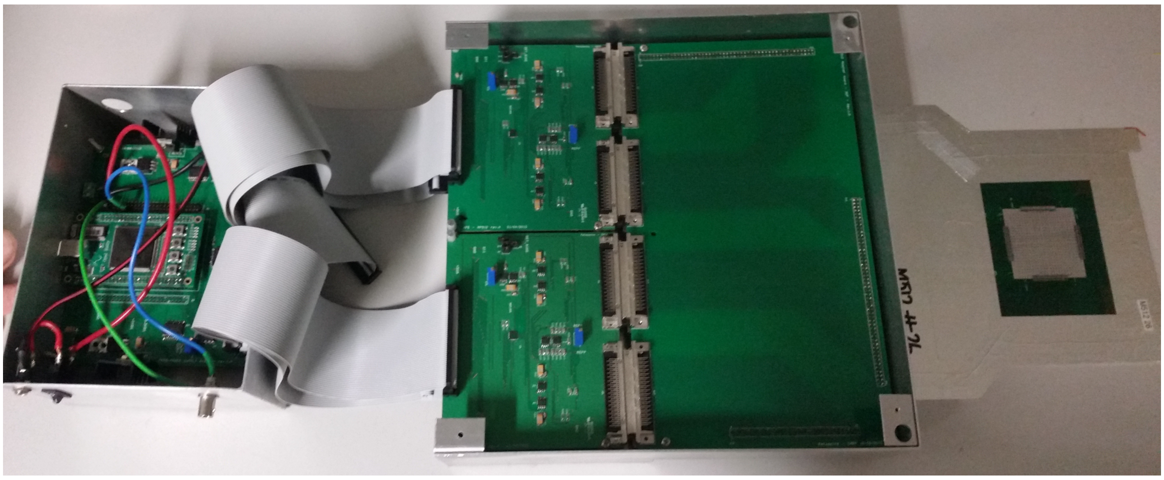

Figure 2.6: The MagicPlate-512 dosimeter, with attached read-out electronics.

2.5 Radiochromic film dosimetry

Early film dosimetry was performed using radiographic film, composed of a gelatin emulsion containing radiation-sensitive silver-halide crystals with an outer coating to provide structure. A chromatic change due to radiation exposure was linearly related to dose. It required chemical development to evaluate the dose response, as well as special storage and handling procedures due to its sensitivity to ambient light. Film dosimetry technology has since progressed to a more user-friendly form, with the advent of radiochromic film. Radiochromic film instead utilises polymerisation as a measure of dose. Upon interaction, a chemical change is initiated within the photomonomer molecules (specifically, diacetylenes), which are suspended in a gelatin solution to create the sensitive layer. This results in colour formation that is related to dose through a logarithmic-based measure referred to as net optical density. Radiochromic film is "read out" using a high quality flatbed scanner. Radiochromic film has the advantage over radiographic film of being thinner, does not require chemical post-processing, is relatively insensitive to ambient (room) light, has less spectral sensitivity (radiographic film showed non-linear sensitivity to photons in 10-200 keV range) and are more tissue equivalent[73].

Radiochromic films are a popular choice for high resolution 2D dose measurements, in applications where a real-time response is not required. As is summarised in reviews by Williams et al[73] and Butson et al[74], the response to dose is well defined and has a large range of sensitivity (as low as 1 cGy), film has high tissue equivalence, have a near linear energy dependence, and negligible energy dependence (except at angles of near incidence, where the OD increases by 1-2%[75,76]).

Strict procedures must be followed if accurate dosimetric results are to be obtained using radiochromic film. This includes first and foremost being consistent with orientation, as the film response varies according to the orientation of the polymers themselves; variations of 4-15% in optical density have been reported[77,78]. Film pieces should be cut from the sheet with a consistent orientation, which is also maintained in the scanning process. The manufacturer of Gafchromic EBT3 film recommends scanning in landscape orientation; there is a difference in calibration curves produced in portrait vs landscape mode, as reported by Williams et al[73]. For EBT3 films there is no difference in optical density between different sides of the sheet[79].

When performing an experiment, it is advised to use film from the same batch, and preferably from the same sheet, as the specific composition of the active layer has been known to vary[80].

Flatbed scanners are commonly used, and recommended by the manufacturers, for readout of radiochromic film. They consist of a charged coupled device (CCD) detection system and light source (white fluorescent light or Light Emitting Diode (LED)) which move in tandem to scan an image by measuring transmission through the film. An appropriate scanner for film dosimetry is one that has a linear response in light detection, high sensitivity of detectable OD, spectral efficiency and adequate resolution of digital output (16-bits of digitization per RGB channel)[73]. The file should be saved in TIFF format, to preserve image data. Also to be considered is the noise introduced by the scanner, which increases with the scanned dpi; and dust on the scanner will also introduce noise[73]. Scanners with fluorescent lamps (such as the EPSON 10000XL scanner used in this thesis) should also be warmed-up before use[81,82], typically for 30 mins. LED-based systems do not require warm-up. Uniformity of the scanner, particularly in the direction parallel to the light source, is well reported for CCD systems[77,82–86]. The impact of non-uniformity can be somewhat managed by limiting the scanning area to the centre of the bed, where uniformity is highest.

Net optical density is calculated according to the following equation[81,87,88]:

$$OD = log_{10}\left(\frac{I_0}{I}\right) \tag{2.3}$$

where I_0 is the initial (pre-irradiated) intensity, and I is the transmitted intensity (post-irradiation). To relate net optical density to dose, a calibration set of film is irradiated to known dose levels. Optical density is then plotted against dose, with a 3^{rd} or 4^{th} order polynomial fit used to define the relationship. Films should be scanned at least 24hrs after irradiation, to allow completion of the polymerisation process[89,90]. When calculating I, a single colour channel should be used for analysis to increase sensitivity according to the exposure. The red channels peak sensitivity wavelength range (600-650 nm) is preferred for Gafchromic film, whose peak absorbency is in this range[73].

The details regarding the properties of radiochromic film discussed above apply to Gafchromic EBT3 film (ISP Inc., Wayne, NJ, USA), which is used as the reference dosimeter in this thesis against which CMRP detectors are benchmarked. It was chosen for its high resolution, thin structure, atomic composition close to water, large dynamic range and established history in radiation therapy applications. It is assumed that the polymerisation process is not affected by the presence of a magnetic field; a safe assumption considering the polymerisation process is based on chemical changes rather than direct ion collection.

2.6 Monte Carlo toolkits for radiotherapy

2.6.1 General Overview

Monte Carlo methods use individual particle transport, based on random number generation and interaction probability distributions, to determine dose distributions from first principles. The sum of energy deposition along individual particle trajectories, including that of primary and secondary particles, is used to calculate a voxelised dose distribution, with energy deposition in a given voxel divided by its mass to obtain dose. The stochastic nature to Monte Carlo means that no two simulations have the same pattern/sequence of energy distribution (excluding the case where the same random number generator seed and number of particles is used for simulations that are identical in geometry and transport parameters). This introduces a statistical uncertainty, however, a degree of reproducibility is still achieved in terms of the final result. This is in contrast to analytic approaches, where convergence to a singular solution means statistical uncertainty is not present. This is not to say uncertainty does not exist for analytic methods - in this case uncertainty is systematic, instead born from errors in the model parameters themselves. Monte Carlo methods prevail in accuracy over analytic methods in complex geometries, especially when physical and radiative interaction properties vary significantly from that of water. This has been clearly demonstrated in phantom-based studies[91–94]. Analytic methods employ many approximations to reach a solution, which can fall down in increasingly complex geometries, however they have the advantage of fast calculation times - the major inhibitor (computing power) of widespread use of Monte Carlo in radiation therapy treatment planning.

Components of a Monte Carlo code, despite the toolkit, commonly require definition of the geometry of the medium (including material properties) in which particle transport will be modelled, as well as definition of the primary particle type, energy, angle of incidence and the number of histories. The number of histories will determine the statistical uncertainty, which follows Poisson statistics, meaning the uncertainty decreases with the square root of the number of initial particles. Scoring grids to extract information from the simulation, such as dose deposition or energy spectra, are also required. A physics model is often hard-coded, which defines how transport occurs. Parameters may also be defined as to how the particle is transported, and the threshold below which transport ceases (e.g. energy cut-offs).

A “step” is common terminology for the transport of a particle to its next position. The components of a step include:

- distance to next interaction
- type of interaction, which for photons includes photoelectric effect, Compton scattering, Rayleigh scattering or pair production

- angle and energy following interaction
- secondary particle generation from interaction

Electron transport consumes most of the calculation time for primary-photon simulations, due to the many small interactions that take place for a single photon history. Various methods of condensing interactions are used to help mitigate this, for example using a continuous slowing down approximation (CSDA) for electrons below a certain energy threshold.

Random number generation is core to Monte Carlo codes, and is used to define each history's initial condition. This is to ensure that each history in a simulation is unique to it. Uncertainty in simulations estimated by simulating several runs, or batches, of a simulation with an identical number of histories. The average of the runs is taken, and uncertainty computed as the standard error.

Variance reduction techniques are used to improve the efficiency of a simulation, with regard to the computation time required to achieve a given level of statistical uncertainty. These techniques are not based on large-scale assumptions where particle transport is concerned; rather they should be implemented to improve the efficiency with which particle transport factors are considered. Variance reduction techniques include the previously mentioned energy-cuts and condensed interaction history, as well as particle splitting (effectively increases the number of particles reaching the volume) and step size selection, to name a few. It goes without saying that the impact of variance reduction techniques on the final outcome should be carefully considered - especially if the technique reduces the calculation time per history by simplifying the physics of transport. They are nonetheless crucial to efficient Monte Carlo simulation, and can be implemented with minimal uncertainty contribution.

In practice, the long calculation time of Monte Carlo can be inhibitive. As such, superposition/convolution algorithms have been widely implemented, which utilise Monte Carlo to generate pre-computed dose kernels, which are convolved in the patient geometry. This has improved accuracy over pencil beam techniques without the long computation time of a direct Monte Carlo model. Going a step further, Voxel Monte Carlo (VMC) system (Kawrakow 2000) is a direct Monte Carlo system whose implementation of variance reduction techniques improves efficiency to a clinically acceptable degree. It takes two slightly varying forms, XVMC (Fippel 1999) and VMC++ (Kawrakow 2000a). They differ in the simulation of the accelerator head; XVMC uses a virtual source method, whereas VMC++ uses directional radiative splitting. XVMC is currently implemented in the treatment planning system Monaco (Elekta CMS, Maryland Heights, MO).

In the following sections, the most commonly used Monte Carlo toolkits in radiation therapy applications will be discussed: GEometry ANd Tracking (GEANT) and Electron Gamma Shower (EGS).

2.6.2 Geant4

The GEANT4 Monte Carlo toolkit[95] is based on the GEANT3 application, which was written in FORTRAN. In 1993 redevelopment began, written in C++, and the GEANT4 collaboration was established in 1999. The GEANT4 collaboration is based at CERN, but is developed by collaborators worldwide. The toolkit was originally developed for applications in high energy physics, but development has further expanded to the fields of space and medical physics research. Individual applications are built using GEANT4 classes, as well as user defined classes, and are highly customisable.

Simulation studies in this thesis were performed using GEANT4 version 9.6.p02. This toolkit was chosen for a number of reasons, such as:

- Complex geometries can be modelled
- Tried and tested for the medical physics applications used in this thesis
- Ability to implement magnetic fields and have appropriate particle tracking in such situations
- Can model large variety of particles
- Free/open source

The main method is implemented by two toolkit classes, G4RunManager and G4UI manager. G4RunManager controls flow of the application, and manages event loops. G4UIManager is a user interface manager. There are three fundamental classes required to form the basis of your simulation; Detector Construction, Physics List and Primary Generator Action. Each requires a header file for class definitions, and a source file for class method definitions.

Detector Construction contains geometric information pertaining to the simulation; any physical objects to be included in the simulation are created here. It is where the desired dimensions and material composition, as well as scoring volumes and particle step limits for specific volumes are specified. A ‘solid’ volume contains shape and dimension information. A ‘logical’ volume includes properties of the volume (e.g. sensitive detector). A ‘physical’ volume defines the placement of the longical volume. Volume placement is done in terms of the coordinate system of it’s ‘mother volume - the volume in which it is contained. Each volume must be placed within a world volume. Volumes must not overlap. Magnetic fields can also be implemented here. To score dose, the detector construction class is modified to create a ‘sensitive detector’ class. This will accumulate energy deposition for an ‘event’.

The Physics List contains information on particles and physics processes needed, and is also where cut values for particles are set. A tracking cut, or range cut, places production thresholds on secondary particles. If a particle is produced, it is tracked until zero energy, or until it exits the world volume. If a secondary particle is produced with a projected range below the range cut, it is not tracked and it is assumed all energy is deposited at the production point.

Primary Generator Action controls primary event generation: how many, from what location, particle type, energy, momentum vector and/or recycle number. Input types used in this thesis include (but are not limited to) custom gun, general particle source (GPS) and phasespace files.

Other classes such as Run Action, Stepping Action and Event Action can also be utilized. Stepping Action can be used for dose scoring; energy deposition is collected for a specified volume (or in a grid covering multiple volumes) step by step. Event action is responsible for event by event accumulation of deposited energy. Run action computes total energy deposition/dose/track lengths etc. at the end of a run.

GEANT4 simulations are run in either an interactive or batch mode. In interactive mode, the built application is called and a user interface is used to execute desired commands, such as initiating a nominated number of histories. Specific information on the particle history can be generated and viewed if the user would like to view tracking information in detail. Simulations can be visualised using an OpenGL library in interactive mode. Alternatively, in batch mode, a macro file which contains a script of several user interface commands can be executed without user interaction. Interactive mode is useful for troubleshooting, and batch mode for long-computation finalised application executions.

Several publications have utilised the GEANT4 toolkit to model radiation transport in magnetic fields, specifically as it relates to MRI-linac dosimetry[31–33,35,37,42,43,45,48,54]. A number of these publications have included a benchmarking component, involving experimental verification of simulations, the results of which highlight the high accuracy that can be achieved when utilising GEANT4 for modelling dose to medium changes in the presence of a magnetic field. The specific parameters used to model magnetic fields in simulations used for this thesis are described in detail in the chapters following.

2.6.3 EGSnrc

EGS3 released in 1978, based on a electron-photon Monte Carlo FORTRAN code developed by Nagel (Rheinischen Friedrich-Wilhelms-Universitaät) that was further developed by Ford and Nelson (SLAC). EGS4 (Nelson et al 1985) was later released, which through collaboration with Nelson (SLAC), Hirayama (National Laboratory for High Energy Physics) and Rogers (NRC) improved the modelling of high energy accelerators, and low energy handling, among other things. EGSnrc (Kawrakow and Rogers 2000) was then released in 2000, which featured a more sophisticated electron transport model regarding multiple scattering theory, which uses Rutherford elastic scattering theory. EGS codes are programmed in MORTRAN, a macro form of FORTRAN.

BEAMnrc (Rogers2007), based on EGS4, is popularly used in radiation therapy to model linear accelerators in order to generate phase space files - data sets that characterise the particle fluence (including energy, position and direction) exiting a linear accelerator. These phase space files are generated by complete simulation of the beam forming components of the linear accelerator, from the point electrons enter the waveguide to when the subsequently produced beam exits the accelerator head. Each of the beam forming components (e.g. target, flattening filter, collimators) are modelled in 3D according to specification. The phase space file can be used as input for subsequent simulations, for example in DOSXYZnrc (Walters2007) if using an EGS-based code, or in a Geant4 application.

A modification of the combined BEAMnrc and GEANT4 model created by Oborn et al[45] was used as the basis for Monte Carlo simulations in this thesis. The model was adapted to simulate radiation transport in magnetic fields; the specific parameters used to model magnetic fields in simulations used for this thesis are described in detail in chapters 4 & 5. BEAMnrc[96] was used to simulate the linac treatment head, to produce machine-specific phase space files at the level just below the MLCs, in IAEA format. The components of the linac included in the simulations were the x-ray target, primary collimator, exit window, flattening filter, monitor ionisation chamber, mirror, jaws and a Millenium 120 leaf MLC. These phase space files were used as input for radiation transport and dose calculation using GEANT4, implementing the Livermore Low-Energy physics model.

Chapter 3

Dose spread array distortion by inline and perpendicularly aligned magnetic fields

The results presented in this chapter relating to dose spread array perturbation by magnetic fields in water and silicon have been published in the journal Medical Physics:

M Gargett, B Oborn, P Metcalfe and A Rosenfeld, Monte Carlo simulation of the dose response of a novel 2D silicon diode array for use in hybrid MRI-LINAC systems, *Medical Physics*, vol. 42, no. 2, pp. 856-865, 2015.

3.1 Overview

Prior to the use of simulation CT for dose planning in radiation therapy, basic empirical dose calculation methods were used. The dose calculation accuracy was largely limited by a lack of anatomical information, rather than the dose calculation model used. As sophisticated imaging modalities became available and were adopted for treatment planning, there was more demand placed on the accuracy of dose calculation. Analytical dose calculation algorithms were developed, eventually progressing to voxel based consideration of heterogeneous tissue. Dose calculation accuracy requirements further increased along with the accuracy with which target volumes were able to be delineated on image sets. While Monte Carlo methods were recognised as the "gold standard" of dose calculation, the technology to facilitate the required computing power in the timeframes required of a clinical setting was yet to be developed. Semianalytical models, which use superposition of Monte Carlo generated dose kernels to calculate a dose distribution, were hence the compromise; it is less computationally intense to deal with implicit modelling of particle transport rather than explicit.

A kernel, the concept of which was first demonstrated by Loevinger[97,98], is an integral concept to modern treatment planning algorithms. It is defined as the energy deposition (or dose) distribution emanating from a point irradiation. A topical review written by Anhesjö and Aspradakis[99] identifies 3 general types of kernel which are referred to in the literature, the definition of which relates to the geometry by which they are generated. The first, a point kernel (also referred to as a dose spread array by Mackie, Scrimger and Battista[100], differential pencil beam by Mohan, Chui and Lidofsky[101] and point spread function by Ahnesjö and Mackie[102]), is defined as the energy deposition around a primary photon interaction site, in an infinite medium. The second, a pencil kernel, is defined as energy deposition from a monodirectional point source, in a semi-infinite medium. The third, a planar kernel, is defined as energy deposition from primary interactions in a plane lateral to an infinite broad beam. Kernels are easily calculated though Monte Carlo simulation[101–103]. While analytic methods have limited capability for the generation of kernels, analytic fitting is used to simplify the use of kernels in dose computation, for both point and pencil kernels[102,104,105].

A popular semianalytical implicit modelling method is kernel based superposition /convolution[100,101,106,107]. Weighted kernels are superimposed to create a dose distribution, following the raytracing of primary photon trajectories through the CT dataset. When the kernel is spatially invariant, convolution techniques can be used to improve efficiency. An example of semianalytic superposition/convolution model is collapsed cone convolution[104]. It improves dose calculation efficiency using the techniques of angular discretization and parametrization. Discrete angular sectors (called cones) are collapsed onto their axes when energy released from the cone axis volume is approximated to be rectilinearly transported, attenuated and deposited in volume elements along a transport line that represents the cone axis. An analytic expression may be used to describe this transport, using recursive formula; a computationally efficient method that requires only one such evaluation per voxel of the transport line. During this process, scaling of primary and scatter dose kernels is also performed to account for heterogeneities. This is the basis of some modern treatment planning system photon dose calculation algorithms such as the Collapsed-Cone Convolution (CCC) algorithm in Pinnacle (Philips Medical Systems).

Other analytic methods used in modern treatment planning systems are those that attempt to solve the Linear Boltzmann Transport Equation (LBTE). The Acuros AXB algorithm, implemented in the Eclipse (Varian Medical Systems) treatment planning system, takes an iterative approach to solve the differential form of the equation. This approach differs from semianalytic superposition/convolution approaches previously described in areas of heterogeneity, such as lung and bone, since physical interactions in the material are explicitly modelled (as opposed to applying scaling corrections to dose kernels generated in water)[108].

As will be demonstrated in this chapter, dose kernels are altered in a magnetic field, according to magnetic field strength, direction, and the physical density of the medium. In the case of a magnetic field oriented perpendicularly to the primary photon beam, kernels also suffer asymmetry. This has garnered the general perception in the scientific community that analytic methods of dose calculation will be inadequate for magnetic field applications. The Utrecht Elekta-Philips MRI-linac collaboration has exclusively explored a Monte Carlo solution, utilising a GPU-based Monte Carlo dose calculation engine developed by Hissoiny et al[10,109] and adopted by the Monaco (Elekta CMS) treatment planning system.

This chapter employs Monte Carlo simulations to investigate changes to dose spread arrays due to the presence of inline and perpendicularly oriented magnetic fields. The results of this chapter provide important context to those presented in the following chapters, by demonstrating at a fundamental level the perturbation of dose distributions in different media, at different field strengths.

3.2 Materials and Methods

The Monte Carlo simulation toolkit, GEANT4 version 9.6.p02 was used. Monte Carlo generated point spread dose arrays were calculated in silicon and water for field strengths 0.5 T, 1 T, 1.5 T and 3 T in both magnetic-field-to-photon-beam orientations. This was done by implementing a general particle source with a unidirectional 6 MV spectrum, generated from a histogram (100 keV bins). The spectrum is based a 6 MV photon beam model for a Varian 2100C linear accelerator[45]. Only particles originating in a 1 mm^3 voxel at 1.5 cm depth were tracked. The number of primary histories was 1 x 10^8 for dose spread arrays.

GEANT4 simulations that include a magnetic field have 3 primary parameters that can be adjusted to modify the chord selection for curved path approximations: miss distance, delta intersection and delta one step. These parameters specify the acceptable level of accuracy for integration approximations in order to maintain realistic computation times. The miss distance specifies the maximum distance between the midpoint of a chord and the “real” trajectory it approximates. The miss distance default value 0.25 mm was reduced to 0.015 mm with no notable change in results above the level of system noise. We settled on a conservative value of 0.025 mm; the same value was used by Meijsing et al[48]. Delta intersection is a parameter associated with systematic errors in momentum. The value is chosen to specify the positional error in the point of intersection at a boundary. Delta one step broadens the definition of delta intersection to the statistical uncertainty in the endpoint of any integration step. Delta intersection and delta one step were left at default values, 1 μm and 10 μm respectively; in keeping with the recommendation that delta intersection and delta one step not differ by more than one order of magnitude[110].

Dose kernels were generated in low-density lung (ρ = 0.217 g/cm^3), water (ρ = 1 g/cm^3) and silicon (ρ = 2.33 g/cm^3). The composition of the lung material used was for blood-filled lung, fixed to a density that corresponds to the inhalation stage of the respiratory cycle[111,112]. As there is a great variation in lung density depending on the age and respiratory capacity of the individual, we selected a density on the low end of the scale, where the magnetic field would have the greatest influence.

The materials selected were chosen for investigation to provide context for the following chapters. Silicon was chosen due to its use in detector systems investigated in this thesis. Water was chosen as it is used as a phantom material for the silicon detectors, and also due to its common use in radiotherapy as a tissue equivalent material. Lung was chosen because it will later be used as a phantom material, and also because it demonstrates the extreme effect magnetic fields have in low density media.

Changes to dose distribution were assessed at the isodose line corresponding to 0.03% of D$_{max}$.

3.3 Results and Discussion

3.3.1 In-line orientation

Figure 3.1, Figure 3.2 and Figure 3.3 show the effect of inline magnetic fields on point spread dose arrays in silicon, water and lung relative to the 0 T case. Dose spread arrays in silicon show slight narrowing with increasing magnetic field strength (max. (0.5 ± 0.3) mm at 3 T) and negligible lengthening compared to the 0 T case (see Figure 3.1).

The influence of the magnetic field is more pronounced in water, with arrays exhibiting narrowing of up to (1.5 ± 0.3) mm and in-depth lengthening of (3.0 ± 0.3) mm at 3 T (see Figure 3.2). In water, a dose increase above the origin can be seen at 3 T. This is simply lengthening of the backscattered electron paths, similar to that of the forward-directed electrons.

Dose spread arrays in lung are most susceptible to perturbation. There is a maximum in-depth lengthening of (45.0 ± 0.3) mm and narrowing of (6.1 ± 0.3) mm at 3 T (see Figure 3.3). Again, there is dose increase above the point of origin, which extends to the phantom surface.

3.3.2 Perpendicular orientation

The effect of perpendicularly oriented magnetic fields on silicon, water and lung point spread dose arrays is shown in Figure 3.4, Figure 3.5 and Figure 3.6. Silicon arrays show a clear shift

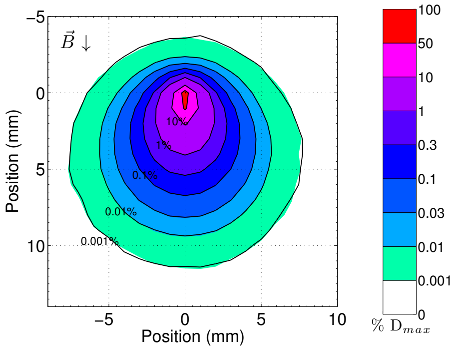

(a)$B_{\parallel}$ = 0.5T, silicon.

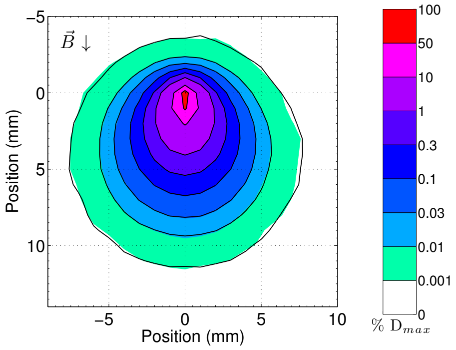

(c)$B_{\parallel}$ = 1T, silicon.

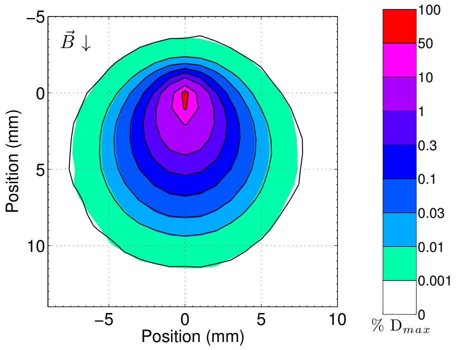

(e)$B_{\parallel}$ = 1.5T, silicon.

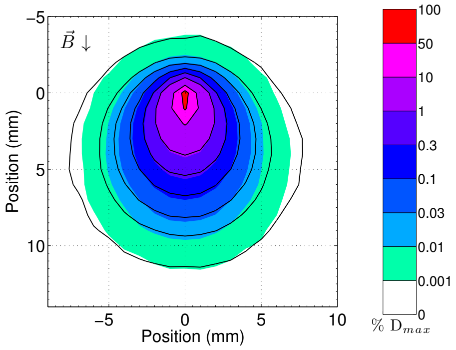

(g)$B_{\parallel}$ = 3T, silicon.

Figure 3.1: Point spread dose arrays in silicon in an *inline* magnetic-field-to-photon-beam orientation, for field strengths 0.5 T, 1 T , 1.5 T and 3 T. Distributions are presented in colour as a percentage of maximum dose, scaled logarithmically. The black isodose lines represent the case with no field applied.

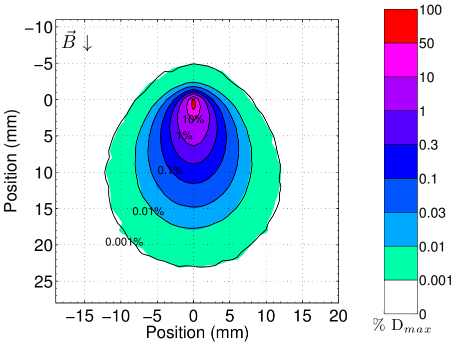

(a)$B_{\|}$ = 0.5T, water.

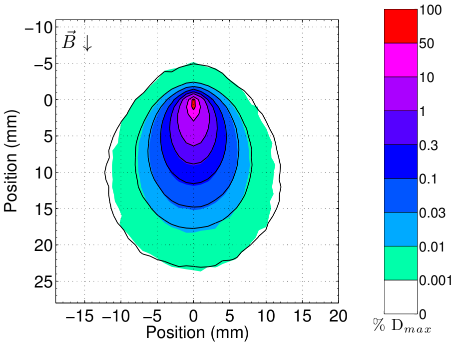

(c)$B_{\|}$ = 1T, water.

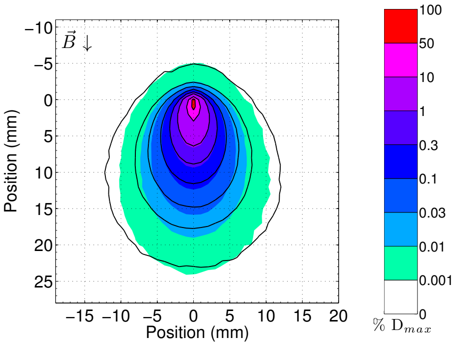

(e)$B_{\|}$ = 1.5T, water.

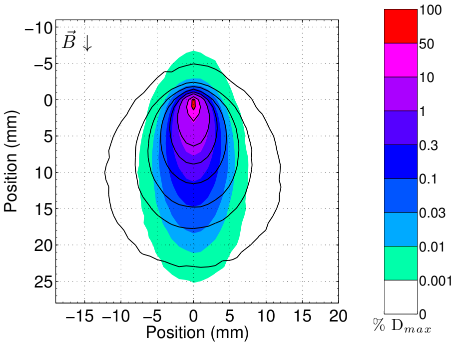

(g)$B_{\|}$ = 3T, water.

Figure 3.2: Point spread dose arrays in water in an *inline* magnetic-field-to-photon-beam orientation, for field strengths 0.5 T, 1 T , 1.5 T and 3 T. Distributions are presented in colour as a percentage of maximum dose, scaled logarithmically. The black isodose lines represent the case with no field applied.

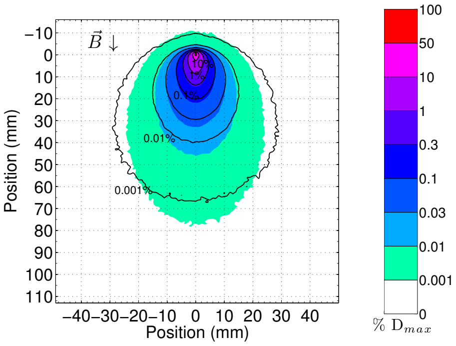

(a)$B_{||}$ = 0.5T, lung.

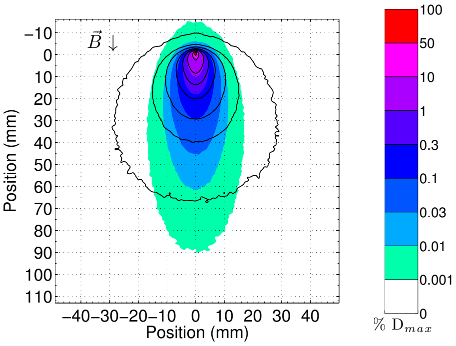

(c)$B_{||}$ = 1T, lung.

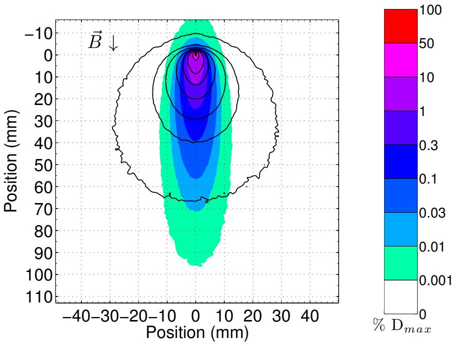

(e)$B_{||}$ = 1.5T, lung.

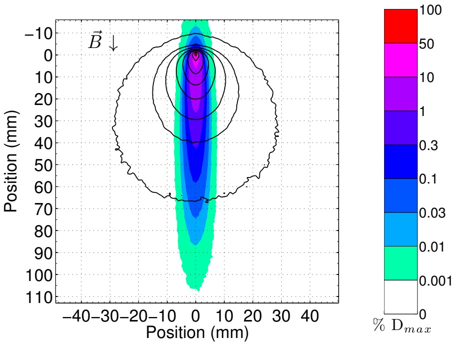

(g)$B_{||}$ = 3T, lung.

Figure 3.3: Point spread dose arrays in lung in an *inline* magnetic-field-to-photon-beam orientation, for field strengths 0.5 T, 1 T , 1.5 T and 3 T. Distributions are presented in colour as a percentage of maximum dose, scaled logarithmically. The black isodose lines represent the case with no field applied.

in dose (relative to the B=0 case) as the field strength increases, with a maximum in-depth shortening of (1.8 ± 0.3) mm and lateral shift of (1.8 ± 0.3) mm for the 3 T case (see Figure 3.4). However, when comparing the dose shift to that experienced in water, this change is minimal.

Water arrays show a maximum in-depth shortening (9.5 ± 0.3) mm at 3 T and a maximum lateral shift of (4.8 ± 0.3) mm at 1.5 T (see Figure 3.5). The results for water are in agreement with those presented by Raaijmakers et al[31], who also quoted a decrease in in-depth penetration as the field strength increased from 0 to 3 T and a maximum lateral displacement at 1.5 T.

In lung, a maximum lateral shift of (10.5 ± 0.3) mm is seen at 0.5 T, and in-depth shortening of (26.0 ± 0.3) mm at 3 T (see Figure 3.6). The maximum lateral shift occurring at the lowest field strength can be attributed to the radius of curved paths (see equation 2.2) being heavily influenced in the low density medium. At higher field strengths, the radius of curvature is much smaller, resulting in a smaller surface area of the kernel and less lateral displacement. This is also seen, although to a lesser extent, in water.

These results confirm that the dose spread arrays are less affected by the presence of a magnetic field in silicon than in water or lung (note difference in x- and y-axis scale for the two materials in the figures) as a consequence of its higher density (2.33 g/cm^3). In the lower-density materials, the helical trajectory of electrons is more achievable due to a decreased probability of scattering events per unit length, which noticeably alters the overall shape of dose spread arrays at each field strength.

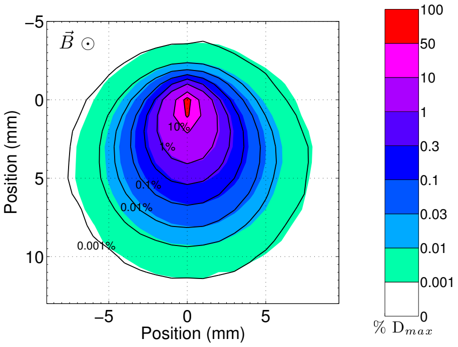

(a)B$_\perp$ = 0.5T, silicon.

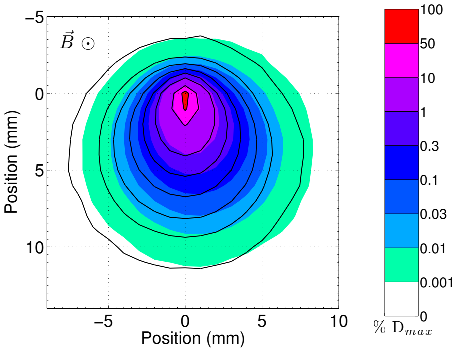

(c)B$_\perp$ = 1T, silicon.

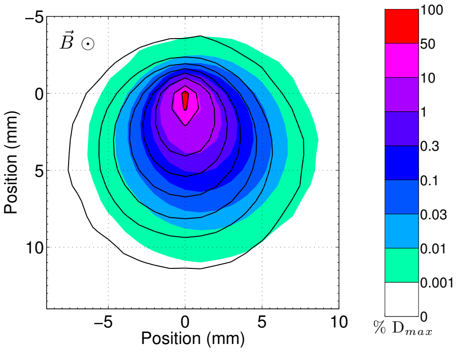

(e)B$_\perp$ = 1.5T, silicon.

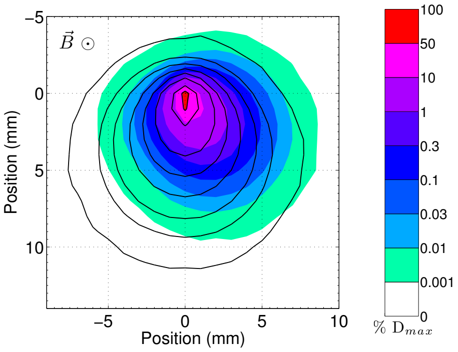

(g)B$_\perp$ = 3T, silicon.

Figure 3.4: Point spread dose arrays in silicon in a *perpendicular* magnetic-field-to-photon-beam orientation, for field strengths 0.5 T, 1 T , 1.5 T and 3 T. Distributions are presented in colour as a percentage of maximum dose, scaled logarithmically. The black isodose lines represent the case with no field applied.

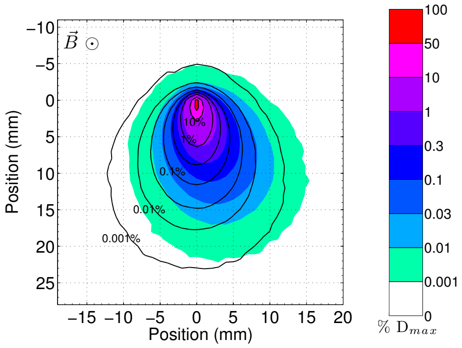

(a)$B_\perp$ = 0.5T, water.

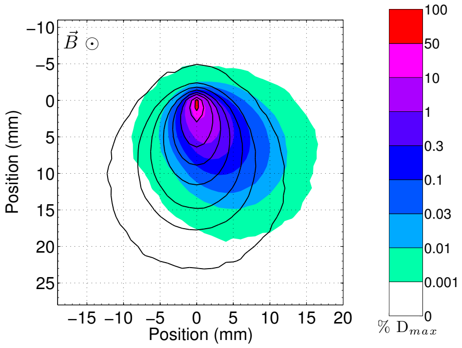

(c)$B_\perp$ = 1T, water.

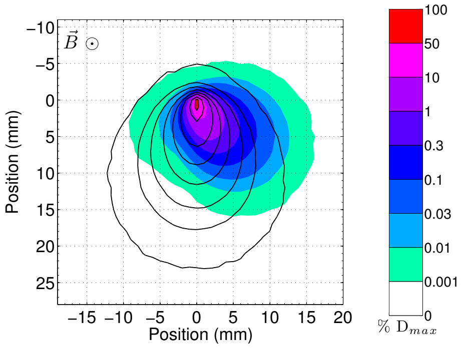

(e)$B_\perp$ = 1.5T, water.

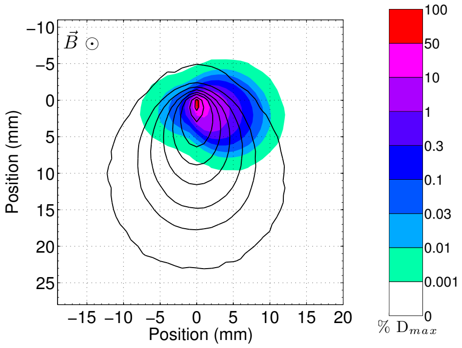

(g)$B_\perp$ = 3T, water.

Figure 3.5: Point spread dose arrays in water in a *perpendicular* magnetic-field-to-photon-beam orientation, for field strengths 0.5 T, 1 T , 1.5 T and 3 T. Distributions are presented in colour as a percentage of maximum dose, scaled logarithmically. The black isodose lines represent the case with no field applied.

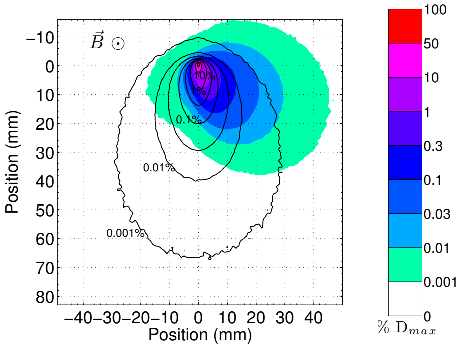

(a)$B_\perp$ = 0.5T, lung.

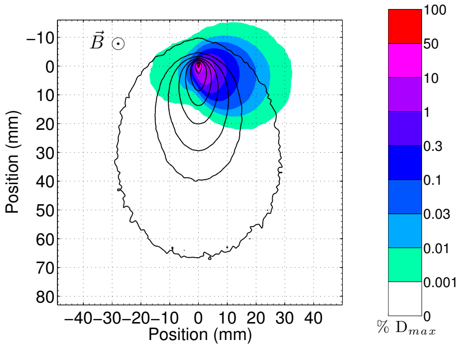

(c)$B_\perp$ = 1T, lung.

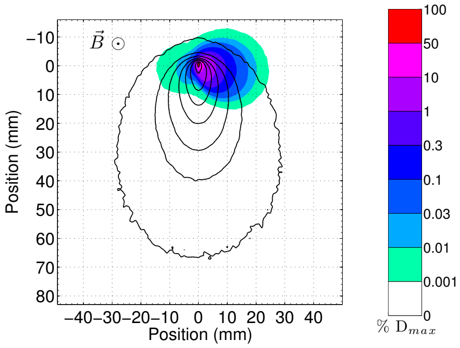

(e)$B_\perp$ = 1.5T, lung.

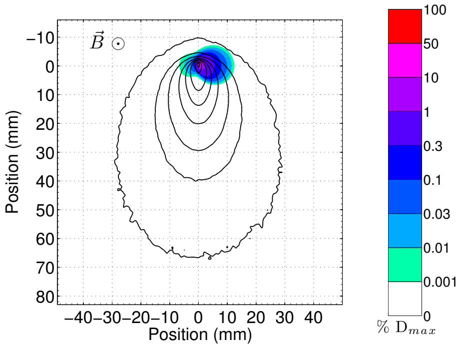

(g)$B_\perp$ = 3T, lung.

Figure 3.6: Point spread dose arrays in lung in a *perpendicular* magnetic-field-to-photon-beam orientation, for field strengths 0.5 T, 1 T , 1.5 T and 3 T. Distributions are presented in colour as a percentage of maximum dose, scaled logarithmically. The black isodose lines represent the case with no field applied.

3.4 Conclusion

The results presented in this chapter show the extent of distortion of deposited dose in magnetic fields in media of different density. When comparing the three media studied, lung (lowest density) was the most severely affected by the presence of a uniform magnetic field, followed by water, then silicon (highest density). The impact of magnetic field strength was also demonstrated. High magnetic field strengths of the perpendicular orientation resulted in a smaller surface area for the kernel. This can be attributed to a decreasing radius of curvature as the magnetic field strength increases. This means that particles have a smaller displacement from their point of origin, and thus a smaller overall surface area for the kernel. This is particularly true for secondary electrons produced in lung, where fuller circular trajectories are more achievable compared to in higher density media such as silicon. For the inline orientation, extreme focusing of dose kernels due to restriction of lateral scatter was observed, increasing in both the forward-projected and backscattered directions as field strength increased.

These results provide context for the data presented in the following chapters by demonstrating, on a fundamental level, changes to MV photon dose distributions as a function of magnetic field strength and media density. The results for silicon, presented in context with those to water, are helpful when considering the use of solid state detectors as water-equivalent detectors in magnetic fields. Further to this, in later chapters silicon detectors will be investigated in both water and lung phantoms.

It is important to note that conclusions as to the dose response of silicon dosimeters relative to water dose cannot be drawn from these point spread arrays alone. These simulations imply a solid three-dimensional silicon lattice, whereas the silicon array dosimeters either consist of small single diode or a thin monolithic silicon layer. Their purpose is to provide a visual aid in comprehending the differences in dose deposition ranges of electrons in the two materials. The silicon array detectors considered in this thesis have differing geometries, the homogeneity and orientation of which will impact on the silicon response. As such, the behaviour of dose depositing secondary electrons at boundaries between materials within the detector will be considered moving forward with the following simulations in chapters 4 and 5.

Chapter 4

Monte Carlo simulation of the dose response of a novel 2D silicon diode array for use in hybrid MRI-linac systems

The results presented in this chapter have been published in the journal Medical Physics:

M Gargett, B Oborn, P Metcalfe and A Rosenfeld, Monte Carlo simulation of the dose response of a novel 2D silicon diode array for use in hybrid MRI-LINAC systems, *Medical Physics*, vol. 42, no. 2, pp. 856-865, 2015.

4.1 Overview

Solid state arrays are yet to be studied for MRI-linac applications. This chapter investigates a novel 2D silicon diode array, named MagicPlate-121 (Magic Plate), for both single point calibration and 2D positional performance, the latter being a key element of modern radiotherapy techniques. The array consists of 121 small (1.5 x 1.5 x 0.38 mm^3) silicon diodes embedded in a kapton substrate. This design has potential advantage by minimising directional changes in secondary electron trajectories, which are known to occur at high-low density interfaces when magnetic fields are present[32]. Detector responses have proven to be affected when such interfaces exist around the detection volume, in particular for ionisation chambers - the current gold standard in external beam dosimetry. The Magic Plate's geometry has a relatively minimal change in density around the small detection volumes (density of kapton and silicon is 1.42 g/cm^3 and 2.33 g/cm^3 respectively) making it a dosimeter of interest for MRI-Linac applications. The radiation response of the epi-diodes has been characterised previously for use in external beam radiotherapy quality assurance (QA), and its design has proven to be minimally perturbative[65]. The results presented in this chapter were obtained via Monte Carlo simulation using the GEANT4 toolkit.

4.2 Materials and Methods

4.2.1 2D silicon diode array

Figure 4.1 shows a schematic diagram of the simulation geometry. The geometry included a homogeneous water phantom (30 x 30 x 30 cm^3) with the array placed at D$_{max}$, 1.5 cm below the surface (see Figure 4.1 (a)). The 11 x 11 silicon diode array covers a 10 x 10 cm^2 area with uniform, 1 cm pitch. The array geometry modelled accurately reflects the true physical geometries and material composition of the dosimeter. Each silicon diode (dimensions 1.5 x 1.5 x 0.38 mm^3) was placed in a kapton volume (thickness 650 μm) such that the sides of the diodes were surrounded by the substrate. The geometry also included a small air gap present at the base of each silicon volume (thickness 270 μm). Dose was scored in the active region, an 800 x 800 x 50 μm^3 volume centred on the top surface of each diode (see Figure 4.1 (c)). An identical detector array volume composed completely of water was simulated in parallel, to act as the reference dose.

4.2.2 Monte Carlo simulation parameters

The Monte Carlo simulation toolkit, GEANT4 version 9.6.p02 was used. The particle source for all simulations came from a 6 MV photon beam model for a Varian 2100C linear accelerator[45], and were read in using phase space files of the spectrum at the level of the MLCs. Note that these phase space files were not generated in the presence of a magnetic field and thus an assumption is made that the photon beam spectrum is not influenced by possible magnetic fringe fields. This assumption should not affect the validity of results, given that the electron gun can be shielded[23] or re-designed[25] so that the capture efficiency is not affected.

Details of the simulation geometry is provided in section 4.2.1; for a schematic see Figure 4.1.

Particle interaction processes modelled include photoelectric effect, compton scattering and gamma conversion for photons; multiple scattering, ionisation, bremsstrahlung and annihilation for electrons and positrons. Particle range cuts for gammas, electrons and positrons were set at a value of 1 mm.

Care was taken in choosing an appropriate step limit for the scoring volume and surrounding material, not exceeding one third of the smallest dimension of respective volumes. The water phantom had a step limit of 0.2 mm, which was reduced to 0.1 mm between diodes, while the silicon diodes had a step limit of 0.01 mm.

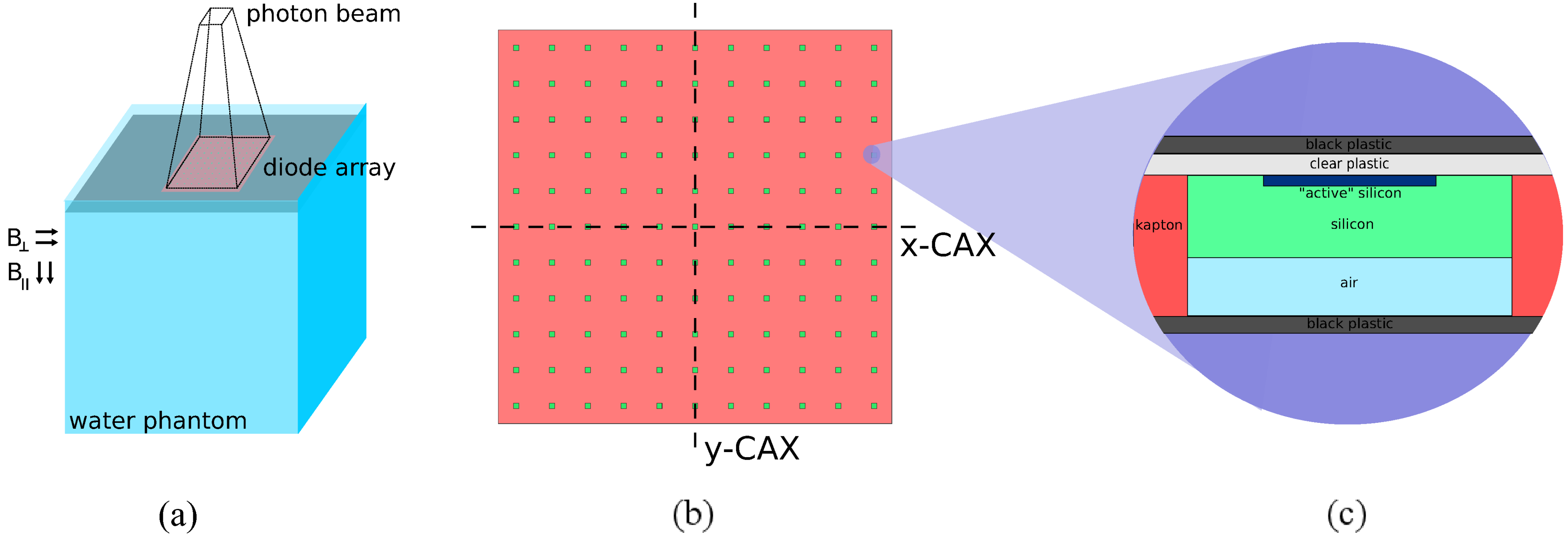

Figure 4.1: Part (a) is a diagram of simulation geometry, with the diode array positioned 1.5 cm below the surface of a 30 x 30 x 30 cm^3 water phantom. The array, pictured in part (b), consists of 121 silicon diodes (11 x 11 placement with 1 cm pitch) in a kapton substrate, with a maximum detectable area of 10 x 10 cm^2. Part (c) is the cross section of a single diode, with dose scored in the “active” region.

GEANT4 simulations that include a magnetic field have 3 primary parameters that can be adjusted to modify the chord selection for curved path approximations: miss distance, delta intersection and delta one step. These parameters were set at 0.025 mm, 1 μm and 10 μm respectively; the same as used for simulations shown in chapter 3, to maintain realistic computation times while still achieving acceptable accuracy. These parameters are described, along with justification of the chosen magnitudes, in chapter 3.

The number of simulations run was chosen so as to reduce standard deviation to an acceptable level (±1%). The standard deviation was calculated from ten parallel groups of jobs with unique seed numbers. The number of primary histories was 1.3 x 10^{10} for phase space files. In most cases histories were recycled 19 times to improve the statistics achieved for a given computation time, considering the small dose scoring volumes involved. The largest jobs ran for an estimated 96 CPUh.

4.2.3 Dose response simulations

The diode array was simulated at 1 T for both the inline and perpendicular magnetic-field-to-photon-beam orientations in order to assess the dose response to jaw-defined photon fields of size 2 x 2 cm^2, 4 x 4 cm^2 and 10 x 10 cm^2. Magnetic field strengths of 1.5 T and 3 T were also investigated for the 4 x 4 cm^2 field size. An assortment of MLC defined segments were then simulated to further assess changes in dose response of the diode array due to 1 T magnetic fields. Leaf arrangements were specifically chosen to fall in a variety of positions in relation to the silicon diodes, in order to rigorously investigate at what distance from the beam edge the dosimeters' response is affected. MLC field shapes ranged in size, from as small as 1 mm between opposing leaves, up to larger areas such as a circle 6 cm in diameter. See Figure 4.6 and Figure 4.7 for detailed field shape diagrams.

To assess in-field dose gradients typical of clinical plans, an IMRT beam consisting of 12 segments was simulated at 1 T for the perpendicular orientation. The chosen plan was a small field case (brain), considering the maximum detectable area of the array is 10 x 10 cm^2. Individual segment dose was weighted according to the corresponding number of monitor units (MUs).

4.3 Results and Discussion

4.3.1 Jaw defined fields

In-line magnetic field orientation

Figure 4.2 parts (a) - (c) show a cross section of the water phantom for the three field sizes simulated, for an inline magnetic-field-to-photon-beam orientation at 1 T. There is an appreciable increase in dose at the phantom surface for the 10 x 10 cm^2 field size, due to a focusing of electron contamination towards the air-water interface by the magnetic field in this orientation. The distribution of dose remains symmetric (about the vertical axis) through the entire depth of the water phantom. Figure 4.2 parts (d)-(f) indicate the photon field size in relation to detector position (black dots), at depth of 1.5 cm.

The dose profiles in Figure 4.3 (parts (g)-(i)) represent the dose to diodes along the central x- and y- axes of the array (see Figure 4.1(b) for profile outlines) in the presence of a 1 T inline magnetic field. The profiles are both flat (in field) and symmetric. This is to be expected of the inline orientation when considering the direction of the Lorentz force is parallel with the photon beam. Figure 4.3 parts (j)-(l) show pixel-by-pixel percentage difference maps of the entire silicon array compared to water, after normalising to the central pixel (central 9 for 10 x 10 cm^2 field size). The silicon and water doses are proportional to one another, demonstrated by the uniformity of the percentage difference maps (variations are due to the level of system noise inherent in Monte Carlo data). The dose response of the silicon array maintains this uniformity at the higher field strengths tested, 1.5 T and 3 T (for a 4 x 4 cm^2 field size, not shown).

Perpendicular magnetic field orientation

The effect of a 1 T perpendicularly oriented magnetic field on the depth dose in the water phantom can be seen in Figure 4.4 parts (a)-(c). The distribution of dose is not symmetric about the vertical axis, but skewed from left to right according to the direction of the Lorentz force associated with the magnetic field. An increase in exit dose is appreciable for all field sizes, as a result of returning electrons at the water-air (high-low density) interface. Figure 4.4 parts (d)-(f) indicate the photon field size in relation to detector position (black dots).

Figure 4.5 parts (g)-(i) show dose profile plots for the perpendicular magnetic field orientation at 1 T. They are asymmetric at the beam edge, which can be attributed to the asymmetirc penumbra chartacteristic of perpendicularly aligned radiation beams and magnetic fields. This

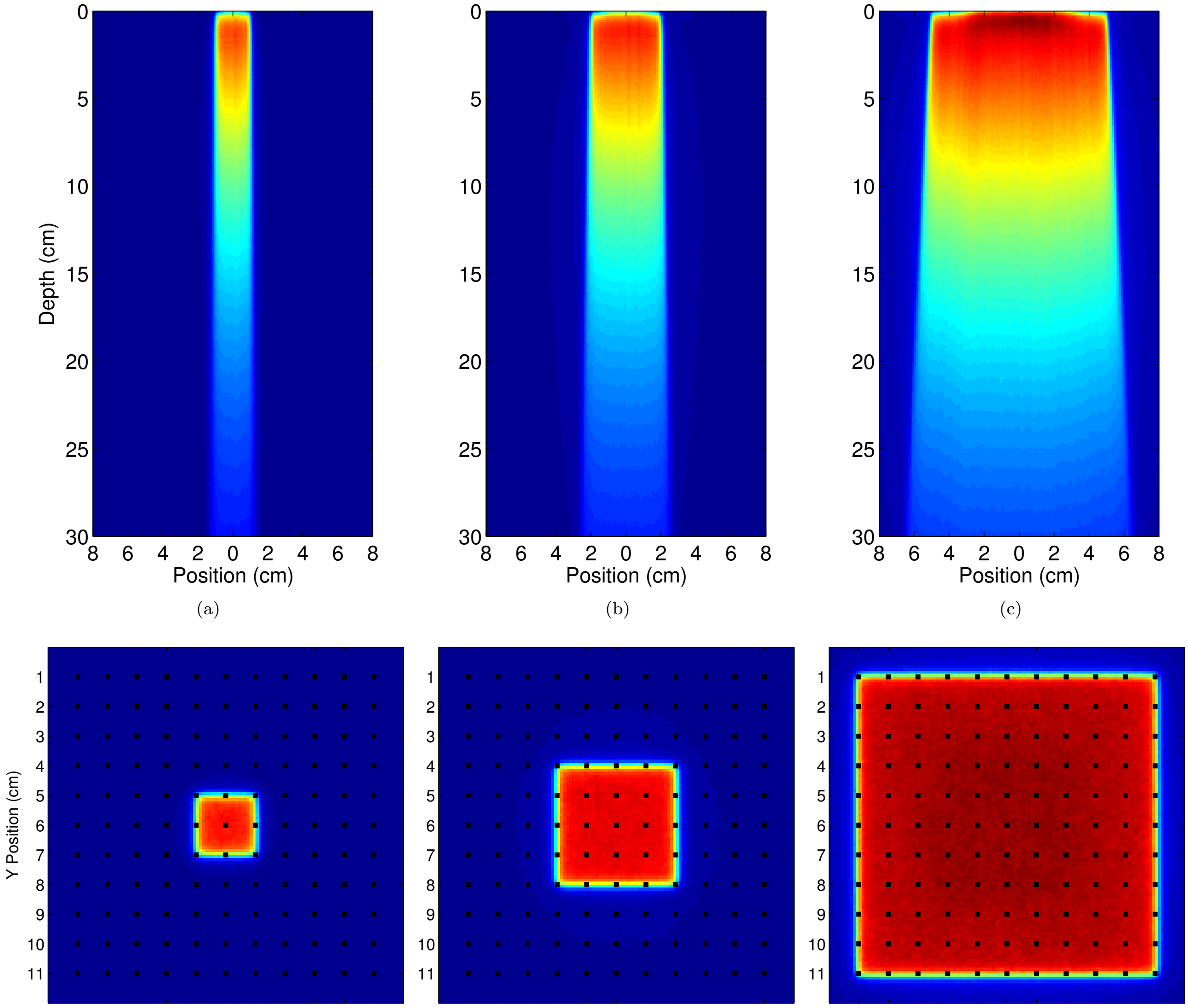

(a) (b) (c)

(d) (e) (f)

Figure 4.2: *In-line* magnetic field orientation, 1 T field strength. Water depth dose in a cross section of the phantom is shown in parts (a)-(c) for the three jaw-defined field sizes, 2 x 2 cm^2, 4 x 4 cm^2 and 10 x 10 cm^2. Water dose in the same plane as the detector array is shown in parts (d)-(f). For parts (a)-(f) the colour scale is such that red indicates high dose and blue indicates low (or zero) dose. View in conjunction with Figure 4.3.

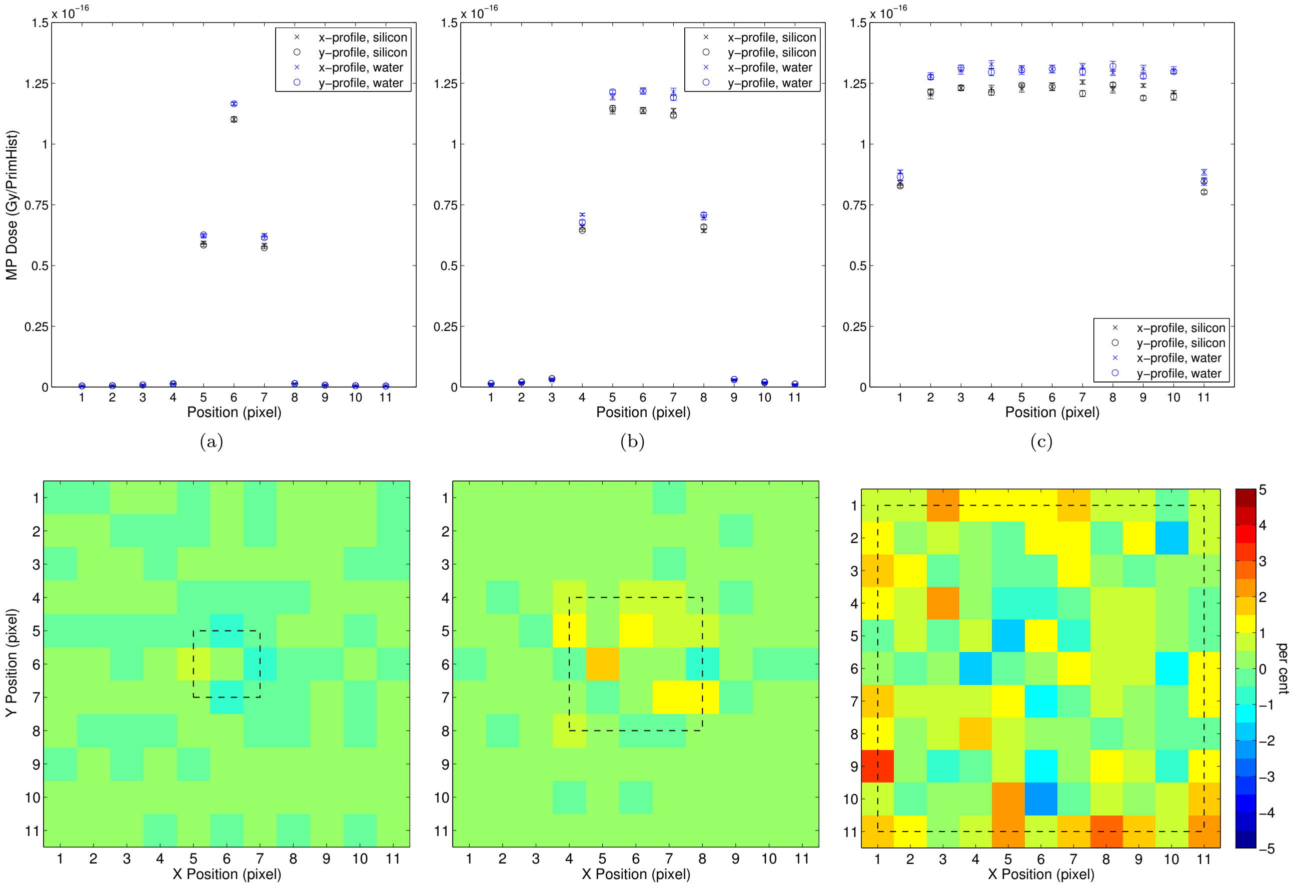

(a) (b) (c)

(d) (e) (f)

Figure 4.3: *In-line* magnetic field orientation, 1 T field strength. Parts (a)-(c) show dose profiles of silicon and water equivalent diodes along the central axes (see Figure 4.1 part (b)). Error bars indicate standard deviation. Parts (d)-(f) show dose difference images of silicon dose relative to water, scaled to respective central axis doses. Each pixel represents the response of the diode in the corresponding position of the 11 x 11 array. The locations of the photon field edge in relation to detector position are indicated by the dotted line. View in conjunction with Figure 4.2.

asymmetry decreases as field size increases and lateral electron equilibrium is achieved. While the central portion of the radiation field exhibits an equivalent level of uniformity as seen for the inline orientation, the edge detectors falling in the high dose gradient penumbral region indicate a shift in silicon dose relative to water dose (see Figure 4.5 parts (j)-(l)) for all field sizes investigated. Taking the 4 x 4 cm^2 field size as an example, an over-response in "-x" side pixels is seen, worst at 1.5 T. This mimics the trend of lateral dose shift in water point spread dose arrays. An under response relative to water is observed in the opposing penumbral region, and worsens for field strengths above 1 T, although there is little difference in results for 1.5 T and 3 T. The magnitude of over and under response is summarised in table Table 4.1.

To further investigate this trend, field sizes 4.2 x 4.2 cm^2, 4.12 x 4.12 cm^2, 3.88 x 3.88 cm^2 and 3.8 x 3.8 cm^2 were also simulated at 1 T. For the largest field size, a maximum over-response and minimum under-response was found ((5.2 ± 0.8) % and (-0.4 ± 0.8) % respectively). As field size decreased (and the corresponding beam penumbra moved gradually out of the line of detection of diodes), the over-response decreased and the under-response increased. At the smallest field size, the over-response diminished and the under-response was a maximum ((1.4 ± 0.8) % and (-4 ± 0.8) % respectively).

Table 4.1: Average edge-of-field over and under response observed for the perpendicular field orientation at various magnetic field strengths, as a percentage relative to water dose. The "-x" side refers to leftmost diode column exposed to beam, and "+x" refers to rightmost. Stated uncertainty is in terms of one standard deviation.

B strength (T)	Field size (cm^2)	"-x" side response (±0.8%)	"+x" side response (±0.8%)
1	2 x 2	3.0	-1.8
	4 x 4	3.3	-1.8
	10 x 10	4.3	-1.3
1.5	4 x 4	4.0	-3.2
3	4 x 4	3.0	-3.2

The perpendicular magnetic field orientation is mostly affecting the dose distribution to the penumbra, which can be explained by the relative contributions of low energy electrons to the spectrum in this region compared to in-field. Since low-energy electrons have a tighter radius of rotation around the magnetic field vector, dose enhancement occurs in regions with more low-energy contribution to fluence[113,114]. This applies to the "-x" side pixels, where low energy electrons enter the silicon diodes located in or near the penumbral region. Conversely, the low energy fluence is reduced in the opposing "+x" penumbral region. This leads to the over and under response observed for silicon dose, relative to water, at opposite sides of the array. This theory also explains the increase in over-response for the 10 x 10 cm^2 field size, as there is a relatively larger population of low energy electrons. These observations are in good agreement with the Bragg Gray cavity theory, which states that the ratio of silicon to water dose is dependent on the mass collisional stopping power ratio, which increases slightly with decreasing of electron energy.

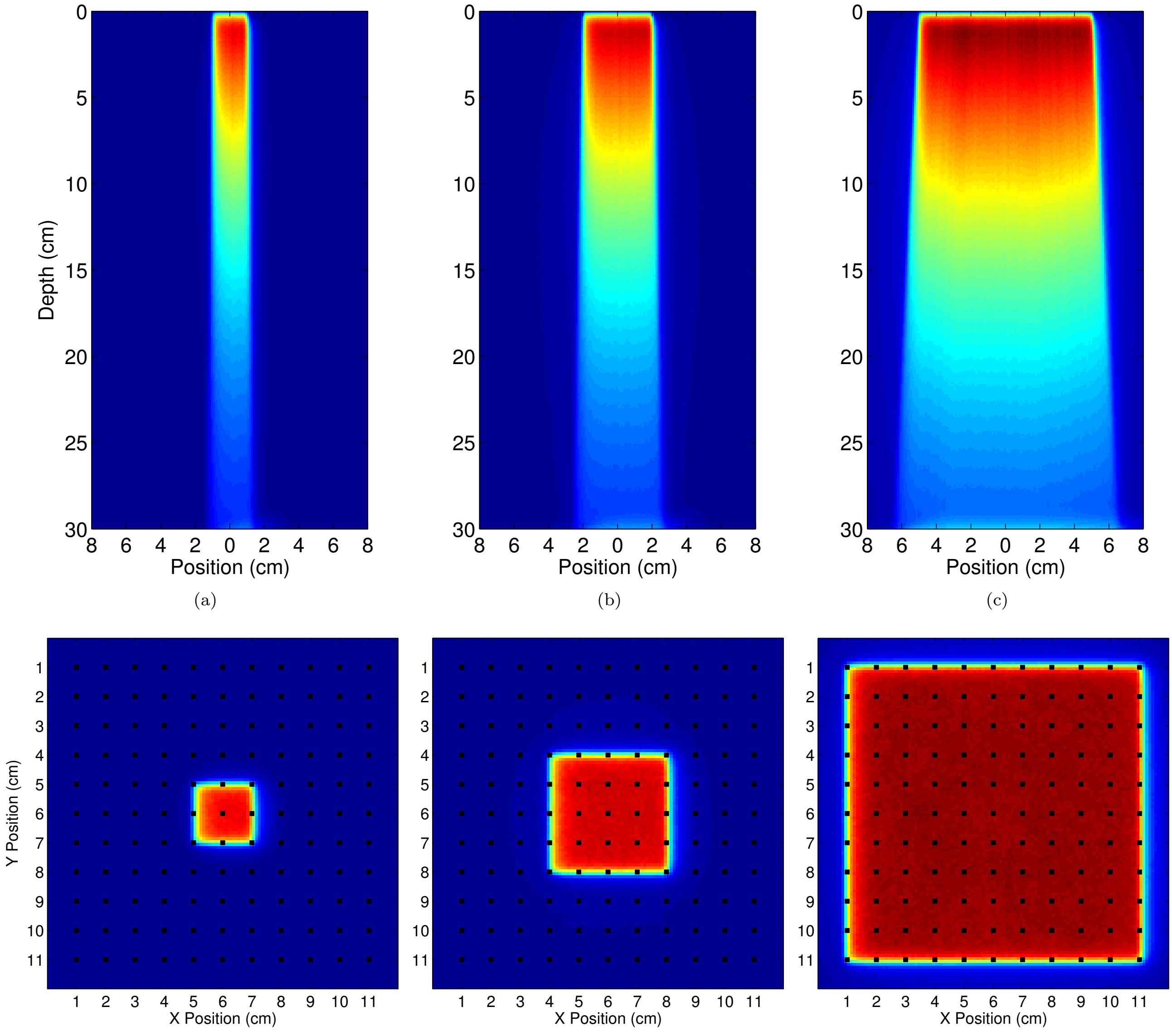

(a) (b) (c)

(d) (e) (f)

Figure 4.4: *Perpendicular* magnetic field orientation, 1 T field strength. Water depth dose in a cross section of the phantom is shown in parts (a)-(c) for the three jaw-defined field sizes, 2 x 2 cm^2, 4 x 4 cm^2 and 10 x 10 cm^2. Water dose in the same plane as the detector array is shown in parts (d)-(f). For parts (a)-(f) the colour scale is such that red indicates high dose and blue indicates low (or zero) dose. View in conjunction with Figure 4.5.

4.3.2 MLC defined fields

Figure 4.6 and Figure 4.7 display the percentage difference in the ratio of silicon to water dose of each diode of the array for the 10 MLC patterns studied, in a perpendicular magnetic field orientation at 1 T. The inline orientation was also investigated (not shown), with no appreciable

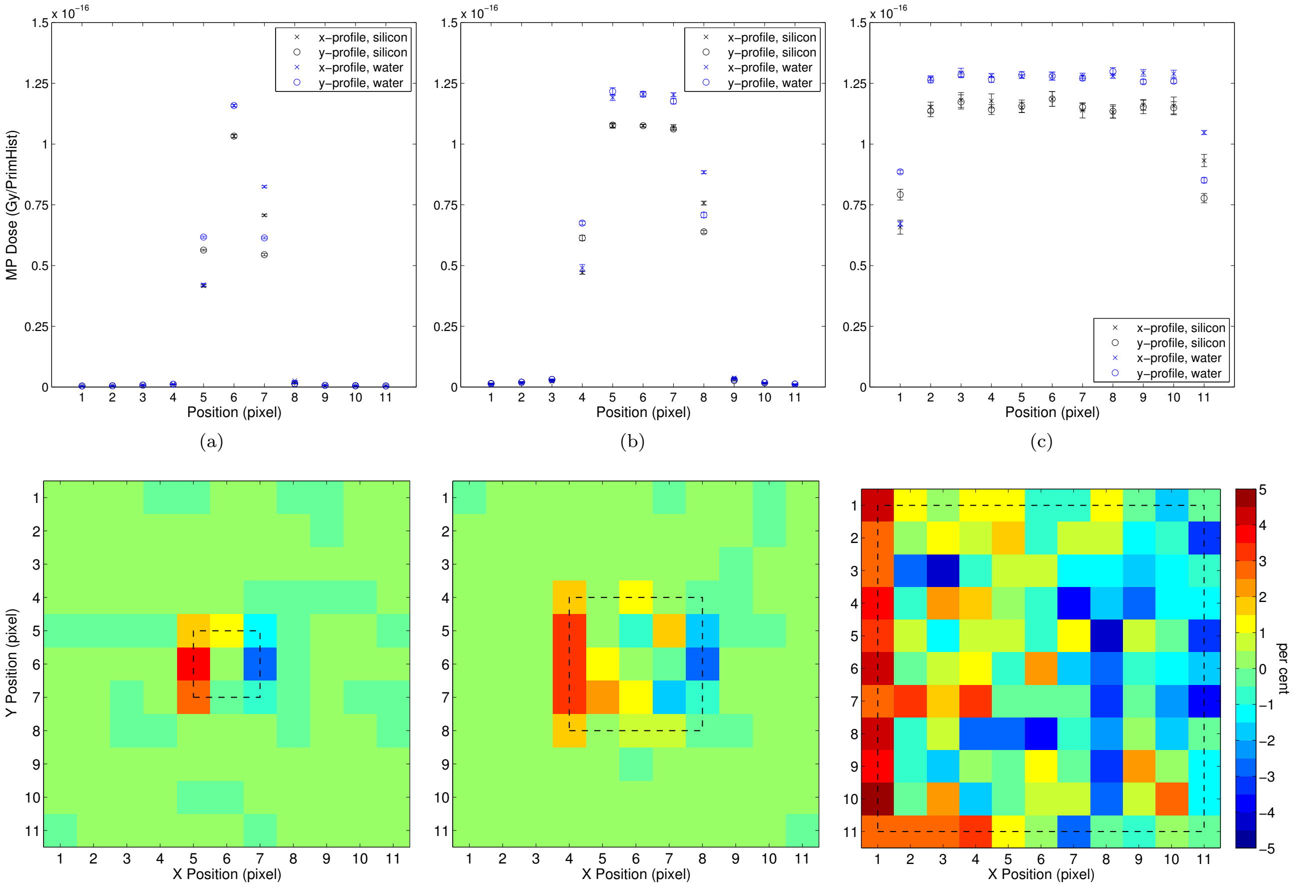

(a) (b) (c)

(d) (e) (f)

Figure 4.5: *Perpendicular* magnetic field orientation, 1 T field strength. Parts (a)-(c) show dose profiles of silicon and water equivalent diodes along the central axes (see Figure 4.1 part (b)). Error bars indicate standard deviation. Parts (d)-(f) show dose difference images of silicon dose relative to water, scaled to respective central axis doses. Each pixel represents the response of the diode in the corresponding position of the 11 x 11 array. The locations of the photon field edge in relation to detector position are indicated by the dotted line. View in conjunction with Figure 4.4.

difference in silicon and water doses at 1 T.

Similar to the case of jaw-defined fields in a perpendicular magnetic field orientation, it is the detectors that lie on or closest to the field edge that irregularly respond. At the “-x” side, diodes over-respond as the beam edge approaches the detector, but return to the baseline response once out of field. At the “+x” side, the worst under-response is seen in detectors just out of field (up to 9 mm from nearest leaf tip) and response becomes more regular as more of the detector is exposed to the open field. This is best shown in Figure 4.6 part (d), where MLC positions were chosen to gradually step across detectors. The field size also affects the dose response of diodes. Small fields of width 3 mm or less do not exhibit an over-response on the “-x” side, only an under-response at the “+x” side. This is expected to be due to the lack of particles that would otherwise magnify the over-reponse, as was seen for larger fields.

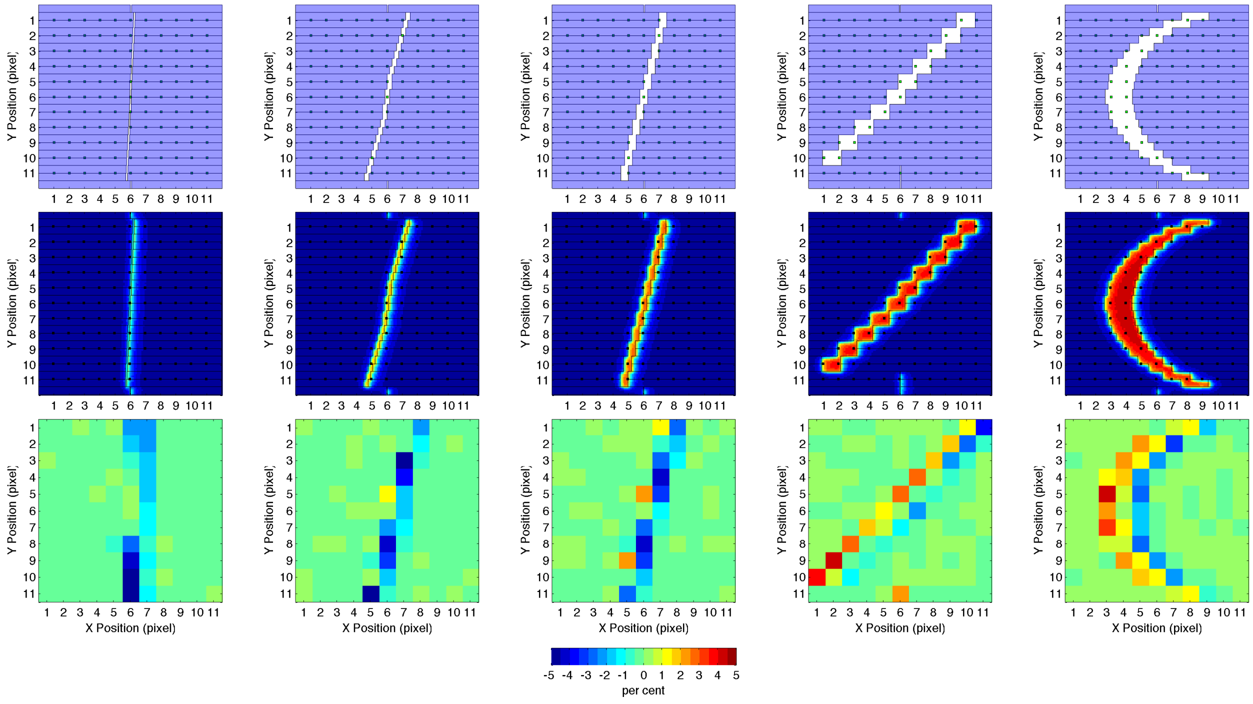

(a) (b) (c) (d) (e)

Figure 4.6: The dose response of the diode array for a variety of irregular field shapes at 1 T, in a perpendicular magnetic-field-to-photon-beam orientation. MLC segment shapes in relation to diode position are shown in the top row. The second row shows the water dose for each field shape in relation to diode position. The third row shows the corresponding pixel-by-pixel dose difference plots of silicon diodes relative to water, as a percentage of central axes dose. Parts (a)-(c) are thin diagonal fields with leaf separation of 1 mm, 3 mm and 5 mm respectively. Part (d) has 12.5 mm leaf separation, with the field stepping gradually across detectors. Part (e) is a thin, rounded-edge field.

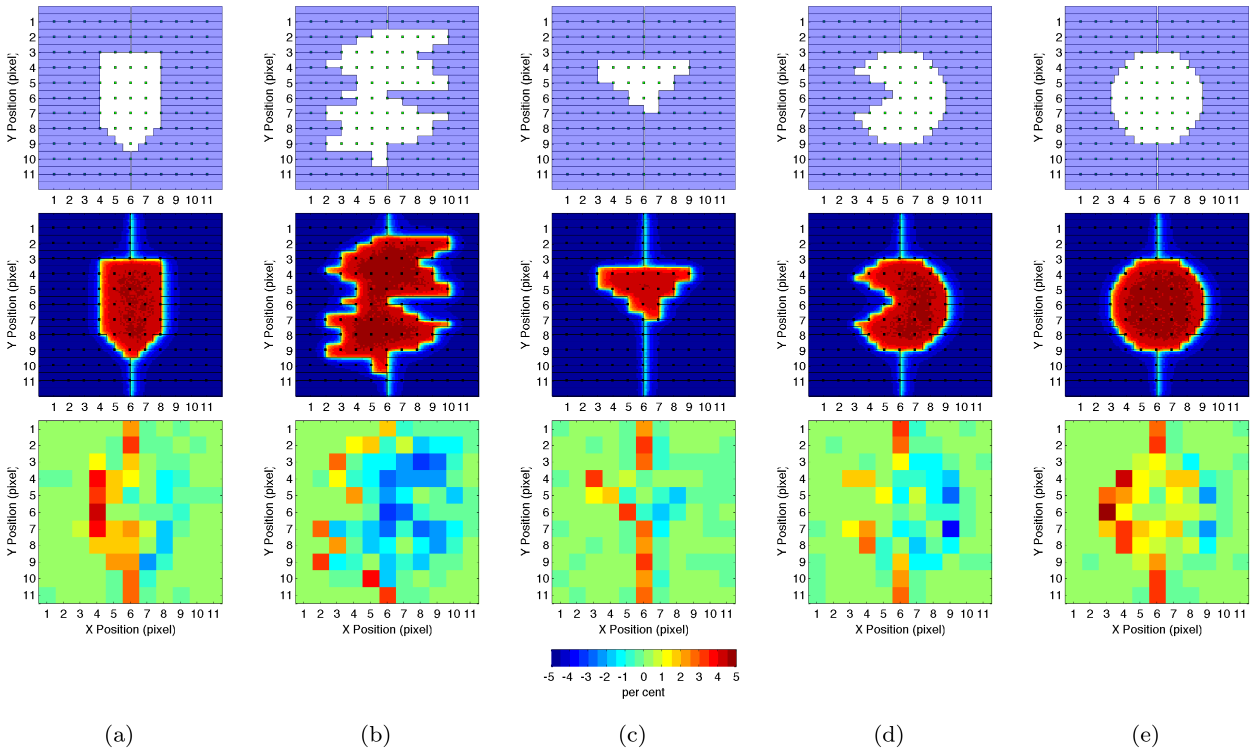

Figure 4.7: Dose response of the silicon diode array relative to water for a variety of larger MLC segments, in a 1 T perpendicular magnetic-field-to-photon-beam orientation.

4.3.3 IMRT segments

The single-segment jaw-defined and MLC-defined fields investigated thus far demonstrate a worst case scenario in terms of dose response in steep dose gradient regions at the edge of field. To assess whether the previously encountered over and under response of diodes is present for typical in-field dose gradients, a clinical IMRT beam composed of 12 segments was simulated (see Figure 4.8). Although this test case can not be taken as definitive for all scenarios, it does contain an appreciable amount of beam modulation with correspondingly steep dose gradients. There is no appreciable over or under response in-field (relative to water) above the level of system noise. The over-response of edge of field diodes remains appreciable, however the combination of multiple segments does not appear to compound the issue.

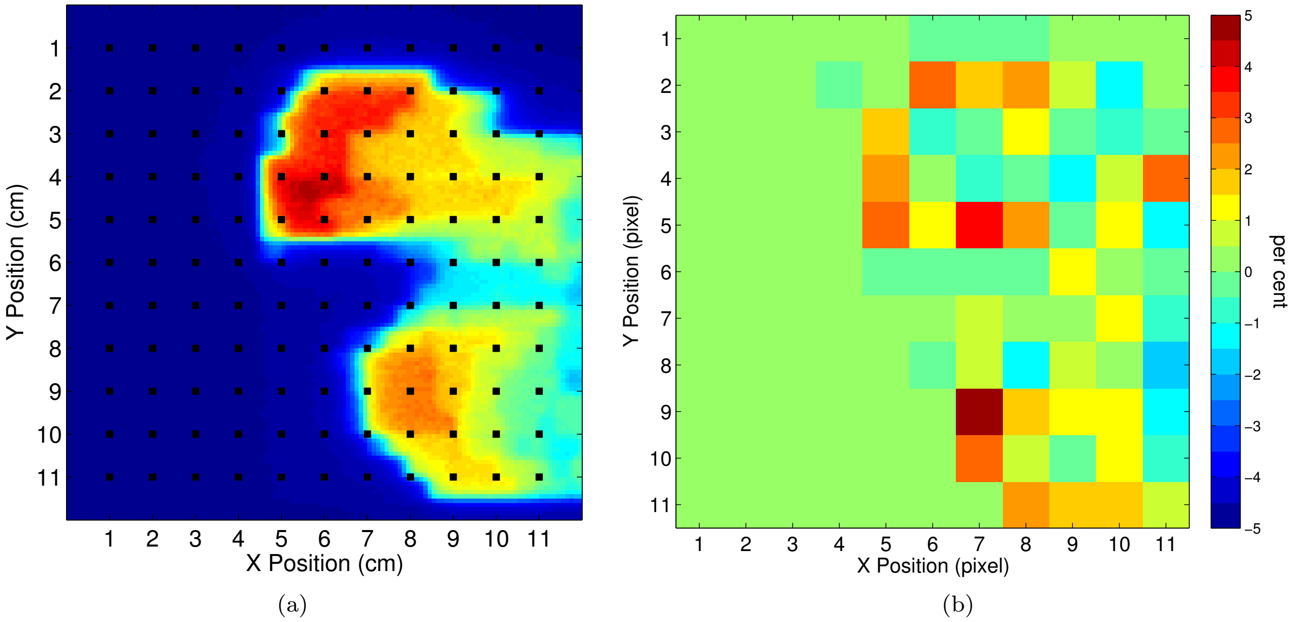

(a) (b)

Figure 4.8: Water dose (part (a), with diode positions indicated) and dose difference relative to water for each diode position (part (b)) for a 12 segment IMRT field in a 1 T, perpendicularly oriented magnetic field.

4.4 Conclusion

Monte Carlo simulations of a novel 2D diode array exposed to various magnetic field strengths have been performed. Results indicate that the dose to the silicon sensitive volume reflects the water dose when used in an inline magnetic field in the range 1 - 3 T. For the perpendicular orientation of the magnetic field, a shift in silicon dose relative to water was observed in the penumbral regions of single-segment fields. This shift was not evident at in-field dose gradients typical of a clinical IMRT plan. Single-segment dose measurements with the array may require corrections if detectors fall on or near the beam edge. The array is expected to be a valuable tool in MRIgRT dosimetry.

Chapter 5

Monte Carlo modeling of a novel high resolution 2D silicon diode array for small field dosimetry in an MRI-linac

The results presented in this chapter have been published in the journal Biomedical Physics and Engineering Express:

M Gargett, B Oborn, S J Alnaghy, T Causer, M Petasecca, A B Rosenfeld and P Metcalfe, A high resolution 2D array detector system for small-field MRI-LINAC applications, *Biomedical Physics & Engineering Express*, vol. 4, no. 3, 2018.

5.1 Overview

The superior image quality of MR imaging compared to current kV-photon based imaging systems, particularly in terms of soft tissue contrast, will be most beneficial for stereotactic ablative radiation therapy (SBRT), where high geometric precision of the delivery of ablative doses is paramount. As such, it is expected that SBRT will form a majority part of the workload at MRI-linac facilities. Many SBRT applications involve small fields.

If MRI-linac systems are to employ small-field treatments, it is imperative there are dosimeters available for dosimetry that are not only magnetic-field compatible but are small-field appropriate, given the challenges already faced in small field dosimetry stemming from source occlusion, lateral electron disequilibrium and detector perturbation effects[115–118]. Several dosimeter types have been characterised with regard to their suitability as small field dosimeters, not all of which are appropriate, for example ionization chambers of (relatively) large volume[119–121].

In this chapter, we investigate re-appropriating a novel high resolution silicon array dosimeter originally developed for small-field dosimetry, the MagicPlate-512 (M512), for magnetic field applications. This dosimeter differs in design and spatial resolution to the MagicPlate-121 array previously investigated for MRI-linac applications in chapter 4. The MagicPlate-121 is an array of silicon diodes arranged with uniform 10 mm pitch in a kapton substrate. The M512 is a monolithic silicon dosimeter with 512 detection pixels (dimension 0.5 mm x 0.5 mm) in a high density arrangement of 2 mm pitch, which is of a higher resolution than commercial diode/chamber array dosimeters currently available. The M512 has been commissioned for small field dosimetry applications down to field sizes of 0.5 cm dimension by Aldosari et al[70,71]. Key results of Monte Carlo simulations addressing how magnetic fields affect small field dose distributions and characteristics (FWHM and 80% - 20% penumbral width) in a homogeneous water phantom are first presented. This is then followed by detailed simulations of the dose deposition within the dosimeter geometry, which included dosimeter density parameters, from which results are drawn as to the perceived water-equivalence of the dosimeter.

5.2 Materials and Methods

5.2.1 The dosimeter: 2D silicon diode array

The M512 consists of a thin monolithic silicon wafer (52 x 52 x 0.47 mm^3) with 512 ion-implanted diodes (0.5 x 0.5 mm^2). Diodes are spaced evenly with 2 mm pitch, covering a maximum detection area 46 mm wide. A small air-gap exists above the silicon chip to counteract dose enhancement that occurs for small field sizes due to different scattering and secondary electron spectra in silicon compared to water[122,123]. The air gap size has been optimised to a water equivalent response at zero magnetic field conditions[71]. Full details on literature relating to the dosimeter is contained in section 2.4.2.

5.2.2 Monte Carlo simulations

GEANT4 Monte Carlo toolkit, version 9.6.p02, was used. Figure 5.1 shows a depth-wise view of the dosimeter as it was modelled. The dosimeter was positioned in a 30 x 30 x 30 cm^3 water phantom, such that the base of the array was at 1.5 cm depth. The monolithic silicon wafer is a bulk silicon volume containing an array of sub-volumes positioned to replicate pixels. The dimension of each sub-volume (0.5 x 0.5 x 0.1 mm^3) approximates that of the sensitive volume of each pixel. Energy in this volume was scored and used to calculate the dose to medium per primary history.

To closely approximate the true geometry of the dosimeter, the bulk silicon volume was placed on top of a thin (0.5 mm) volume representing a printed circuit board, the material of which has the composition of FR4 grade laminate. This is contained by two PMMA volumes of 5 mm thickness, top and bottom. The top layer has a recess surrounding the silicon volume, which introduces an air gap around the dosimeter (2 mm directly above) which is reflective of the true dosimeter casing.

For each test case, simulations were also run for a water-only geometry (the 30 x 30 x 30 cm^3 phantom, without dosimeter), to assess magnetic field effects on small photon fields in a homogeneous medium. It provides a frame of reference to separate magnetic field effects from dosimeter perturbations and other possible geometry-related effects (e.g. ERE in an air-gap). A higher resolution dose grid (voxel size 0.1 x 0.1 x 0.01 mm^3) was used to produce dose profiles in the pure-water medium, covering a region equivalent to the depth of the active volumes of the silicon pixels.

The maximum allowed step lengths in the active volume was set to 2 μm, to ensure accurate dose deposition calculation. In the presence of a magnetic field there are further parameters that can be optimised to improve the simulation of radiation transport, including miss distance, delta intersection and delta one step. These parameters are used to modify the chords used to approximate curved path trajectories of charged particles. Selection of appropriate values for these parameters allows the user to optimise computation time while maintaining a suitable level of accuracy. The values set for miss distance, delta intersection and delta one step were 25 μm, 1 μm and 10 μm respectively. These values were chosen based on previous investigations of appropriate parameterisations for the magnetic field strengths used; see chapters 3 and 4.

Magnetic field effects were investigated for a series of small divergent photon beams of size 0.5 x 0.5 cm^2, 1 x 1 cm^2, 2 x 2 cm^2 and 3 x 3 cm^2 and uniform magnetic fields of strength 1 T and 3 T. A 1 T magnetic field was chosen to reflect the strength of the Australian MRI-linac research facility. A 3 T field strength was chosen in order to investigate the dosimetric effect of higher field strengths, that could potentially be used in future systems to provide higher image quality. The particle source was in the form of phase space files from a 6MV photon beam model for a Varian 2100C linear accelerator[45], and corresponds to the beam spectrum used for experimental measurements reported in chapter 6.

Particles were recycled 780 times for all runs, to achieve an approximate density of 2.5 x 10^8 particles per cm^2. This reduced the standard deviation of energy deposition in the central diode pixel to $\leq$ 0.5% (out of 100 runs, each with unique seed numbers).

The MATLAB® (MathWorks) curve fitting toolbox was used to fit a shape-preserving interpolant to beam profiles for full width at half maximum (FWHM) and penumbral width (80% - 20%) calculations. Results are reported to the nearest 100 μm.

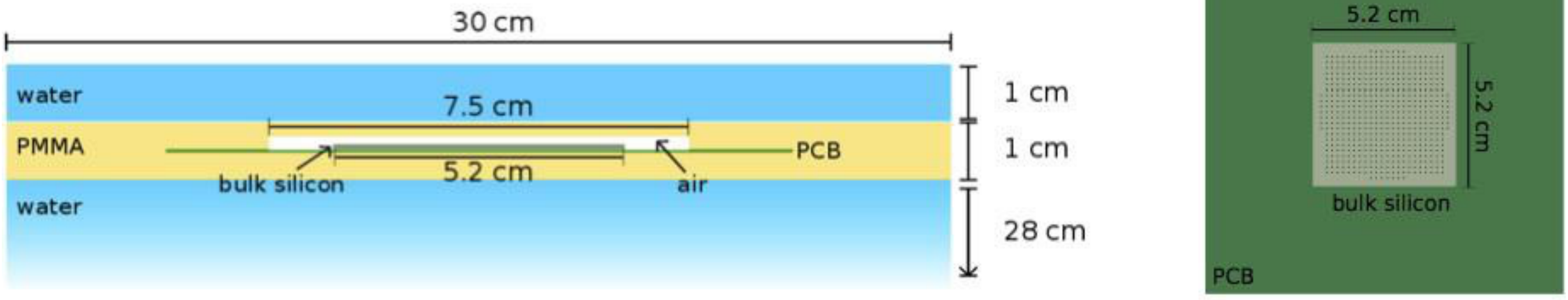

(a) (b)

Figure 5.1: Part (a) is a side-on view of simulation geometry showing the dosimeter, surrounded by PMMA casing, in a water phantom. Part (b) shows sub-volume arrangement in bulk silicon.

5.3 Results and Discussion

5.3.1 Impact of magnetic fields on small photon fields in water

Figure 5.2, Figure 5.3, Figure 5.6 and Figure 5.6 parts (a) - (b) present square photon beam (0.5 x 0.5 cm^2, 1 x 1 cm^2, 2 x 2 cm^2, 3 x 3 cm^2) profiles in a 30 x 30 x 30 cm^3 water phantom, at 1.5 cm depth, for inline and perpendicular magnetic field orientations respectively.

In-line magnetic field orientation

Table 5.1 contains FWHM and penumbral width results for photon fields in the inline magnetic field orientation. The presence of an inline magnetic field does not significantly affect the FWHM of beam profiles for all field sizes and magnetic field strengths investigated, with the change from 0 T to 3 T being less than 0.1 mm. There is a very slight penumbral narrowing at 3 T (approx. 0.2 mm).

There is an increase in dose at the central axis (CAX) in the presence of inline magnetic fields, which is most significant at 3 T (11% for 0.5 x 0.5 cm^2), see Figure 5.2. This is a result of reduced lateral scattering of secondary electrons, since the magnetic field acts to focus the trajectories of secondary electrons along the beam direction[30,42]; see chapter 3 for further detail on the impact of inline magnetic fields on dose spread arrays. The relative increase in central axis dose decreases with increasing field size, as lateral electron equilibrium is established.

Perpendicular magnetic field orientation

FWHM and penumbral width values for beam profiles in the perpendicular magnetic field orientation are displayed in Table 5.1. The magnetic field does not significantly change the FWHM, however there was an increase in penumbral width, particularly on the right hand side (see Figure 5.6) of profiles for the smallest field sizes. As the field size increases past 1 x 1 cm^2, the disparity between left and right penumbral widths decreases and the asymmetry of field profiles becomes less pronounced.

The peak intensity of profiles is stable, and equivalent to the response at 0 T (within 2%) for field sizes 2 x 2 cm^2 and above. For field sizes smaller than this, disequilibrium effects induce variability. However this is within a magnitude of 5%. Noise in the phase-space file also contributes some uncertainty to this effect.

Perhaps more important is the observation that the position of the field itself has shifted,

Table 5.1: Magnetic field beam profile characteristics at 1.5 cm depth in water and silicon dosimeter, for inline and perpendicular magnetic field orientations. The lateral field shift was quantified by measuring the change in position of the field edge at half-maximum compared to the 0 T case. The error bounds for FWHM, penumbral widths and field shift is ±0.05 mm.

	Geometry	Field size		FWHM	(mm)	Penumbral	Width	(mm)	Field shift	(mm)
		(cm^2)	0 T	1 T	3 T	0 T	1 T	3 T	1 T	3 T
						L,R	L,R	L,R	L,R	L,R
In-line	Water	0.5 x 0.5	5.3	5.3	5.2	1.8,1.8	1.8,1.8	1.7,1.7	0,0	0.1,0
		1 x 1	10.2	10.2	10.1	2.1,2.2	2.1,2.2	2.0,2.0	0,0	0,-0.1
		2 x 2	20.3	20.2	20.2	2.4,2.3	2.4,2.3	2.2,2.1	0,0	0,0
		3 x 3	30.4	30.4	30.4	2.4,2.4	2.4,2.4	2.3,2.1	0,0	0,0
	M512	0.5 x 0.5	5.9	5.8	5.5	2.6,2.6	2.6,2.6	2.0,2.1	0,0	0.2,-0.2
		1 x 1	10.3	10.2	10.0	3.2,3.2	3.2,3.2	2.3,2.4	0.1,-0.1	0.1,-0.2
		2 x 2	20.4	20.3	20.2	3.5,3.5	3.3,3.3	2.5,2.5	0.1,-0.1	0.1,-0.1
		3 x 3	30.3	30.3	30.2	3.9,3.9	3.6,3.6	2.5,2.5	0.1,0	0.1,-0.1
Perpendicular	Water	0.5 x 0.5	5.3	5.3	5.4	1.8,1.8	1.9,2.3	2.1,2.7	0.4,0.4	0.8,0.9
		1 x 1	10.2	10.2	10.1	2.1,2.2	2.6,2.9	2.9,3.0	0.5,0.5	1.0,1.0
		2 x 2	20.3	20.3	20.2	2.4,2.3	3.0,3.1	3.2,3.2	0.6,0.6	1.1,1.1
		3 x 3	30.4	30.4	30.4	2.4,2.4	3.1,3.2	3.2,3.3	0.6,0.6	1.1,1.1
	M512	0.5 x 0.5	5.9	5.9	6.2	2.6,2.6	2.2,2.6	2.3,3.2	0.7,0.7	1.0,1.4
		1 x 1	10.3	10.3	10.2	3.2,3.2	3.0,3.2	3.6,3.8	0.8,0.8	1.4,1.3
		2 x 2	20.4	20.2	20.2	3.5,3.5	3.6,3.6	4.1,4.0	1.0,0.8	1.5,1.4
		3 x 3	30.3	30.4	30.4	3.9,3.9	3.5,3.6	3.9,4.1	0.8,0.8	1.4,1.4

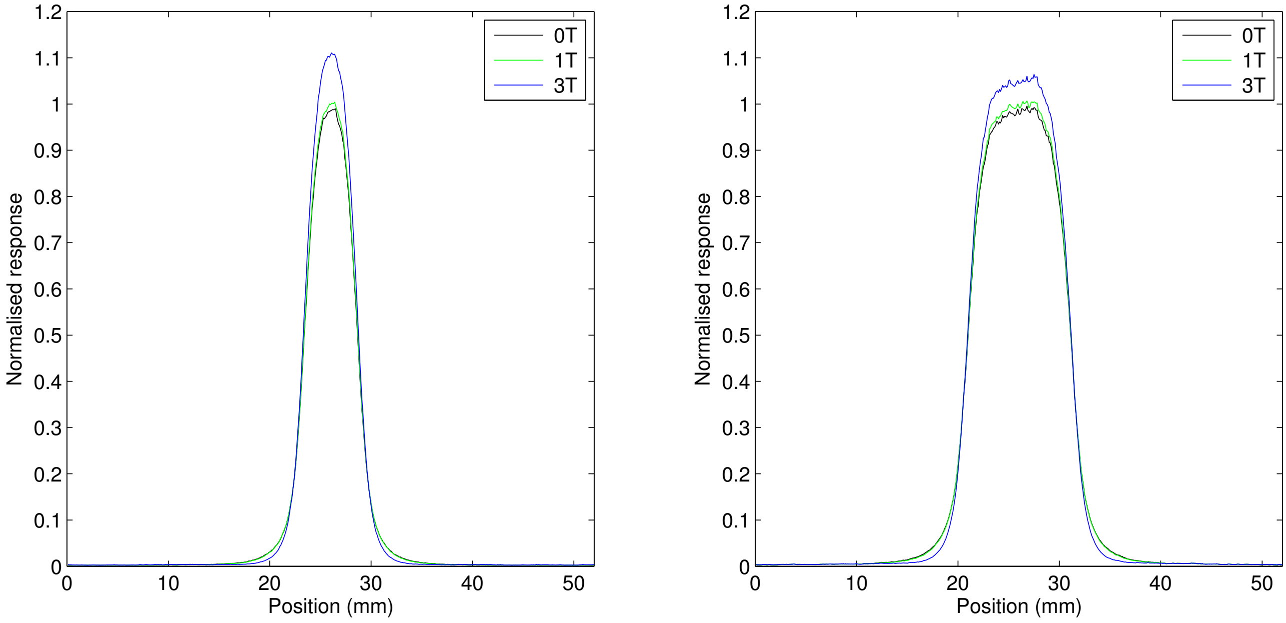

(a)Water, 0.5 x 0.5 cm^2 (b)Water, 1 x 1 cm^2

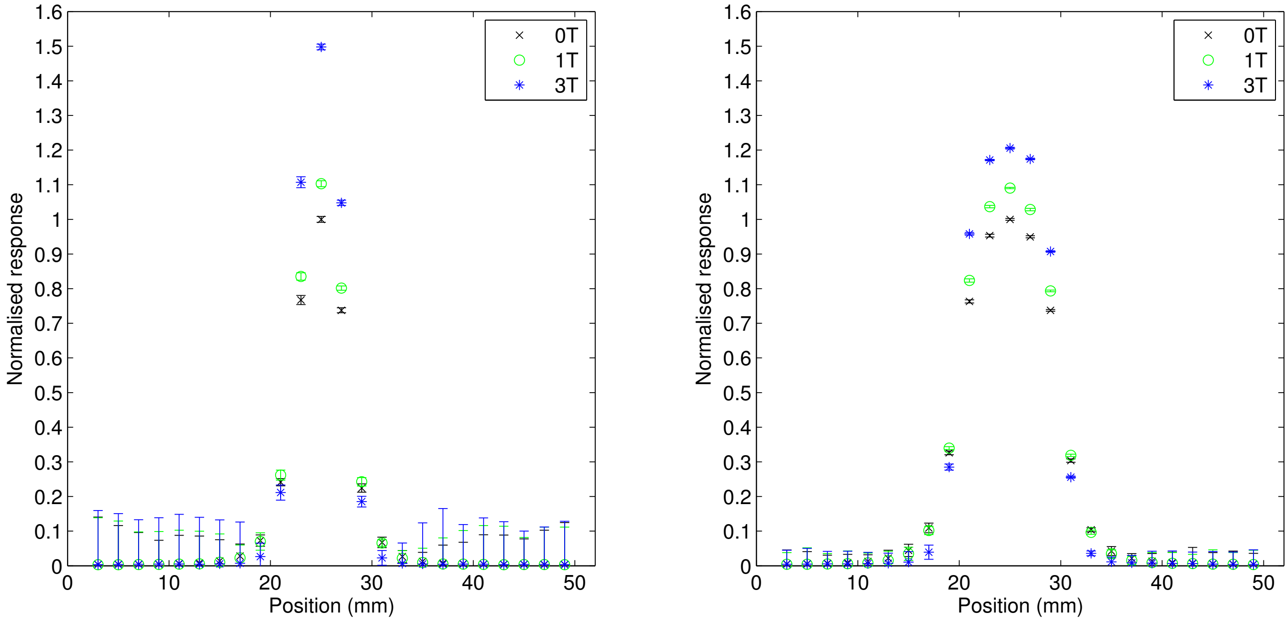

(c)M512, 0.5 x 0.5 cm^2 (d)M512, 1 x 1 cm^2

Figure 5.2: Relative radiation beam profiles part 1, *in-line* magnetic field orientation. Parts (a) and (b) show beam profiles at 1.5 cm depth in water. Parts (c) and (d) show beam profiles in the silicon dosimeter at 1.5 cm depth in a water phantom (note change in y-axis scale).

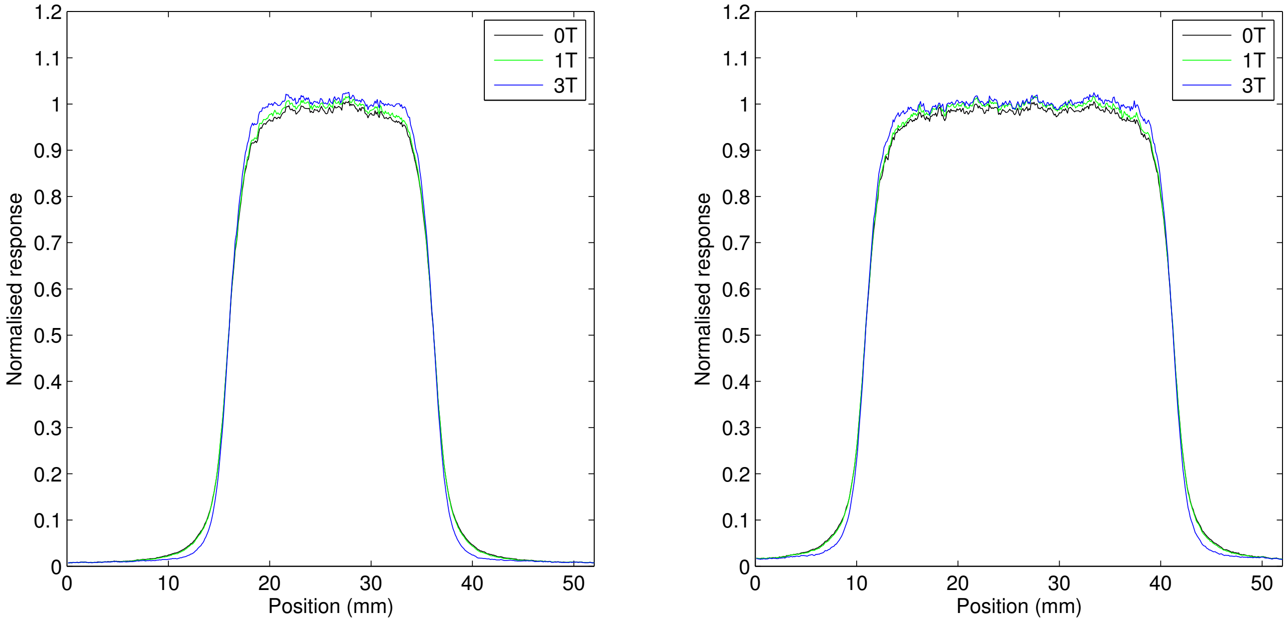

(a)Water, 2 x 2 cm^2 (b)Water, 3 x 3 cm^2

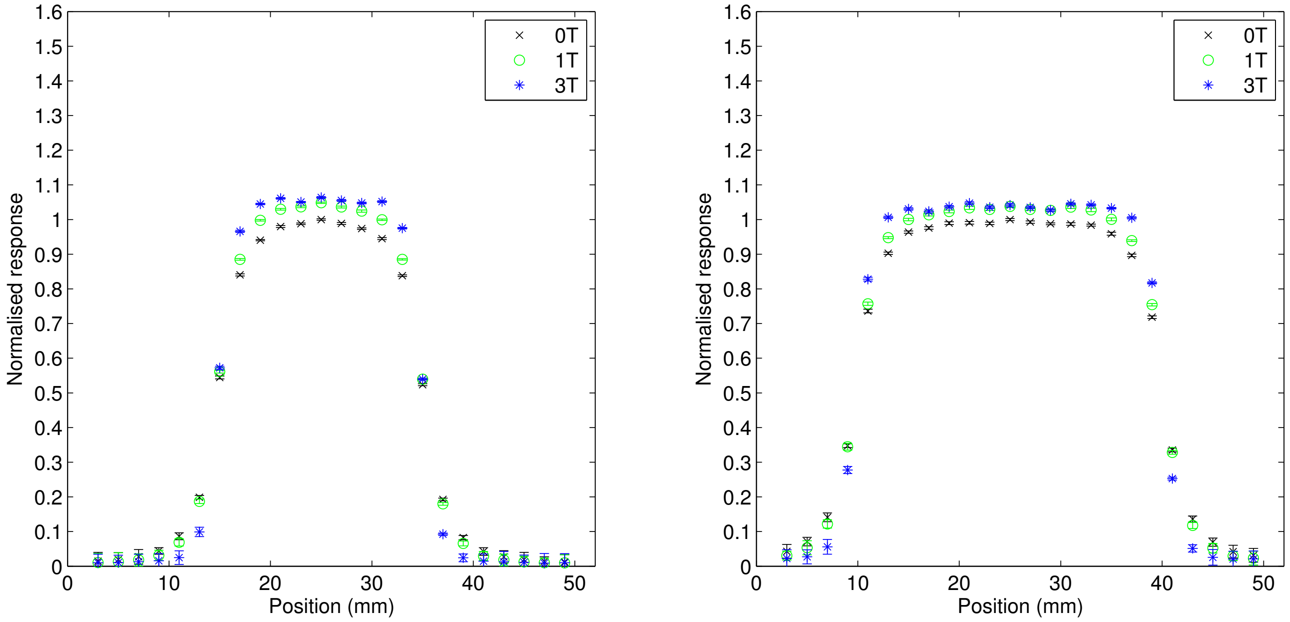

(c)M512, 2 x 2 cm^2 (d)M512, 3 x 3 cm^2

Figure 5.3: Relative radiation beam profiles part 2, *in-line* magnetic field orientation.. Parts (a) and (b) show beam profiles at 1.5 cm depth in water. Parts (c) and (d) show beam profiles in the silicon dosimeter at 1.5 cm depth in a water phantom (note change in y-axis scale).

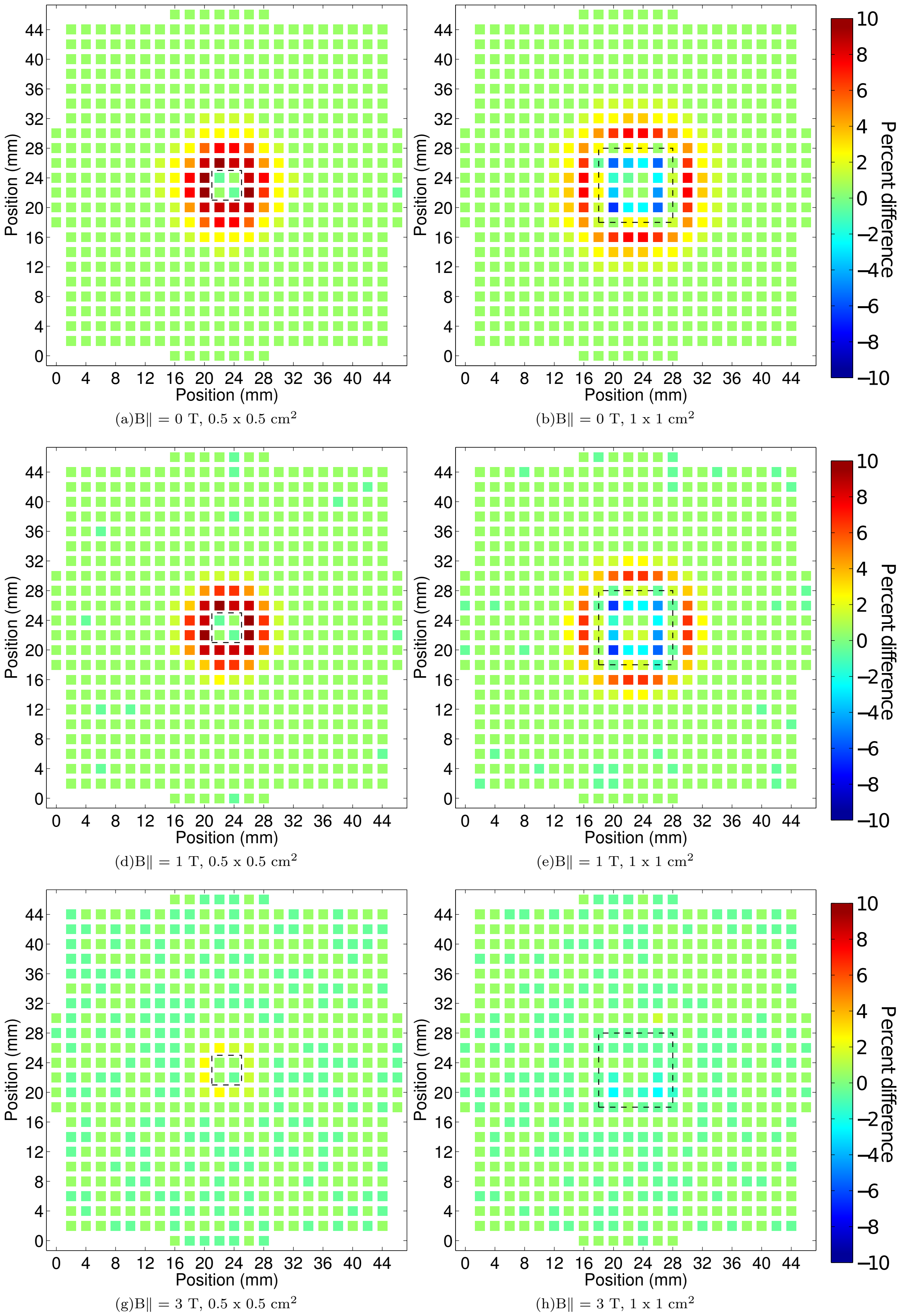

(a)B‖ = 0 T, 0.5 x 0.5 cm^2 (b)B‖ = 0 T, 1 x 1 cm^2

(d)B‖ = 1 T, 0.5 x 0.5 cm^2 (e)B‖ = 1 T, 1 x 1 cm^2

(g)B‖ = 3 T, 0.5 x 0.5 cm^2 (h)B‖ = 3 T, 1 x 1 cm^2

Figure 5.4: Dose difference arrays (silicon - water) part 1, *in-line* magnetic field orientation. Each pixel represents a detector in the array. The dotted line indicates field edge.

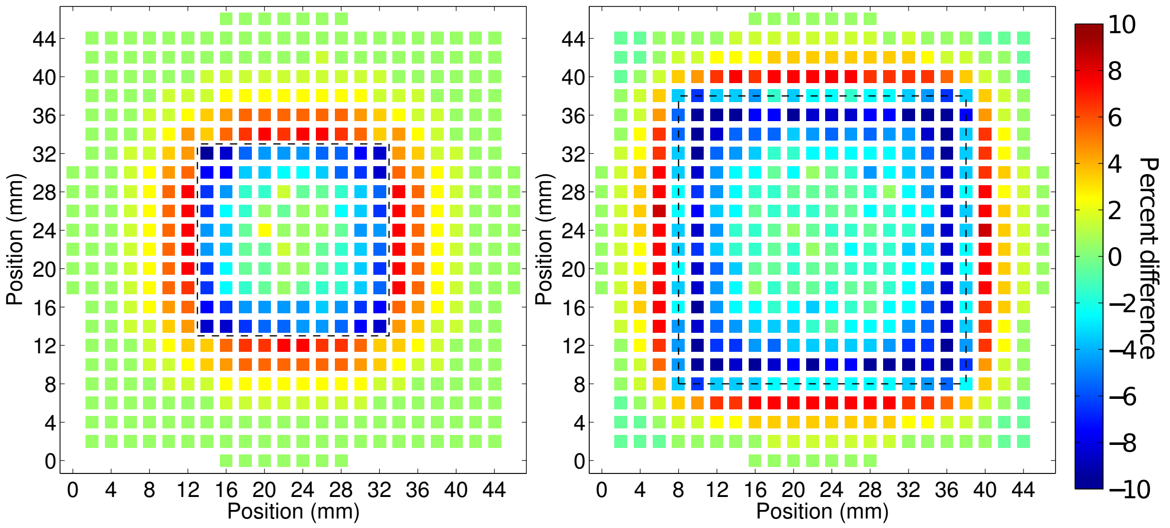

(a)B‖ = 0 T, 2 x 2 cm^2 (b)B‖ = 0 T, 3 x 3 cm^2

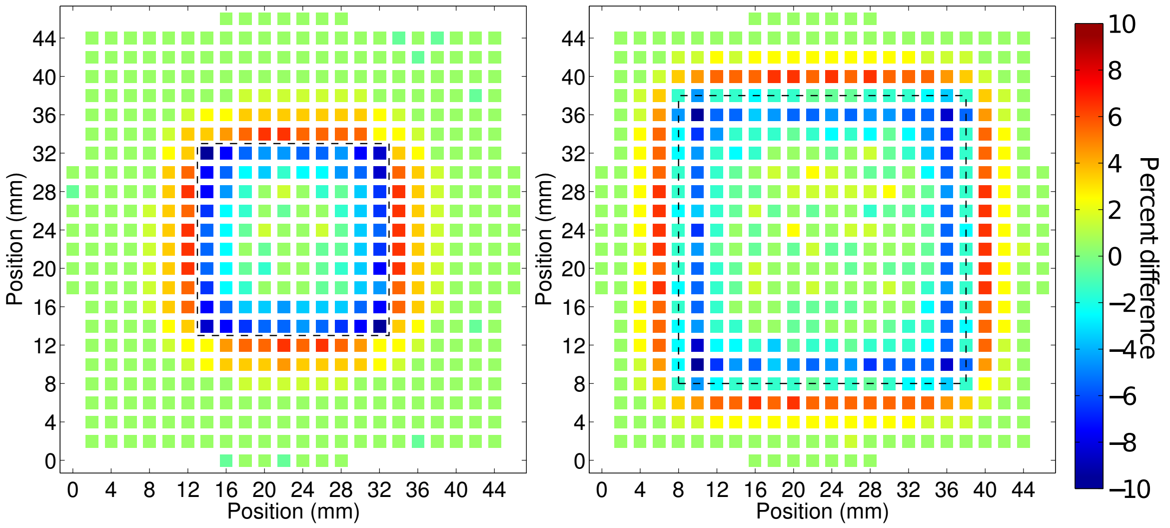

(d)B‖ = 1 T, 2 x 2 cm^2 (e)B‖ = 1 T, 3 x 3 cm^2

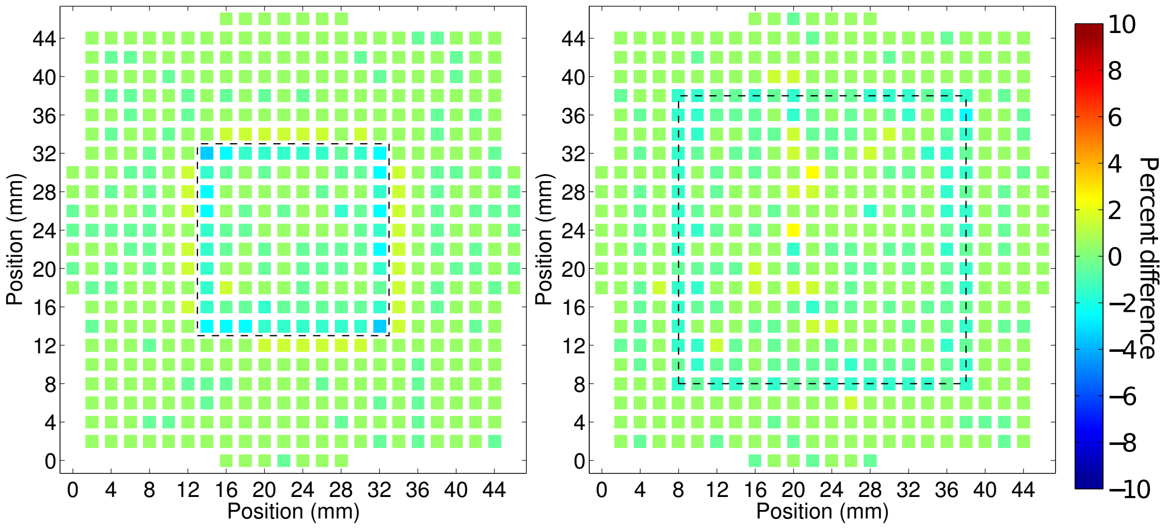

(g)B‖ = 3 T, 2 x 2 cm^2 (h)B‖ = 3 T, 3 x 3 cm^2

Figure 5.5: Dose difference arrays (silicon - water) part 2, *in-line* magnetic field orientation. Each pixel represents a detector in the array. The dotted line indicates field edge.

which is quantified by the change in position of the field edge at 50% dose maximum. In water, the field position shifts by up to (1.10 ± 0.05) mm (at 3 T) in the direction of the magnetic force.

Considering the changes to beam profile characteristics, it would be crucial to use a dosimeter capable of measuring these changes in a clinical setting to be confident in delivery of small field treatments. Dose delivered is most often higher per fraction for small fields compared to larger field treatments, hence requiring high precision pre-treatment assessment of the dose distribution relative to the target location.

5.3.2 Impact of magnetic fields on the MagicPlate-512 model

Figure 5.2, Figure 5.3, Figure 5.6 and Figure 5.7 parts (c) and (d) show beam profiles as measured using the M512 dosimeter geometry, simulated at 1.5 cm depth in a water phantom, for inline and perpendicular orientations respectively. Figure 5.4, Figure 5.5, Figure 5.8 and Figure 5.9 show dose difference maps of the M512, relative to water, for inline and perpendicular orientations.

In-line magnetic field orientation

FWHM and penumbral width data for beam profiles in the silicon dosimeter are shown in Table 5.1. The FWHM as measured with M512 geometry is accurate to that measured in water to within 0.2 mm for field sizes $\geq$ 1 x 1 cm^2. There is a larger discrepancy for the 0.5 x 0.5 cm^2 field size, however disagreement does not exceed 0.6 mm.

At a magnetic field strength of 1 T, the penumbral widths as measured in silicon are larger in magnitude compared to water, by 1 mm on average. This however is not due to the presence of the magnetic field, as this magnitude overestimation is present at 0 T; with application of the 1 T field strength the penumbral width does not change in either water or the M512 by more than 0.3 mm. With the 3 T field applied, the penumbral width as measured in silicon most closely approximates the 0 T case in water (to within 0.3 mm), see Table 5.1. This is clearly shown in the dose difference maps in Figure 5.4 and Figure 5.5, where dose difference maps show the best agreement to water at 3 T, and improved agreement at 1 T, compared to the 0 T scenario. This is due to the 2 mm air-gap above the silicon volume, which gives the magnetic field more opportunity to narrow the distribution of laterally scattered electrons, thus creating a sharper profile and compensating for the overestimation of penumbral width at 0 T.

The dosimeter, like the case for water, sees an increase in the intensity of dose profiles as field strength increases. However, this increase is overestimated - particularly for the 0.5 x 0.5 cm^2 field size. This is due to the air gap above the dosimeter, in which the magnetic field min-

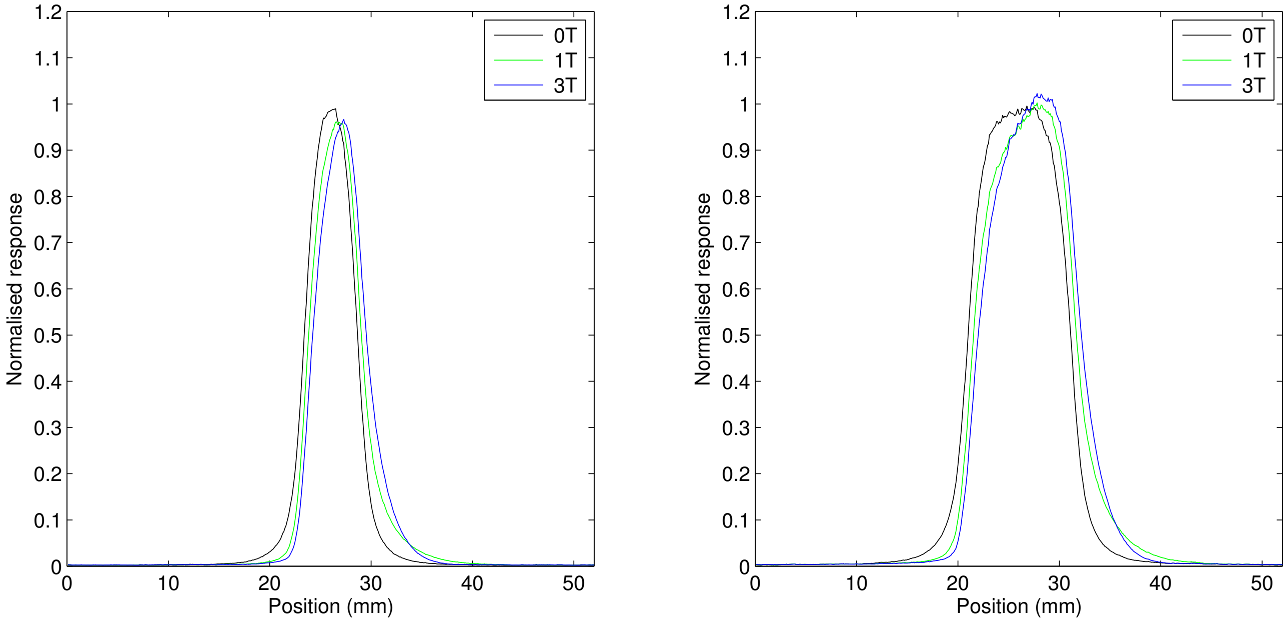

(a)Water, 0.5 x 0.5 cm^2 (b)Water, 1 x 1 cm^2

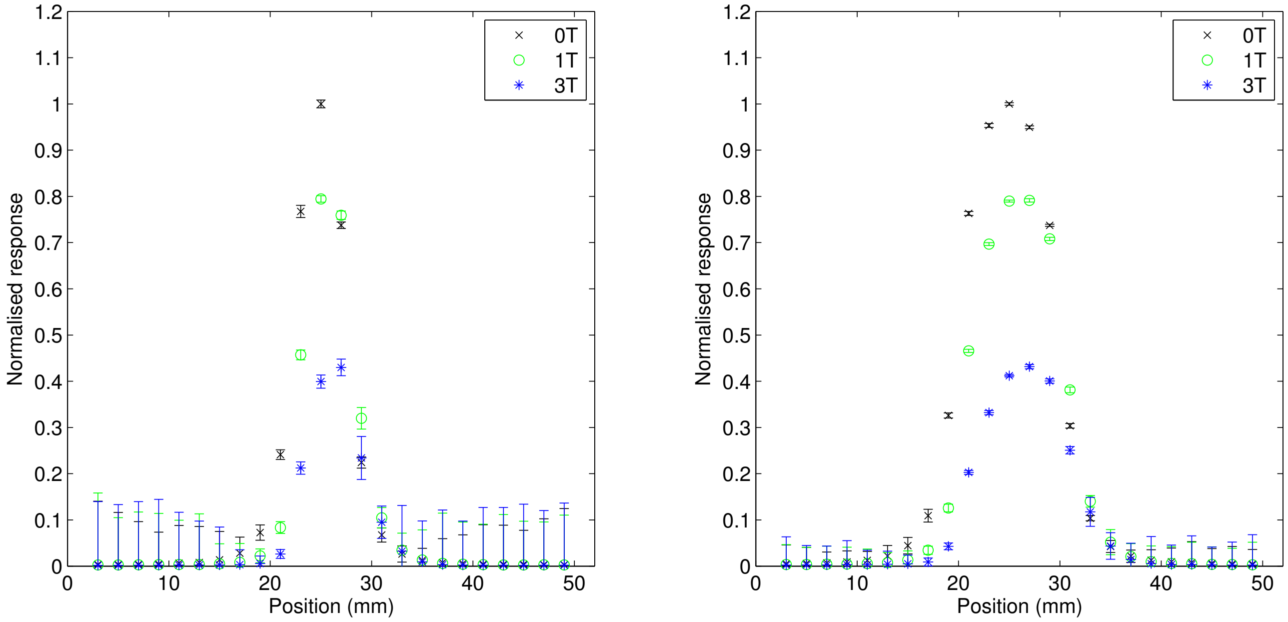

(c)M512, 0.5 x 0.5 cm^2 (d)M512, 1 x 1 cm^2

Figure 5.6: Relative radiation beam profiles part 1, *perpendicular* magnetic field orientation. Parts (a) and (b) show beam profiles at 1.5 cm depth in water. Parts (c) and (d) show beam profiles in the silicon dosimeter at 1.5 cm depth in a water phantom. The Lorentz force is in the left - right direction.

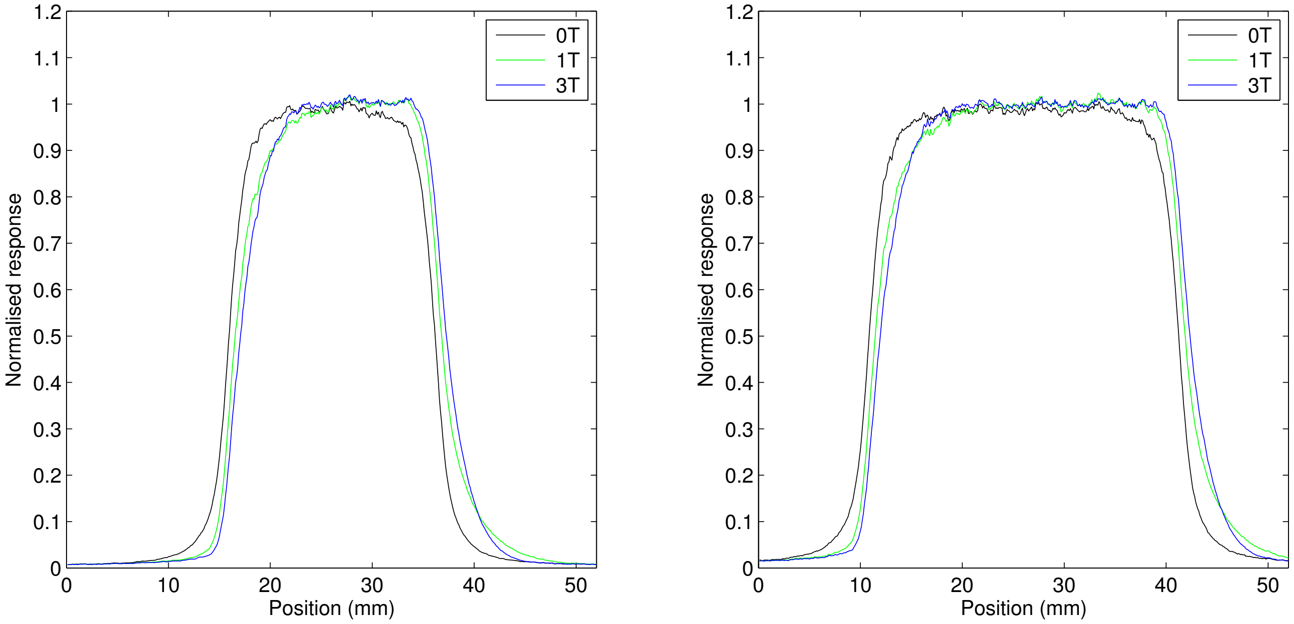

(a)Water, 2 x 2 cm^2

(b)Water, 3 x 3 cm^2

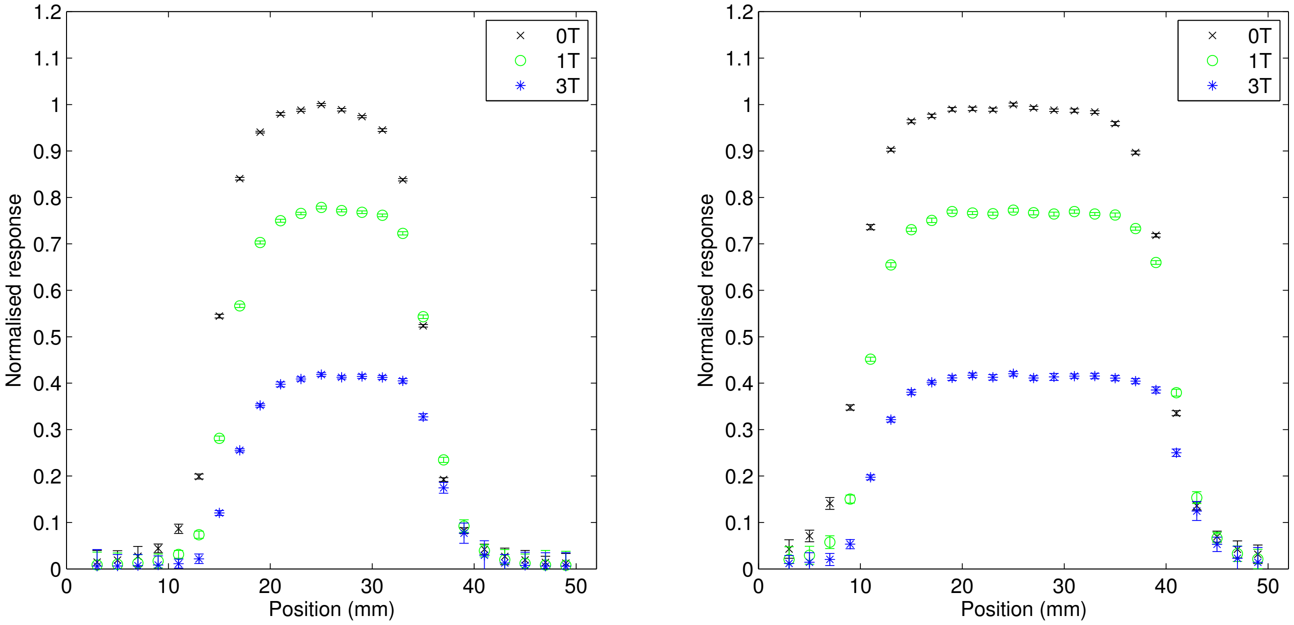

(c)M512, 2 x 2 cm^2

(d)M512, 3 x 3 cm^2

Figure 5.7: Relative radiation beam profiles part 2, *perpendicular* magnetic field orientation. Parts (a) and (b) show beam profiles at 1.5 cm depth in water. Parts (c) and (d) show beam profiles in the silicon dosimeter at 1.5 cm depth in a water phantom. The Lorentz force is in the left - right direction.

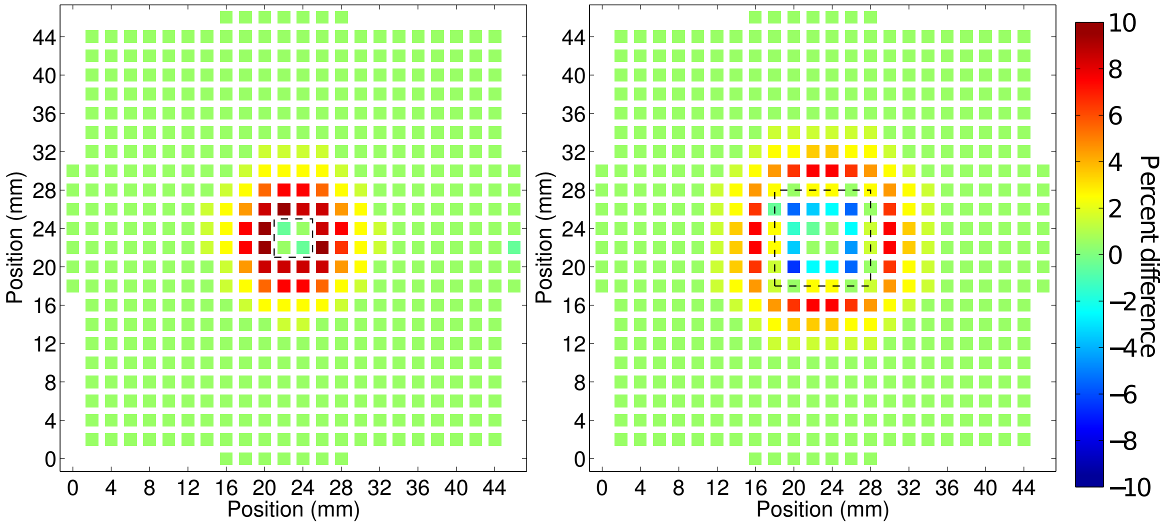

(a)B⊥ = 0 T, 0.5 x 0.5 cm^2 (b)B⊥ = 0 T, 1 x 1 cm^2

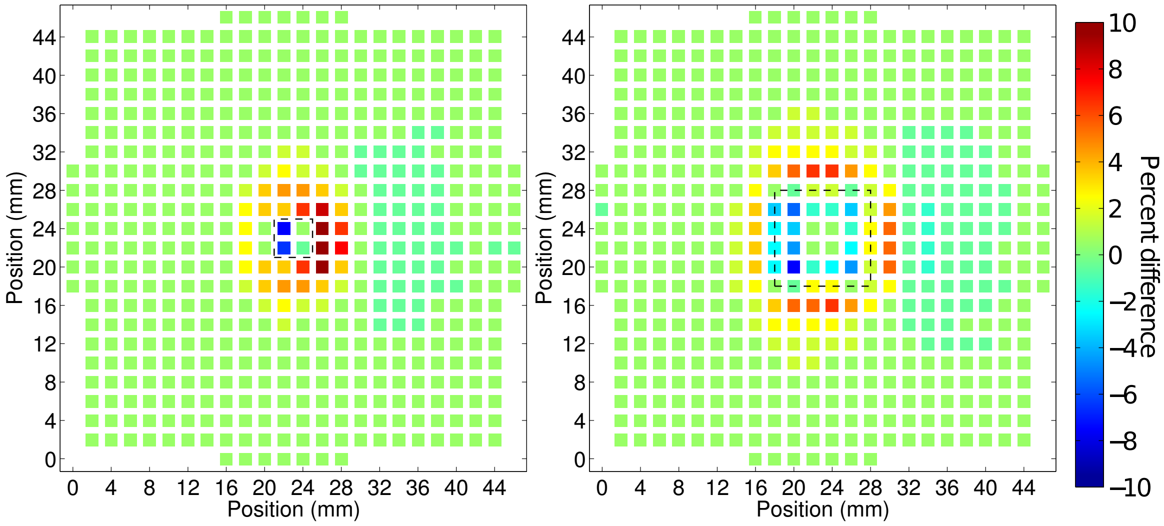

(d)B⊥ = 1 T, 0.5 x 0.5 cm^2 (e)B⊥ = 1 T, 1 x 1 cm^2

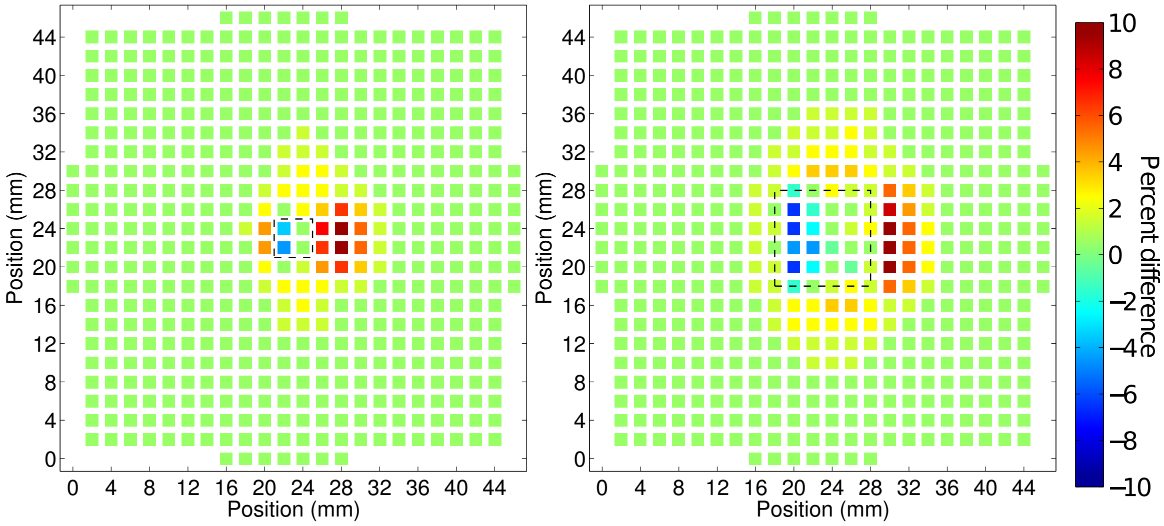

(g)B⊥ = 3 T, 0.5 x 0.5 cm^2 (h)B⊥ = 3 T, 1 x 1 cm^2

Figure 5.8: Dose difference arrays (silicon - water) part 1, *perpendicular* magnetic field orientation. Each pixel represents a detector in the array. The dotted line indicates field edge.

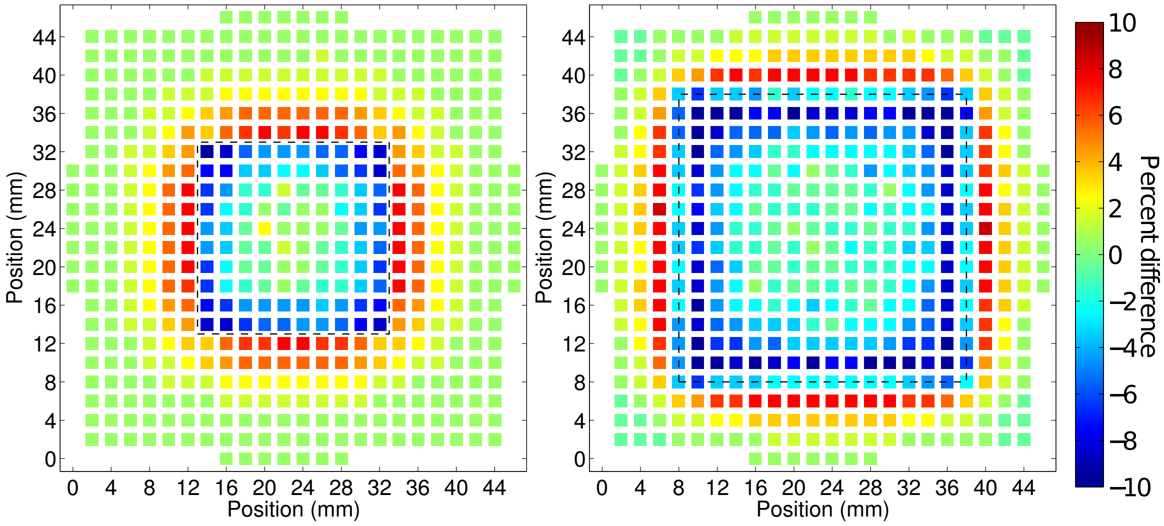

(a)B⊥ = 0 T, 2 x 2 cm^2 (b)B⊥ = 0 T, 3 x 3 cm^2

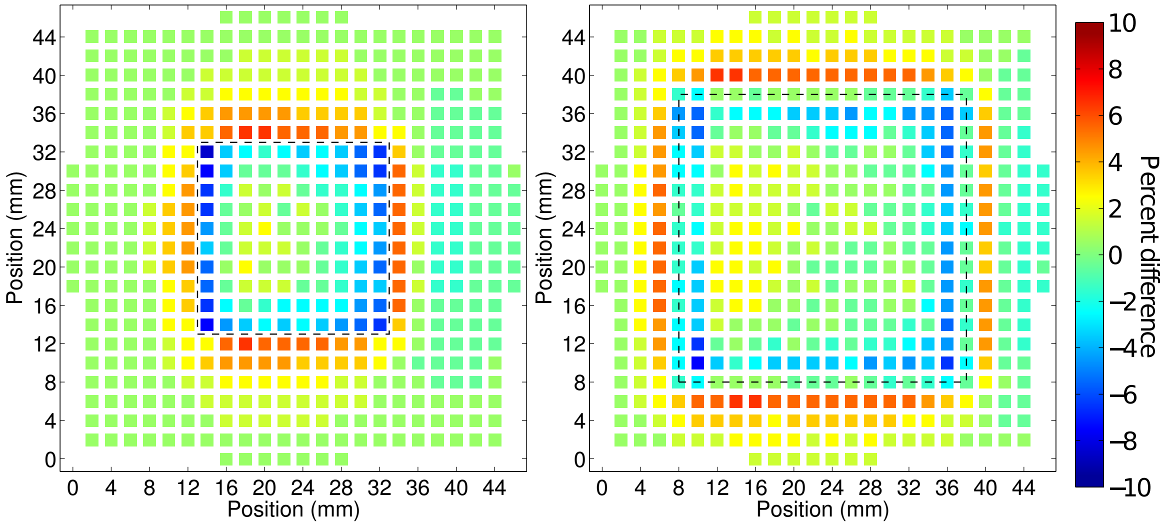

(d)B⊥ = 1 T, 2 x 2 cm^2 (e)B⊥ = 1 T, 3 x 3 cm^2

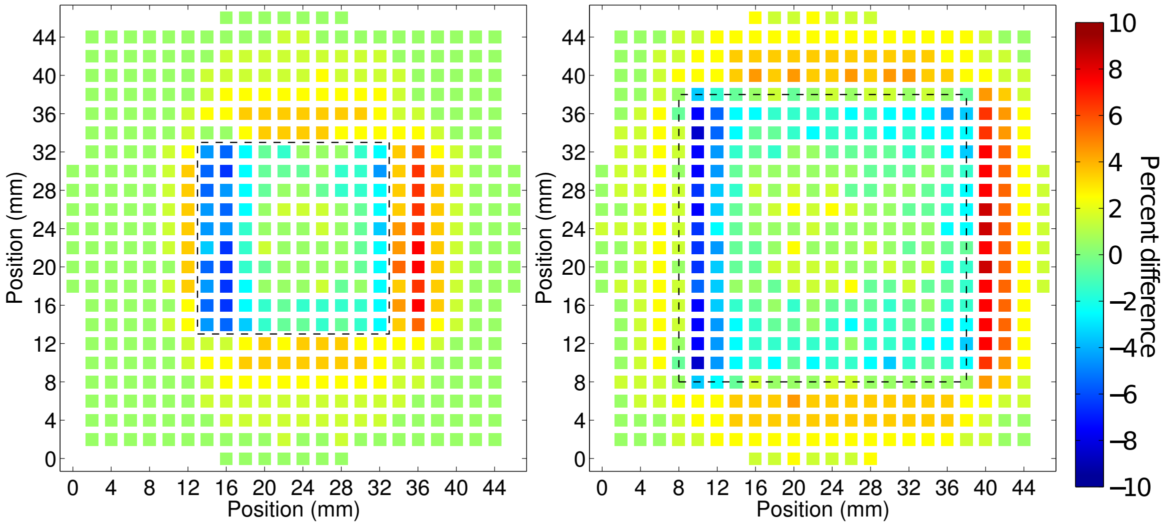

(g)B⊥ = 3 T, 2 x 2 cm^2 (h)B⊥ = 3 T, 3 x 3 cm^2

Figure 5.9: Dose difference arrays (silicon - water) part 2, *perpendicular* magnetic field orientation. Each pixel represents a detector in the array. The dotted line indicates field edge.

imises lateral scatter and focuses dose toward the following interface - in this case the sensitive detector layer. This effect is further magnified as the level of lateral electronic disequilibrium more severely deteriorates, as is the case for the smallest field sizes. Resolution of this effect by elimination of the air gap is further discussed in section 5.3.3.

Perpendicular magnetic field orientation

Table 5.1 contains beam characteristic data for the silicon dosimeter in perpendicular magnetic fields. The FWHM of beam profiles measured in the silicon dosimeter are similar to that of water for field sizes 1 x 1 cm^2 and larger. For penumbral width measurements, results are generally within 0.5 mm agreement to water at 1 T, however for the 3 T case there is disagreement of 0.9 mm. By simulating the dosimeter without the air-gap, the penumbral width disparity compared to water for 3 T improves from a 0.9 mm overestimation to agreement within 0.5 mm. Hence it can be inferred that this is the result of distortion of field profile due to electron return effects occurring in the air gap. This will be discussed further below.

The dose difference maps comparing M512 to water in Figure 5.8 and Figure 5.9 parts (d) and (e) show that there is excellent agreement between silicon and water at 1 T, which even exceeds the 0 T scenario. This is due to the accuracy with which the dosimeter measures penumbral width and field position, which is within 0.5 mm and 0.3 mm respectively. At 3 T the agreement is also improved, however not the same degree as for the 1 T field strength. As is shown in parts (g) and (h) of Figure 5.8 and Figure 5.9, the disagreement of dosimeter response to water is confined to the field edges in parallel with the magnetic force. This is due to a combination of the overestimation of penumbral width, as well as field position. The magnitude of disagreement to the water-equivalent response is 6%. Considering the steep dose gradient of this region (approx. 20%/mm), and the small magnitude of field position misalignment, this is a small spatial difference.

The dose profiles in Figure 5.6 and Figure 5.7 show a decrease in measured dose to the silicon chip as the magnetic field strength increases. The loss in dose is as high as 23% for 1 T, and 57% for 3 T magnetic field strengths. The magnitude of dose loss is not dependent on field size. This is due to ERE occurring in the air-gap above the dosimeter. Secondary electrons are being directed back into the PMMA above the air-gap by the magnetic field, and hence away from the dosimeter (confirmed by running simulations with no air-gap, see section 5.3.3). The increasing dose loss as the field strength increases is due to the decreasing radius of curvature; at 3 T the radius is tighter, and hence a higher proportion of secondary electrons are returned to the PMMA-air interface rather than traversing the air gap.

5.3.3 Impact of air-gap around MagicPlate-512

As is demonstrated in Figure 5.10 and Figure 5.11, replacing the air-gap above the dosimeter with PMMA reduces the changes in dose response due to magnetic field effects occurring within the dosimeter. This means the dosimeter no longer dramatically overestimates CAX response in the inline orientation, which for the 0.5 x 0.5 cm^2 field size was as much as 50%. Eliminating the air-gap also improves CAX response in the perpendicular orientation by reducing dose loss due to ERE. However it does not eliminate this effect completely, as some dose loss is still observed (8% at 1 T, 23% at 3 T). This will be further addressed experimentally in chapter 5.

Without the air-gap, penumbral width measurements are also a closer approximation to water. For the 3 T case (1 x 1 cm^2 field size), penumbral widths were overestimated by up to 0.9 mm; by eliminating the air-gap agreement is to within 0.5 mm. However, the degree of field shift due to the perpendicular magnetic field is underestimated by (0.40 ± 0.05) mm, whereas previously the air-gap caused an overestimation of the same magnitude.

These results demonstrate the importance of controlled experimental set-up conditions, as inhomogeneities (air-gaps in particular) can significantly affect the outcome of results. While it is demonstrated above that, at 1 T at least, beam profile characteristics can be accurately estimated using normalised profiles with the current dosimeter geometry (i.e. including a 2 mm air gap above the dosimeter), if the dosimeter is used in an absolute capacity the air gap should be resolved. This is in practice difficult, due to the fragile nature of the silicon chip and associated detector channel read-out connections. Solutions to this will be further discussed in the next chapter.

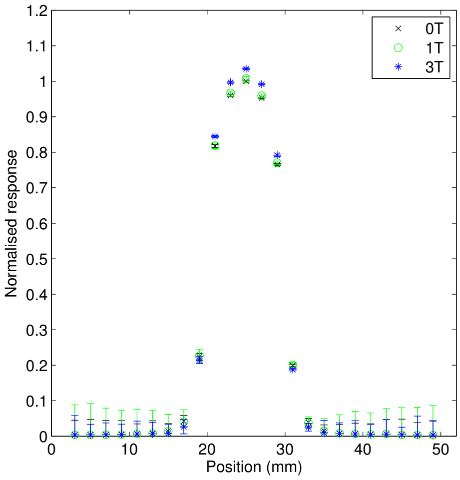

(a)M512 - no air-gap, in-line

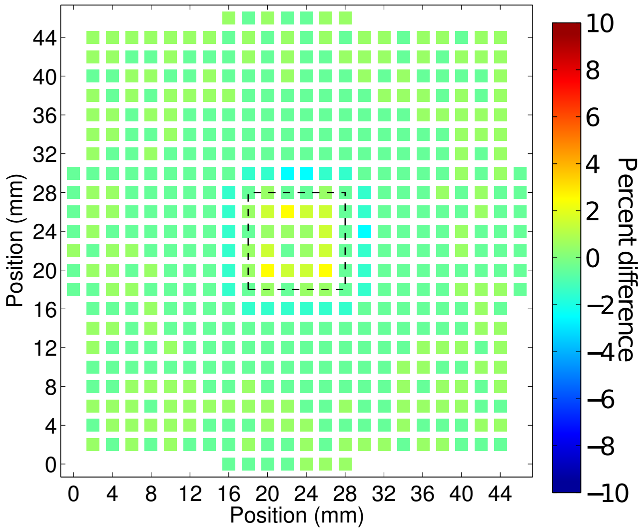

(b)B|| = 1 T

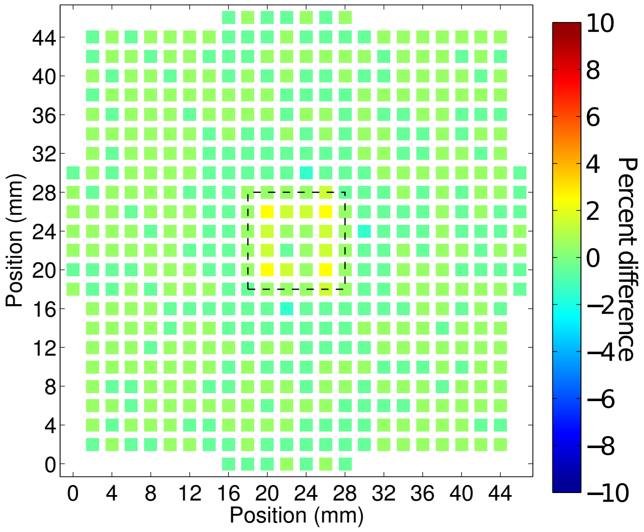

(d)B|| = 3 T

Figure 5.10: *Inline* orientation. Part (a) displays dose profiles in the silicon dosimeter for 1 x 1 cm^2 field size with no air-gap around the dosimeter. Parts (b) and (d) display dose difference maps of the silicon dosimeter with no air-gap around the dosimeter compared to water, for 1 x 1 cm^2 field size at 1 T and 3 T respectively.

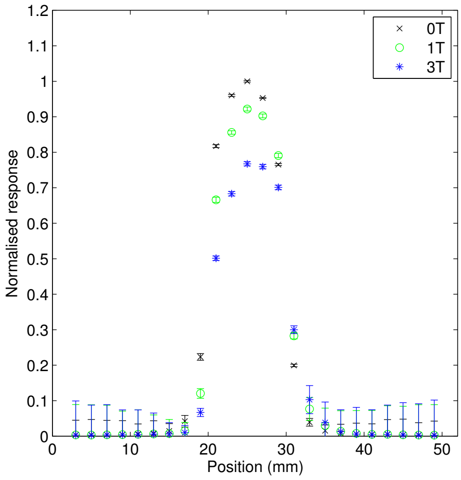

(a)M512 - no air-gap, perpendicular

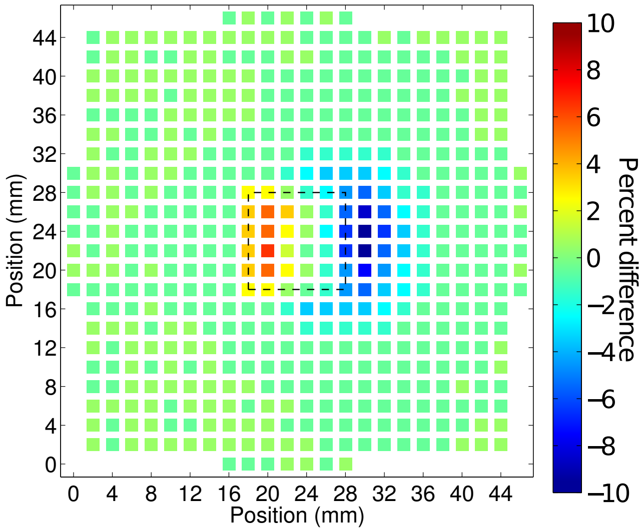

(b)B⊥ = 1 T

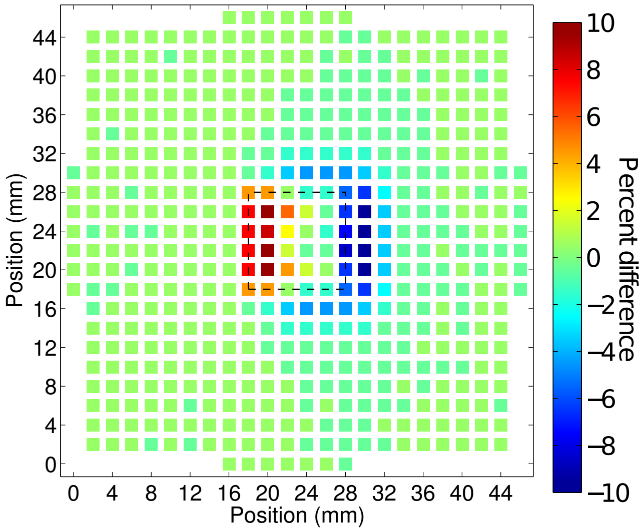

(d)B⊥ = 3 T

Figure 5.11: *Perpendicular* orientation. Part (a) displays dose profiles in the silicon dosimeter for 1 x 1 cm^2 field size with no air-gap around the dosimeter. Parts (b) and (d) display dose difference maps of the silicon dosimeter with no air-gap around the dosimeter compared to water, for 1 x 1 cm^2 field size at 1 T and 3 T respectively.

5.4 Conclusion

Monte Carlo simulations of the MagicPlate-512 have been performed. Sub-millimetre accuracy in FWHM and penumbral width measurement was achievable (with respect to water), which in most cases exceeded 0.5 mm. ERE was observed to occur in the 2 mm air gap above the dosimeter, which in the perpendicular orientation resulted in a decrease in response of up to 23% for 1 T and 57% for 3T. Consequences of the air gap were further investigated in the next chapter, where practically applicable solutions to resolving the air gap are applied experimentally.

The results presented in this chapter indicate that the M512 will be appropriate for beam profile measurement in MRI-linacs, which at this point in time employ a maximum field strength of 1.5 T in the perpendicular orientation and 1 T in the inline orientation. Considering the larger pitch of commercial 2D array dosimeters considered in the literature (e.g. IC Profiler[52]), the M512 presents itself as a superior option for real-time small field beam profile reconstruction in magnetic fields.

The results presented in this chapter should be considered in conjunction with the experimental measurements performed with the dosimeter, reported in chapter 6.

Chapter 6

Experimental measurements with a high resolution 2D silicon array dosimeter in a permanent magnet system

The results presented in this chapter have been published in the journal Biomedical Physics and Engineering Express:

M Gargett, B Oborn, S J Alnaghy, T Causer, M Petasecca, A B Rosenfeld and P Metcalfe, A high resolution 2D array detector system for small-field MRI-LINAC applications, *Biomedical Physics & Engineering Express*, vol. 4, no. 3, 2018.

6.1 Overview

This chapter includes the results of experimental measurements performed with the MagicPlate-512 (M512) dosimeter in a permanent magnet system, named Magnetic Apparatus for RaDiation Oncology Studies (MARDOS). MARDOS was specifically designed to be used in conjunction with a clinical linear accelerator. It can be configured in both inline and perpendicular magnetic field orientations, for field strengths 0.95T and 1.2T respectively, as well as a 0 T arrangement.

Of the CMRP-designed dosimeters discussed thus far in this thesis, only the M512 has been used for experiments in MARDOS; this is because MARDOS limits the measurable field size to 5 x 5 cm^2 in the plane of the dosimeter. As such, it is intuitive that the dosimeter designed for small field dosimetry be used. As discussed in chapter 5, the M512 is a monolithic silicon dosimeter with 512 detection pixels (dimension 0.5 mm x 0.5 mm) in a high density arrangement of 2 mm pitch, which is of a higher resolution than commercial diode/chamber array detectors currently available. The M512 has a fast, online read-out that makes it a desirable option for real time measurement compared to other high resolution methods commonly used for small field applications, such as film. The M512 has been commissioned for small field dosimetry applications down to field sizes of 0.5 cm dimension by Aldosari et al[70]. Its angular response has been characterised by Stansook et al[71].

The experimental results presented in this chapter are crucial in confirming the trends observed in Monte Carlo simulations of the dosimeter in chapter 5.

6.2 Materials and Methods

6.2.1 2D silicon array dosimeter

The M512 consists of a thin monolithic silicon wafer (52 x 52 x 0.47 mm^3) with 512 ion-implanted pixels (0.5 x 0.5 mm^2). The pixels are spaced evenly with 2 mm pitch, covering a maximum detection area of 46 mm x 46 mm. A small air-gap exists above the silicon chip to counteract dose enhancement that occurs for small field sizes due to different scattering and secondary electron spectra in silicon compared to water[122,123]. The air gap size has been optimised to a water equivalent response at zero magnetic field conditions[71]. The dosimeter has a fast FPGA-based read-out system with 8 x 64-channel ASIC chips, and is synchronized with the linac to allow read out of all pixels pulse-by-pulse[68,69]. For the experiments detailed in this chapter, a specialised read-out electronics set was constructed, which was modified for magnetic field compatibility. This included replacement of ferromagnetic parts and the extension of cabling to distance the electronics from the dosimeter. Readout of the dosimeter is performed using custom-designed software. The radiation response of the M512 dosimeter has been successfully characterised previously by Aldosari et al[70] and Stansook et al[71] for small field dosimetry applications. Full details on literature relating to the dosimeter is contained in section 2.4.2.

In order to calibrate the dosimeter in terms of a charge-to-dose relation, the raw reading collected by the detector first needed to be converted to charge. This was done by scaling the raw value according to the gain range used for acquisition. For these experiments, this corresponded to a maximum charge of 2.4 pC at the nominal gain range of 4 for the AFE0064. The raw “counts”, which are normalised to the AFE0064-specific range factor of 65535, are multiplied by this maximum charge range value to obtain a reading in the units of pC.

The charge to dose conversion was performed under the reference conditions of the linac used.

That is, for a 6MV beam, 100MU equates to 100cGy delivered to the CAX of a 10 cm x 10 cm field at 1.5 cm depth in water with the phantom at 100 cm SSD. Under these reference conditions the charge reading (pC) to dose relationship was obtained for exposures in the range 0.2 - 5 Gy, in a method analogous to that used for net OD to dose conversion for radiochromic film. The linearity of the response of the dosimeter is confirmed.

As part of the calibration process, a flood field measurement was also obtained, to adjust the gain sensitivity of each individual pixel of the array. This involved irradiating the dosimeter with a nominally flat radiation field of size 20 x 20 cm^2 at 10 cm depth in a water phantom. From this, an equalisation matrix is created that is normalised to the central pixel, and applied to each measurement. The calibration was performed with no magnetic field present.

As will be described in the following section, the M512 was used at an extended source-to-detector-distance (SDD). A dose-per-pulse correction (approx. 2%) was applied to the dosimeter response, as per the characterisation of the dosimeter[70].

6.2.2 EBT3 film dosimetry

Measurements performed with the M512 were repeated using Gafchromic EBT3 film for benchmarking. Each film measurement was repeated, with a total of 3 separate exposures collected for each experimental setup. A custom made plastic case was used to hold the film in the magnet device, in order to mimic the exact position of the M512 silicon chip (see Figure 6.1). Film preparation and handling procedures outlined in the AAPM Task Group 55 report were followed[124]. Both calibration and experimental films were from the same batch. Each piece was cut in landscape orientation, as recommended by the manufacturer. Orientation was kept consistent throughout the scanning process (the importance of which is discussed in chapter 2). Films were scanned on an EPSON 10000XL flatbed scanner (model recommended by the manufacturer, ISP), at 150dpi resolution. A template was used so the film was placed in a reproducible position between pre- and post-irradiation scans. The films were scanned in the central 10 cm of the scanner, where uniformity is within 1%[73]. Each film was scanned six times, with the first three scans discarded to eliminate warm-up effects of the scanner. The average of the last three scans was used for analysis, which was performed using the ImageJ software package. The red channel was used for net OD to dose conversion, using equation 2.3. A 4^{th} order polynomial was fitted to the calibration curve to establish the net OD - dose relationship. The calibration curve is shown in Figure 6.2. The estimated standard uncertainty associated with film dosimetry results presented is ±4%.

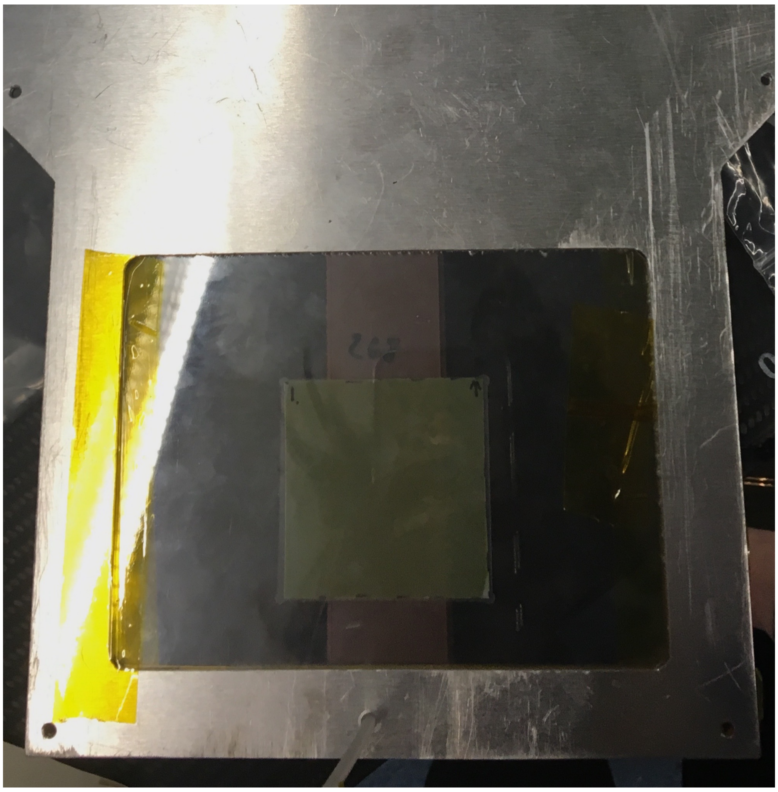

Figure 6.1: The custom film holder used in the permanent magnet device to replicate the precise position of the silicon dosimeter.

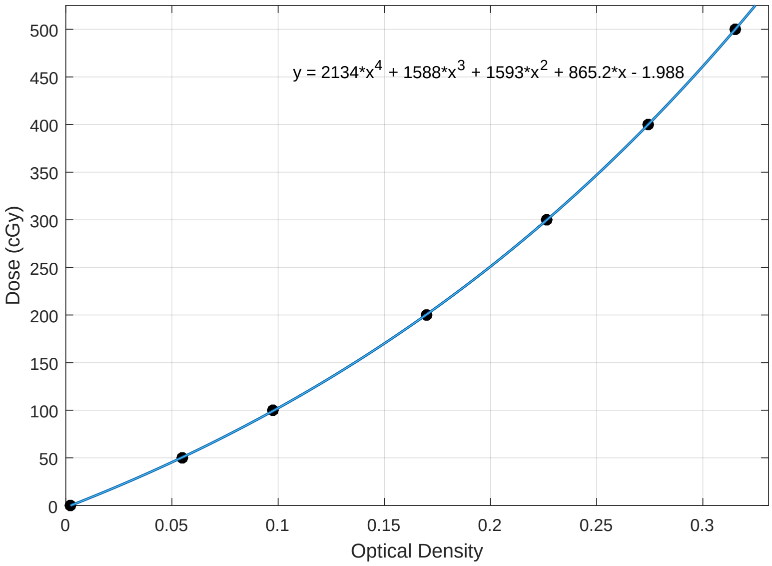

Figure 6.2: EBT3 Gafchromic film calibration curve produced to convert optical density to dose.

6.2.3 Experimental measurements in a permanent magnet system

A permanent magnet system was manufactured specifically for testing dosimetry devices under magnetic field conditions on standard clinical linear accelerators. The system produced uniform magnetic fields in which the M512 was used to collect field profiles for 6MV photon beams. The system is composed of opposing banks of neodymium-iron-boron magnets (in a 5 x 5 matrix arrangement) in a steel yoke, with steel focusing cones. The focusing cones focus the magnetic flux across the pole gap. Using the COMSOL Multiphysics^{TM} software (v4.4), a finite element method was used to create a 3D magnetic field map model of MARDOS, which was used to develop the design of the device. The cone tip design was optimised to produce uniform magnetic fields of strengths approaching 1 T and greater. This was an important aim, as this is the field strength that will be used in the Australian MRI-linac facility. Magnetic field maps of the device, in the inline and perpendicular configuration, are shown in Figure 6.3. Parts (e) and (f) show the magnetic field strength in the plane of the dosimeter, at the measurement position for results presented in this chapter.

The field strength was verified once the device was constructed. A MAGSYS HGM09s handheld gaussmeter was used to measure the magnetic field flux density produced by the apparatus, as verification of the COMSOL-produced magnetic field maps. The device has a maximum measurement range of 4.5 T, with a 1 mT resolution. A raster-style scanning method (2 mm resolution) was used to produce a measured magnetic field map in the central horizontal plane of the device. The agreement of the measured to the modelled magnetic field map was within ± 2.1%[125].

The configuration allows for the radiation beam to enter the magnetic field in both inline and perpendicular orientations; see Figure 6.4. Each field orientation configuration has a customised cone tip; a pulley system is used to exchange the cones in and out of the device. The magnetic isocentre of the device is between the tips of the steel cones.

A zero-field replica of the system was manufactured to perform zero-field measurements. Because the scatter conditions of the magnet are unique, it was important to be able to draw comparisons to zero magnetic field conditions in equivalent scatter conditions. This zero field replica employed the same focusing cones as for the magnetic system, to achieve precisely the same scatter conditions and also reproducible placement of detectors in relation to the cones.

In the inline orientation, an approximately uniform (within ±2%) 0.95 T magnetic field is produced over the volume between the cone tips, with a cross-sectional area of 3 x 3 cm^2. The M512 dosimeter was placed centrally between the focusing cones, at a source-to-axis distance of 150 cm. The maximum distance between the cone tips is 3 cm in this configuration; this

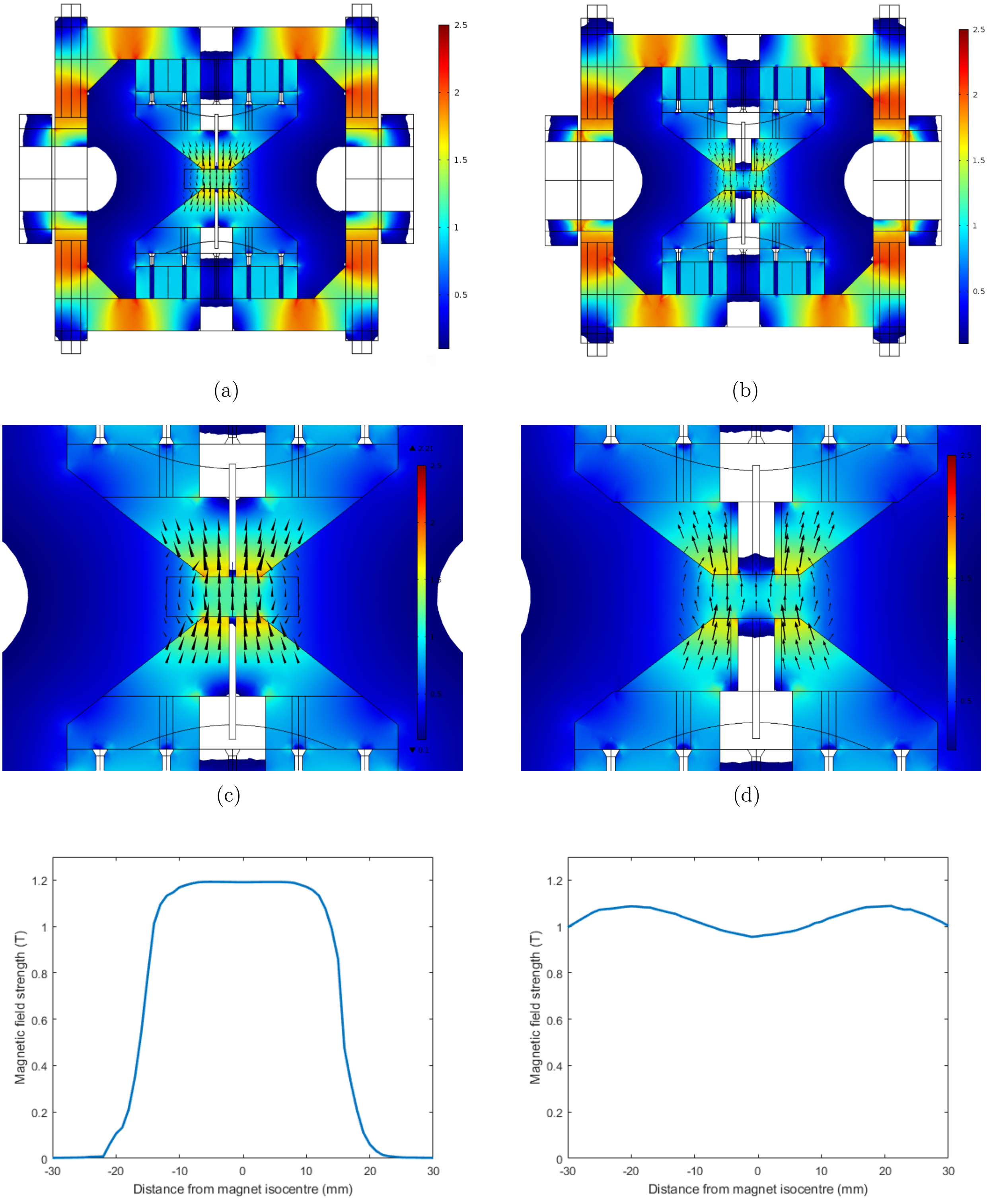

(a) (b)

(c) (d)

(e) (f)

Figure 6.3: Magnetic flux density maps of the MARDOS device. Parts (a) and (c) show the perpendicular magnetic field orientation. Parts (b) and (d) show the inline orientation. Arrows represent the magnetic field direction and flux density across the pole gap, where the detector was placed in the system. Parts (b) and (d) and magnified views of parts (a) and (c). Units: T. The magnetic field strength in the dosimeter's plane of measurement is plotted for perpendicular and inline orientations in parts (e) and (f), respectively.

allowed 1.7 cm of buildup and 1.2 cm of backscatter material to be placed around the dosimeter (phantom cross section 5 cm). Field profiles for beams of size 0.8 x 0.8 cm^2, 1.4 x 1.4 cm^2 and 2.0 x 2.0 cm^2 in the plane of the detector were collected.

In the perpendicular orientation, a uniform 1.2 T magnetic field is produced over an area 5 x 3 cm^2. The dosimeter was again placed centrally in the magnetic field, although in this instance in a slot machined into the focusing cones. This configuration allowed 5 cm of buildup and 5 cm of backscatter material to be placed around the dosimeter (phantom cross section 3 cm). Field profiles for beams of size 0.8 x 0.8 cm^2, 1.5 x 1.5 cm^2 and 2.3 x 2.3 cm^2 in the plane of the detector were collected in this orientation.

In order to produce these magnetic field strengths, a compromise must be made that involves placing the focusing cones close enough to one another such that phantom side-scatter material was unable to be placed around the dosimeter. Hence, the field profiles collected will not be representative of profiles measured in a homogeneous phantom; the Monte Carlo simulation data presented in chapter 5 can be referred to for this.

The phantom materials used for these experiments included solid water and lung equivalent material, RMI-457 and RMI-455 (Gammex RMI, Middleton, WI). Solid water was chosen for its water (and soft tissue) equivalent properties in MV photon beams. Solid lung was chosen to investigate magnetic field profile changes in a low-density media, in which the extended path length of secondary electrons is expected to intensify the effect of the magnetic field on dose profiles, as was inferred from the results presented in chapter 3.

In the perpendicular magnetic field orientation, the effect of the size of the air gap above the M512 was also analysed, to quantify the expected variations in response due to ERE. Profiles were collected with a variable recess above the sensitive layer, creating a 2 mm air gap (the standard air gap, optimised for zero-field conditions), as well as a 2.9 mm air gap. A 0 mm air gap geometry was also created by filling the 2 mm recess with a tissue equivalent bolus material. It was necessary to use a soft bolus material because the delicate nature of the silicon chip prevents direct contact of the solid water phantom to the detector; there are also conductivity issues related to contact between solid water and the silicon chip.

6.2.4 Beam profile analysis

MATLAB was used to fit a “shape-preserving interpolant” to beam profiles, which is a piecewise cubic Hermite interpolant. The fit was used to quantify full width at half maximum (FWHM) and penumbral widths (80% - 20%). In the case of the perpendicular magnetic field orientation,

Figure 6.4: Experimental setup. The left image shows the MARDOS device positioned along the central beam axis of a clinical linear accelerator, with the magnet's isocentre at 150 cm SAD. The top right image shows the M512 in a solid water phantom (1.7 cm buildup and backscatter) positioned between the focusing cones of MARDOS, in the inline orientation, within the 0.95 T magnetic field. The middle right figure shows the M512 positioned within slots machined in the focusing cones, in the perpendicular orientation in a 1.2 T magnetic field. The bottom right image also shows the M512 in the perpendicular setup, within the solid water phantom (5cm buildup and backscatter).

the profile shape is distorted laterally, in the direction of the magnetic field. This means that the dose maximum does not correspond to the CAX in the case of the smallest field sizes investigated. The profiles were normalised to the dose maximum, off central axis, when calculating FWHM and penumbral width. All measurements quoted have been rounded to the nearest 100 μm, as this was estimated to be the lower limit of reliability of the shape-preserving interpolant fit. This was determined using Monte Carlo data, by comparing the fit applied to 2 mm scoring resolution data (to be representative of the 2 mm pixel spacing of M512) to a 100 μm x 100 μm high resolution dose scoring grid applied to the entire silicon chip.

6.3 Results and Discussion

6.3.1 Perpendicular magnetic field orientation

In Figure 6.5, 6MV photon beam profiles are displayed, comparing M512 to film in the 1.2 T permanent magnet system, for a perpendicular photon-beam-to-magnetic-field orientation. For a normalised distribution, the asymmetry of the field profiles is accurately modelled for the zero air gap M512 configuration as well as the 2 mm air gap configuration. Comparing FWHM and penumbral width measurements for the two dosimeters (M512 - film), agreement to within (0.5 ± 0.2) mm was obtained across the range of square field sizes measured (0.75 cm - 2.25 cm wide). This indicates that the M512 will be appropriate for the collection of normalised beam profiles in its default configuration, with a 2 mm air gap above the silicon chip. However for a 2.9 mm air gap there becomes some visible change to the shoulders of the profile, which become narrowed in comparison to the profiles collected using film.

If the dosimeter is to be calibrated to read out dose per monitor unit, electron return effects occurring in the air gap will affect its response. Figure 6.6 shows a comparison of dose measured with the M512 with variable air gaps and film (with no air gap). A (17.4 ± 6.5)% drop in response of the dosimeter across the central 80% of the field occurs with a 2 mm air gap. For the 0 mm configuration, there is an improvement in response relative to film, however with all experimental errors considered, the response of the dosimeter is (9.0 ± 6.7)% lower. This is in agreement with the trend observed for 0 mm air gap Monte Carlo simulations, presented in chapter 5, for which an 8% dose loss was observed after elimination of the air gap. It is, however, still possible that non-water equivalence of the bolus material and imperfect setup (in terms of contact of the material with the detector) may be the reason for the discrepancy, but the magnitude of error contributed by the material and fit cannot be quantified. The decrease in profile intensity is independent of the field sizes tested, but is expected to be dependent on magnetic field strength, as is demonstrated in chapter 5 using Monte Carlo simulations. The dosimeter should therefore be calibrated for charge to dose conversion in the magnetic field conditions in which it is to be used, as the zero-field calibration will not be transferable.

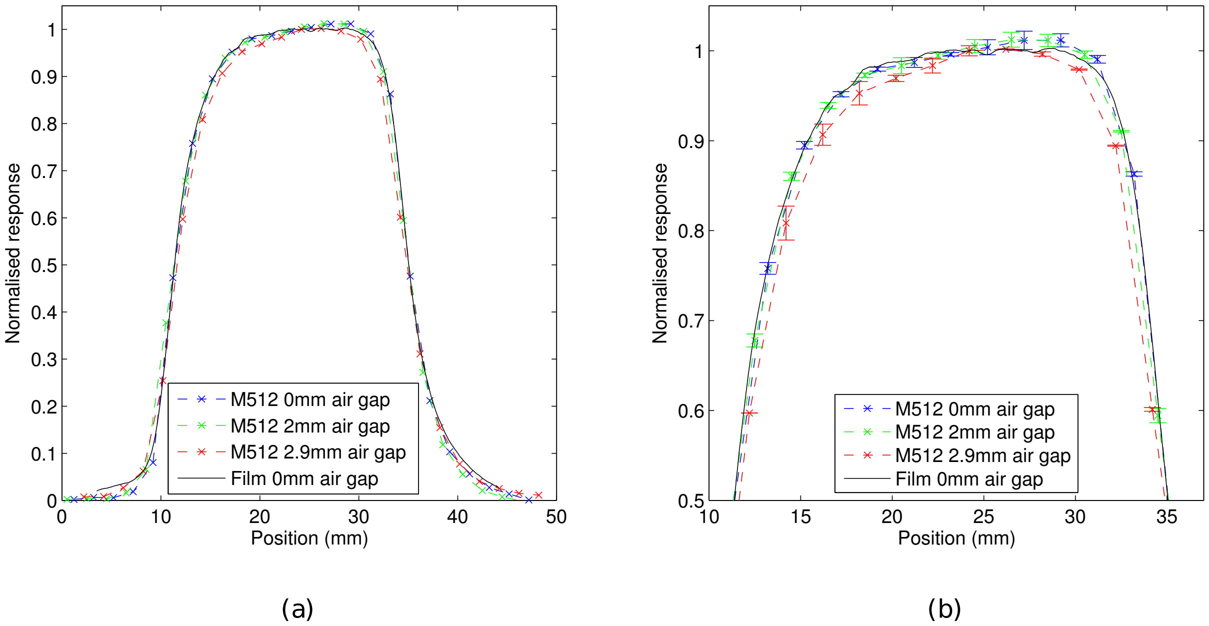

Figure 6.5: M512 field profiles (2.25 cm field size) with varying air gap configurations, compared to profiles collected with EBT3 film (no air gap), measured in the permanent magnet system for a perpendicularly oriented magnetic field of strength 1.2 T. Part (b) is a magnified view of the profiles; error bars reflect 1 standard deviation. The Lorentz force is acting in the left-right direction.

Calibration of the dosimeter requires exposure of the dosimeter under reference conditions; this was not able to be accommodated by the magnet device and thus the theory is unable to be verified at this time.

Figure 6.7 demonstrates the effect of the magnetic field relative to zero field conditions for solid water and solid lung phantoms, as measured by the M512. It is clearly shown that there is asymmetry in the profiles in the presence of the 1.2 T magnetic field. The asymmetry is visibly worse in the lower density lung phantom, and there is also a larger shift in field position (0.2 mm for solid water vs. 1.2 mm for solid lung). The asymmetry extends into the inter umbral region of the profiles in the lung material; this effect is visible, but to a much smaller degree in solid water. The dose gradient across the central 80% of the field width (i.e. in the inter umbral region) is approximately 0.5 %mm^{-1} in water, compared to 1.5 %mm^{-1} in lung.

Table 6.1 includes FWHM and penumbral width (80%-20%) measurements for the profiles displayed in Figure 6.7. The profiles measured in solid lung have wider penumbral widths compared to the profiles measured in solid water in the presence of the magnetic field. The asymmetry in the penumbra is only measurable (in terms of 80%-20% penumbral width) for the 15 mm x 15 mm and 7.5 mm x 7.5 mm field sizes. There is no change to the measured FWHM in lung in the presence of the magnetic field.

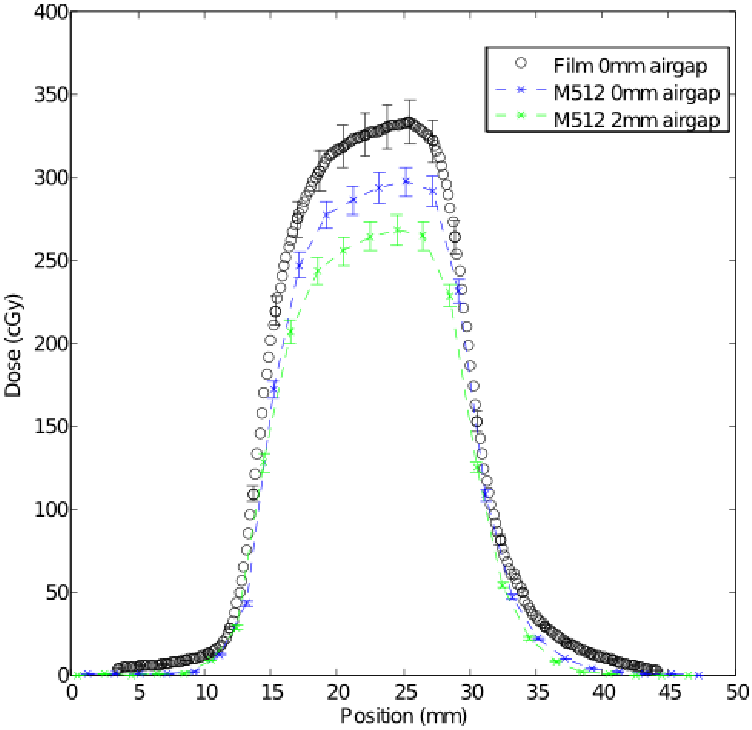

(a) $B_{\perp} = 1.2$ T, 1.5 x 1.5 cm^2

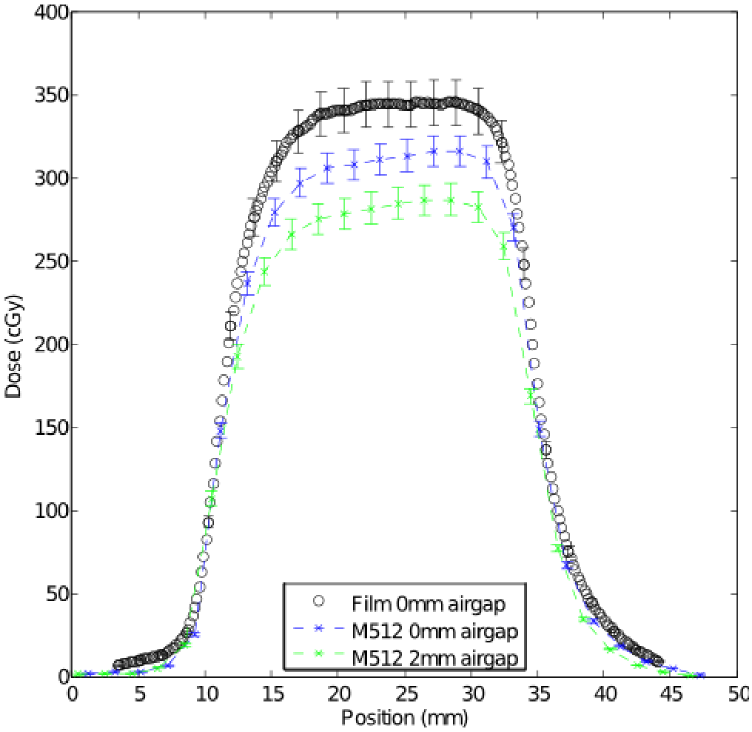

(b) $B_{\perp} = 1.2$ T, 2.25 x 2.25 cm^2

Figure 6.6: Absolute dose response of M512 field profiles with varying air gap configurations, compared to profiles collected with EBT3 film (no air gap), measured in the permanent magnet system for a perpendicularly oriented magnetic field of strength 1.2 T. The drop in dosimetric response as air gap size increases can be attributed to ERE. The Lorentz force is acting in the left-right direction. Error bars reflect ±4% estimated error for film, and ±3% estimated error for M512.

The results presented in Table 6.1 can be compared to simulation data presented in Table 5.1 in chapter 5. Note however the difference in scatter conditions. The Monte Carlo simulation data at 1 T with the M512 dosimeter simulated in a full-scatter water phantom likewise show that there is no change to the measured FWHM in the magnetic field compared to 0 T, as is there no change to the measured (80%-20%) penumbral width above 0.3 mm. This validates the trends observed through Monte Carlo simulation in chapter 5 regarding the response of the M512 in perpendicular magnetic fields.

As has been described throughout this thesis, the presence of a perpendicularly oriented magnetic field results in a bias towards laterally-directed dose deposition. The fundamental changes to dose deposition, as demonstrated in chapter 3 for point spread kernels, have here been shown to perpetuate to the divergent beam scenario. The degree of perturbation of the dose spread kernel was earlier shown to increase with decreasing electron density of the medium. The experimental results presented in this section have shown that for open fields, the dose profile demonstrates the same trend in increasing asymmetry with decreasing medium density. This is exacerbated by lateral electron disequilibrium in the small-field setting, where the range of secondary electrons (being of the magnitude of the field width) contribute to the intensified degree of asymmetry in the low density medium. While changes to dose distributions in lung have been demonstrated in the literature[41,42], these may be the first experimentally measured small fields at high-resolution, in a magnetic field.

Table 6.1: Beam profile characteristics as measured by the M512 in solid water and solid lung for the perpendicular magnetic field orientation. All values reported are in mm. PW: Penumbral width (80% - 20%). FWHM: Full width at half maximum. Measured FWHM deviates from the "expected" field size due to jaw positional accuracy, which has a tolerance of ±1 mm at isocentre as specified by AAPM TG142.

	Field size (mm)	Solid 0 T	Water 1.2 T	Solid 0 T	Lung 1.2 T
Left PW (mm)	7.5 x 7.5	2.7	2.8	3.0	2.7
	15 x 15	3.0	3.2	3.7	4.7
	22.5 x 22.5	3.2	3.7	4.1	6.2
Right PW (mm)	7.5 x 7.5	2.8	3.1	3.1	3.7
	15 x 15	3.2	3.6	3.8	5.3
	22.5 x 22.5	3.3	3.7	4.1	6.2
FHWM (mm)	7.5 x 7.5	8.1	8.2	8.8	8.5
	15 x 15	15.8	15.8	16.2	16.0
	22.5 x 22.5	23.3	23.7	23.9	23.8

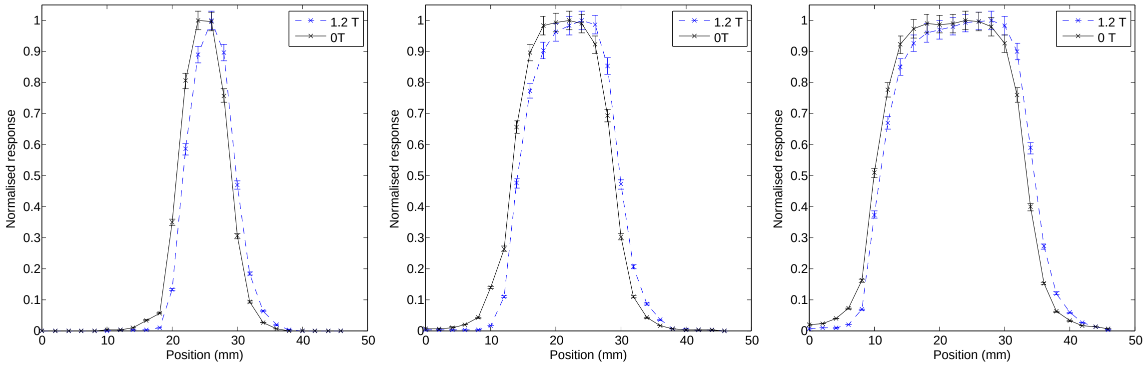

(a) Solid water, $B_\perp$ = 1.2 T, 0.75 x 0.75 cm^2 (b) Solid water, $B_\perp$ = 1.2 T, 1.5 x 1.5 cm^2 (c) Solid water, $B_\perp$ = 1.2 T, 2.25 x 2.25 cm^2

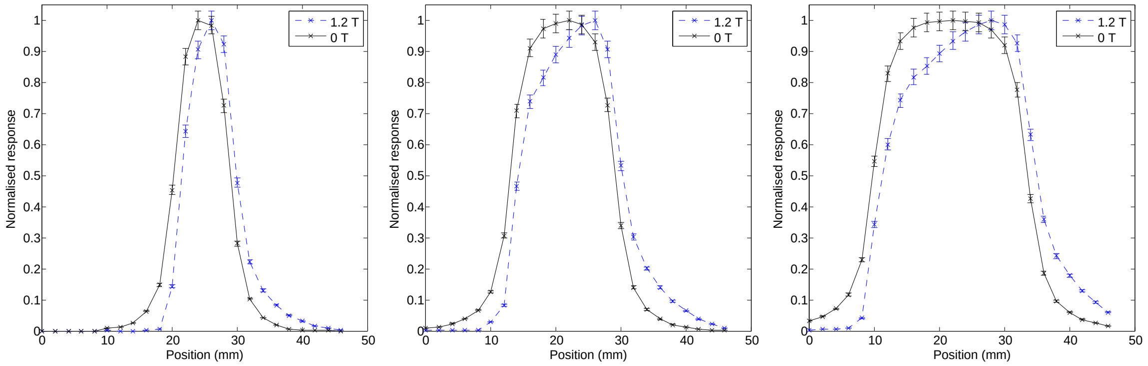

(d) Solid lung, $B_\perp$ = 1.2 T, 0.75 x 0.75 cm^2 (e) Solid lung, $B_\perp$ = 1.2 T, 1.5 x 1.5 cm^2 (f) Solid lung, $B_\perp$ = 1.2 T, 2.25 x 2.25 cm^2

Figure 6.7: M512 measured profiles in solid water, parts (a) - (c), and solid lung, parts (d) - (f), for a perpendicular magnetic field orientation. Profiles measured in 0 T geometry have been included for comparison. The Lorentz force is acting in the left-right direction. Each profile is normalised to the maximum. Error bars reflect ±4% estimated error for film, and ±3% estimated error for M512.

6.3.2 Inline magnetic field orientation

Excellent agreement is seen between film and M512 profiles in the inline magnetic field orientation. Figure 6.8 shows the dose response of the M512 compared to film, which agree within experimental error bounds. For all field sizes the FWHM and penumbral widths measured using the M512 were in agreement to film better than 0.5 mm. These results indicate that a zero field calibration of the dosimeter is adequate for magnetic field applications. Depending on the required dosimetric accuracy, a magnetic field calibration for charge to dose conversion may improve performance. These experiments were performed with the nominal 2 mm air gap above the M512. This indicates that a water-equivalent response of the dosimeter may be obtained without modification of the device to eliminate low-density inhomogeneities. In a broader sense, it also indicates that the use of the dosimeter in solid phantoms is not as sensitive to the presence of small air gaps in the same extreme manner that is the case for the perpendicular orientation.

Table 6.2: Beam profile characteristics as measured by the M512 in solid water and solid lung for the inline magnetic field orientation. All values reported are in mm. PW: Penumbral width (80% - 20%). FWHM: Full width at half maximum. Measured FWHM deviates from the "expected" field size due to jaw positional accuracy, which has a tolerance of ±1 mm at isocentre as specified by AAPM TG142.

	Field size (mm)	Solid 0 T	Water 1.2 T	Solid 0 T	Lung 1.2 T
Left PW (mm)	7.5 x 7.5	3.3	3.2	3.2	3.1
	13.5 x 13.5	3.9	3.7	3.8	3.6
	19.5 x 19.5	4.0	3.7	4.0	3.7
Right PW (mm)	7.5 x 7.5	3.3	3.2	3.2	3.2
	13.5 x 13.5	4.0	3.8	3.9	3.7
	19.5 x 19.5	4.0	3.9	4.2	4.0
FHWM (mm)	7.5 x 7.5	8.3	8.3	8.4	8.1
	13.5 x 13.5	13.8	13.6	13.9	13.6
	19.5 x 19.5	20.1	8.3	20.0	19.5

Beam profiles measured with the M512 in solid water and lung phantoms are displayed in Figure 6.9. Considering the acceptable dosimetric accuracy of the dosimeter relative to film, the magnetic field profiles have been normalised to the response at 0 T. Figure 6.9 parts (a) - (c) show that for an inline 0.95 T magnetic field, the change in dose response is largely unchanged in solid water, with a minor dose enhancement. This is not the case for profiles measured in the solid lung phantom; see parts (d) - (f). The magnetic field profiles show a dose enhancement of (8 ± 6)% at the central axis. The profiles are also visibly narrower at the outer edge of the penumbra, however not to the extent that the 80%-20% width is affected (see Table 6.2). This figure demonstrates experimental evidence to bolster previously reported Monte Carlo simulation results[42] that indicate an inline magnetic field will introduce dose enhancement effects in

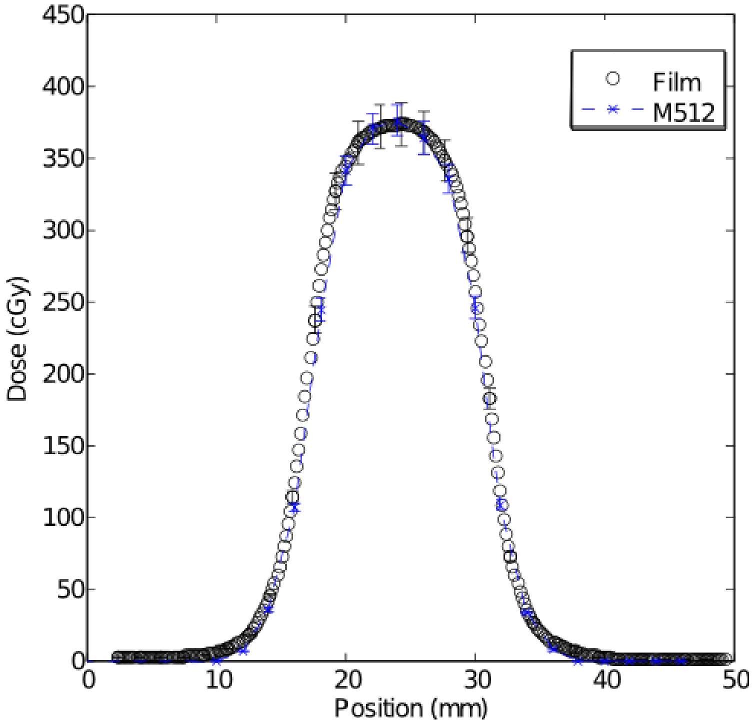

(a) $B_{\|} = 0.95$ T, 1.35 x 1.35 cm^2

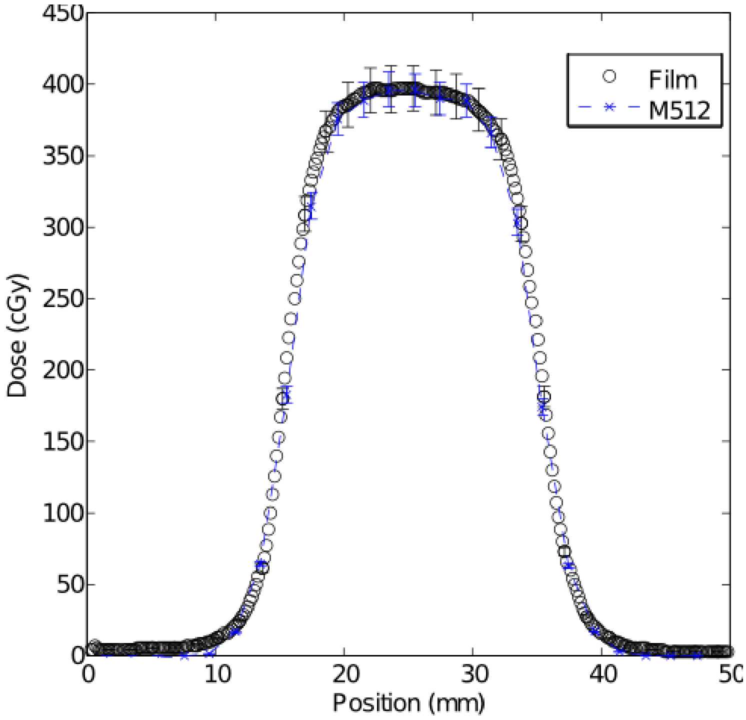

(b) $B_{\|} = 0.95$ T, 1.95 x 1.95 cm^2

Figure 6.8: Absolute dose response of M512 field profiles compared to profiles collected with EBT3 film (no air gap), measured in the permanent magnet system for an inline magnetic field of strength 0.95 T. Error bars reflect ±4% estimated error for film, and ±3% estimated error for M512.

lung.

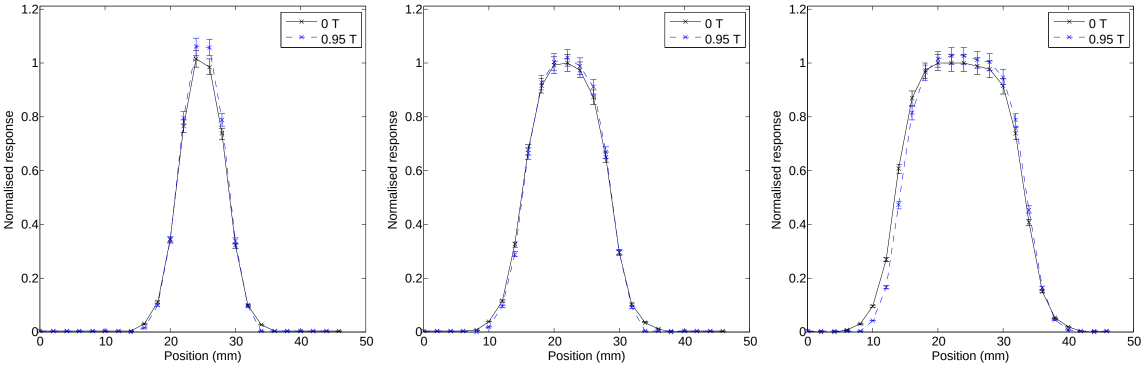

(a) Solid water, $B_{||}$ = 0.95 T, 0.75 x 0.75 cm^2 (b) Solid water, $B_{||}$ = 0.95 T, 1.35 x 1.35 cm^2 (c) Solid water, $B_{||}$ = 0.95 T, 1.95 x 1.95 cm^2

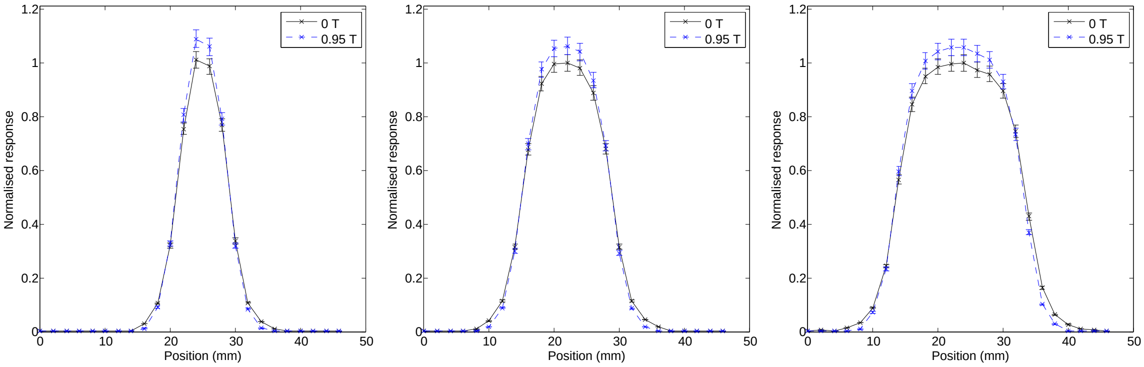

(d) Solid lung, $B_{||}$ = 0.95 T, 0.75 x 0.75 cm^2 (e) Solid lung, $B_{||}$ = 0.95 T, 1.35 x 1.35 cm^2 (f) Solid lung, $B_{||}$ = 0.95 T, 1.95 x 1.95 cm^2

Figure 6.9: M512 measured profiles in solid water, parts (a) - (c), and solid lung, parts (d) - (f), for a perpendicular magnetic field orientation. Profiles measured in 0 T geometry have been included for comparison. Each profile is normalised to the maximum. Error bars reflect ±4% estimated error for film, and ±3% estimated error for M512.

When comparing the results presented in Table 6.2 for solid water to those reported for Monte Carlo simulations in full scatter geometry in chapter 5 (see Table 5.1), the trends observed are validated. The same trend is seen regarding there being no change to the measured FWHM in the magnetic field compared to 0 T, as is there no change to the measured (80%-20%) penumbral width above 0.3 mm.

6.3.3 Applications and Limitations

In the presence of a magnetic field, the M512 dose response differs from that of the zero field case. This is in part due to changes in the dose profiles themselves, and as a consequence of the M512 geometry altering the paths of secondary electrons due to the introduction of non-water equivalent materials. The results presented have demonstrated that the M512 can be used to examine FWHM and penumbral widths of small-field beam profiles, as well as measure dose with a zero-field charge to dose calibration, in the presence of inline magnetic fields. For a perpendicular magnetic field orientation, FWHM and penumbral width can be evaluated accurately using M512. If M512 is to be used for dose measurement in perpendicular magnetic fields, the dosimeter must be calibrated in the magnetic field in which it is to be used; otherwise, normalised distributions must be used. It is advisable to seek a practical solution to resolving the air gap above the dosimeter when used in the perpendicular magnetic field orientation. A bolus/gel material has shown to be a reasonable option, however depositing a layer of non-conductive gel directly on the dosimeter that acts to both fill the air gap as well as protect the silicon layer and associated electric contacts is a more robust solution. This will require special manufacture, and is an area for future development of the technology.

6.4 Conclusion

Experimental measurements show the M512 to be a promising option for use in MRI-linac systems as a high-resolution array dosimeter for small photon field applications. Considering the larger pitch of most commercial 2D array dosimeters, the M512 is an advancement on alternate methods of real-time small field beam profile measurement. The system has demonstrated capability for FWHM and penumbral width measurement with agreement to film within 0.5 mm. The nominal 2 mm air gap present above the sensitive layer does not affect the shape of normalised profiles in the magnetic field, however electron return effects in the air gap (specific to the perpendicular magnetic field orientation) affects the absolute response of the dosimeter. The dosimeter may be used without a specific magnetic field calibration in the inline orientation for a 1 T magnetic field strength - as are the conditions at the Australian MRI-linac facility.

Chapter 7

Conclusion

Two detector systems from the Centre for Medical Radiation Physics have been investigated in this thesis. Both detectors are novel in design, using either drop-in or ion implanted technology to create solid state detector systems that are very thin and minimally perturbing, and in the case of M512 provide superior spatial resolution in comparison to commercially available real-time array detector equivalents. This lends them to magnetic field applications, where array detectors will play an important role in assessing magnetically-induced field profile changes. For example, they are foreseen to be used for QA activities that can be performed in-phantom, such as beam profile constancy measurement. This could reduce the frequency of use of scanning water tanks, which are cumbersome to set up.

Following are the key results of this thesis, stated in terms of the aims:

Aim 1: Compare dose spread array distributions for a combination of magnetic field orientations and strengths, as well as in different media.

Chapter 3 reports on the changes to dose spread arrays to evaluate, in the most fundamental sense, the consequence of changes to secondary electron trajectories and hence dose deposition patterns in magnetic fields. The simulations showed that for inline magnetic fields, dose kernels are minimally affected in water and silicon mediums, for field strengths up to 3 T. Changes were much more sensitive in low density media, with kernels in lung (density $\rho = 0.217$ g/cm^3) showing strong narrowing of the dose distribution in the direction of the primary beam. Kernels narrowed by up to (6.1 ± 0.3) mm at the 0.03% isodose line at 3 T. In the perpendicular orientation, a lateral dose shift and compressed distribution was seen, agreeing with similar simulations that have been previously reported for water in the literature[31]. Maximal lateral displacements of (1.8 ± 0.3) mm, (4.8 ± 0.3) mm and (10.5 ± 0.3) mm at 3 T were seen at the 0.03% isodose line for silicon, water and lung respectively. These results are important to provide context to those presented in the following chapters, where these materials are encountered in the various geometries investigated.

Aim 2: Use a Monte Carlo model of silicon array dosimeters designed by CMRP to model their radiation response.

Chapter 4 characterises the water-equivalence of the response of the MagicPlate-121 array dosimeter in magnetic fields via Monte Carlo simulation. Phase-space files characteristic of a clinical linear accelerator, and possessing divergent beam geometry, were employed. Dose maps of the device simulated in a water phantom geometry were compared to homogeneous water geometry; an approach that separates magnetic-field induced changes from detector-based changes. Dose distributions collected with the detector were shown to agree to within 2% of water response for the inline orientation. For the perpendicular orientation there was some disagreement in the penumbral regions of open fields, of the order of 5%. This is due to the relative contributions of low-energy electrons at the edge of field, which have a tighter axis of rotation about the magnetic field vector and hence higher population density relative to the 0 T case. This caused exaggerated dose enhancement in the high-density silicon pixels, which is possibly due to an increase in the silicon-water mass collisional stopping power ratio at low electron energies. When simulating an IMRT field, the detector demonstrated a water equivalent response to within ±2% in field, indicating these edge of field discrepancies do not perpetuate errors in-field in a dynamic scenario, where there is effective superposition of individual MLC segments.

A next-generation detector named the MagicPlate-512, which has a monolithic silicon construction designed for small field applications has been investigated using Monte Carlo simulations in chapter 5. The detector was found to measure full-width-at-half-maximum and penumbral width with an accuracy exceeding 0.5 mm. ERE was investigated in terms of its impact on the dosimeters response when there was a 2 mm air gap above the detector. The 2 mm air gap is ordinarily incorporated into the dosimeters geometry to correct the over-response characteristic of silicon detectors in 0 T conditions. In the perpendicular orientation, ERE resulted in a decrease in response of up to 23% for 1 T and 57% for 3T. Consequences of the air gap were further investigated in chapter 6, where practically applicable solutions to resolving the air gap were applied experimentally, and their impact on improving dose response was assessed.

Aim 3: Experimentally assess the radiation response of a high resolution silicon array dosimeter in a custom designed permanent magnet system.

The simulation results of the M512 were experimentally verified in chapter 6 using a custom-designed permanent magnet device compatible with a clinical linear accelerator. Sub-millimetre accuracy for full-width-at-half-maximum and penumbral width measurement was achievable with respect to water, which in most cases exceeded an accuracy of 0.5 mm. The detector can be used to assess the features of normalised dose profiles in both inline and perpendicular orientations without specific magnetic field modification, for a 1 T field strength (such as that of the prototype MRI-linac currently under installation in Australia). It is expected to be a valuable device for beam profile monitoring applications, particularly considering its superior spatial resolution compared to commercially available real-time array detectors.

The effect of an air gap above the M512 detector on its dosimetric response was experimentally investigated, in addition to Monte Carlo simulation, in chapter 6. The presence of the air gap above the detector was inconsequential for the inline magnetic field orientation at 1 T. In the perpendicular orientation, the detector response decreased with increasing gap size around the detector, due to ERE. Gel bolus was used as a fill material in the air recess, as a stopgap to a more permanent solution.

7.0.1 Future work

It is recommended for future work that a permanent solution be sought to resolve the air gap that exists above the sensitive layer of the dosimeters. This is important for applications where the dosimeter is used in the perpendicular orientation. Experimental results indicate that in the inline orientation the dosimeters can be used in their current form (i.e. with air gap).

The experimental verification presented in this thesis is somewhat limited in terms of the phantom geometry the magnetic apparatus can accommodate. While the conditions are sufficient to draw conclusions as to the accuracy of profile measurements in a magnetic field, as was the aim of this thesis, experiments should be repeated in full-phantom geometry at a true MRI-linac facility.

The permanent magnet system used for the experimental measurements reported in this thesis is compact, and therefore significant modification to the cabling connecting the dosimeter to readout electronics was not required to distance them from the magnetic field. It is likely a solution will need to be sought when using the dosimeters in a MRI-linac facility to further extend the electronics from the detector elements. A new flexible carrier and electronics packaging has been designed as part of this process.

An even higher resolution detector is also in the prototype stage, which improves upon the 2 mm resolution of the M512 to offer 200 μm resolution along the primary beam axes.

Finally, it is conceptualised that the CMRP dosimetry systems will be used in MRI-linacs for “dynamic dosimaging” applications, as proposed by Metcalfe et al[126], whereby integral dose maps are acquired and processed in real time while the detector array moves in a temporal and spatial pattern that mimics the target (tumour) volume. This would be used to validate dynamic tracking dose deliveries, e.g. MRI-guided MLC tracking[72,127].

Bibliography

[1] M. Barton, S. Jacob, J. Shafiq, K. H. W. Wong, S. Thompson, G. Delaney, and T. Hanna, “Review of optimal radiotherapy utilisation rates,” tech. rep., Ingham Institute for Applied Medical Research and CCORE, 2013.

[2] D. G. Mitchell, B. Snyder, F. Coakley, C. Reinhold, G. Thomas, M. Amendola, L. H. Schwartz, P. Woodward, H. Pannu, and H. Hricak, “Early invasive cervical cancer: tumor delineation by magnetic resonance imaging, computed tomography, and clinical examination, verified by pathologic results, in the acrin 6651/gog 183 intergroup study,” *Journal of Clinical Oncology*, vol. 24, pp. 5687–5694, 2006.

[3] J. M. Edmund and T. Nyholm, “A review of substitute ct generation for mri-only radiation therapy,” *Radiation Oncology*, vol. 12, no. 28, 2017.

[4] J. Dowling, J. Lambert, J. Parker, O. Salvado, J. Fripp, A. Capp, C. Wratten, J. W. Denham, and P. B. Greer, “An atlas-based electron density mapping method for magnetic resonance imaging (mri)-alone treatment planning and adaptive mri-based prostate radiation therapy,” *International Journal of Radiation Oncology Biology Physics*, vol. 83, no. 1, pp. e5–e11, 2012.

[5] J. Uh, T. E. Merchant, Y. Li, X. Li, and C. Hua, “Mri-based treatment planniing with pseudo ct generated through atlas registration,” *Medical Physics*, vol. 41, no. 5, 2014.

[6] P. Metcalfe, G. P. Liney, L. Holloway, A. Walker, M. Barton, G. P. Delaney, S. Vinod, and W. Tome, “The potential for an enhanced role for mri in radiation therapy treatment planning,” *Technology in Cancer Research and Treatment*, vol. 12, no. 5, pp. 429–446, 2013.

[7] A. Walker, G. Liney, P. Metcalfe, and L. Holloway, “Mri distortion: considerations for mri based radiotherapy treatment planning,” *Australas. Phys. Eng. Sci. Med.*, vol. 37, no. 1, pp. 103–113, 2014.

[8] K. Huang, Y. Cao, U. Baharom, and J. M. Balter, “Phantom-based characterization of distortion on a magnetic resonance imaging simulator for radiation oncology,” *Physics in Medicine and Biology*, vol. 61, no. 2, 2016.

[9] J. S. Ginn, N. Agazaryan, M. Cao, U. Baharom, D. A. Low, Y. Yang, Y. Gao, P. Hu, P. Lee, and J. M. Lamb, "Characterization of spatial distortion in a 0.35 t mri-guided radiotherapy system," *Physics in Medicine and Biology*, vol. 62, no. 11, 2017.

[10] S. Hissoiny, B. Ozell, H. Bouchard, and P. Despres, "Gpumcd: A new gpu-oriented monte carlo dose calculation platform," *Medical Physics*, vol. 38, no. 2, pp. 754–764, 2011.

[11] G. H. Bol, S. Hissoiny, J. J. W. Lagendijk, and B. W. Raaymakers, "Fast online monte carlo-based imrt planning for the mri linear accelerator," *Physics in Medicine and Biology*, vol. 57, no. 5, 2012.

[12] C. Kontaxis, G. H. Bol, J. J. W. Lagendijk, and B. W. Raaymakers, "Towards adaptive imrt sequencing for the mr-linax," *Physics in Medicine and Biology*, vol. 60, no. 6, 2015.

[13] C. Kontaxis, G. H. Bol, B. Stemkens, M. Glitzner, F. M. Prins, L. G. W. Kerkmeijer, J. J. W. Lagendijk, and B. W. Raaymakers, "Towards fast online intrafraction replanning for free-breathing stereotactic body radiation therapy with the mr-linac," *Physics in Medicine and Biology*, vol. 62, no. 18, 2017.

[14] J. J. W. Lagendijk, B. W. Raaymakers, C. A. T. V. den Berg, M. A. Moerland, M. E. Philippens, and M. van Vulpen, "Mr guidance in radiotherapy," *Physics in Medicine and Biology*, vol. 59, pp. R349–369, 2014.

[15] D. A. Jaffray, M. C. Carlone, M. F. Milosevic, S. L. Breen, T. Stanescu, A. Rink, H. Alasti, A. Simeonov, M. C. Sweitzer, and J. D. Winter, "A facility for magnetic resonance-guided radiation therapy," *Seminars in Radiation Oncology*, no. 24, pp. 193–195, 2014.

[16] S. Mutic and J. F. Dempsey, "The viewray system: magnetic resonance-guided and controlled radiotherapy," *Seminars in Radiation Oncology*, no. 24, pp. 196–199, 2014.

[17] B. G. Fallone, "The rotating biplanar linac-magnetic resonance imaging system," *Seminars in Radiation Oncology*, vol. 24, pp. 200–202, 2014.

[18] J. J. W. Lagendijk, B. W. Raaymakers, and M. van Vulpen, "The magnetic resonance imaging-linac system," *Seminars in Radiation Oncology*, vol. 24, pp. 207–209, 2014.

[19] C. Printz, "First patients undergo mri-guided radiotherapy," *Cancer*, 2014.

[20] T. Freeman, "First patient treated on the unity mri-linac," May 2017.

[21] P. J. Keall, M. Barton, and S. Crozier, "The australian magnetic resonance imaging-linac program," *Seminars in Radiation Oncology*, no. 24, pp. 203–206, 2014.

[22] ViewRay, "A new generation of treatment delivery performance."

[23] D. M. Santos, J. S. Aubin, B. G. Fallone, and S. Steciw, “Magnetic shielding investigation for a 6 mv in-line linac with the parallel configuration of a linac-mr system,” *Medical Physics*, vol. 39, no. 2, pp. 788–797, 2012.

[24] J. S. Aubin, S. Steciw, and B. G. Fallone, “Magnetic decoupling of the linac in a low field biplanar linac-mr system,” *Medical Physics*, vol. 37, no. 9, pp. 4755–4761, 2010.

[25] D. Constantin, L. Holloway, P. J. Keall, and R. Fahrig, “A novel electron gun for inline mri-linac configurations,” *Medical Physics*, vol. 41, no. 2, pp. 022301–1–10, 2014.

[26] S. Kolling, B. Oborn, and P. Keall, “Impact of the mlc on the mri field distortion of a prototype mri-linac,” *Medical Physics*, vol. 40, no. 12, pp. 121705–1–10, 2013.

[27] B. Burke, A. Ghila, B. G. Fallone, and S. Rathee, “Radiation induced current in the rf coils of integrated linac-mr systems: The effect of buildup and magnetic field,” *Medical Physics*, vol. 39, no. 8, pp. 5004–5014, 2012.

[28] J. Overweg, B. W. Raaymakers, J. J. W. Lagendijk, and K. J. Brown, “System for mri guided radiotherapy,” *Proc Int Soc Magn Reson Med*, vol. 17, p. 594, 2009.

[29] B. W. Raaymakers, J. J. W. Lagendijk, J. Overweg, J. G. M. Kok, A. J. E. Raaijmakers, E. M. Kerkhof, R. W. van der Put, I. Meijsing, S. P. M. Crijns, F. Benedosso, M. van Vulpen, C. H. W. de Graaff, J. Allen, and K. J. Brown, “Integrating a 1.5 t mri scanner with a 6 mv accelerator: proof of concept,” *Physics in Medicine and Biology*, vol. 54, no. 12, p. N229, 2009.

[30] A. F. Bielajew, “The effect of strong longitudinal magneic fields on dose deposition from electrona nd photon beams,” *Medical Physics*, vol. 20, no. 4, pp. 1171–1179, 1993.

[31] A. J. E. Raaijmakers, B. W. Raaymakers, and J. J. W. Lagendijk, “Magnetic-field-induced dose effects in mr-guided radiotherapy systems: dependence on magnetic field strength,” *Physics in Medicine and Biology*, vol. 53, pp. 909–923, January 2008.

[32] A. J. E. Raaijmakers, B. W. Raaymakers, and J. J. W. Lagendijk, “Integrating a mri scanner with a 6 mv radiotherapy accelerator: dose increase at tissue-air interfaces in a lateral magnetic field due to returning electrons,” *Physics in Medicine and Biology*, vol. 50, pp. 1363–1376, March 2005.

[33] B. W. Raaymakers, A. J. E. Raaijmakers, A. N. T. J. Kotte, D. Jette, and J. J. W. Lagendijk, “Integrating a mri scanner with a 6 mv radiotherapy accelerator: dose deposition in a transverse magnetic field,” *Physics in Medicine and Biology*, vol. 49, pp. 4109–4118, 2004.

[34] C. Kirkby, T. Stanescu, and B. G. Fallone, “Patient dosimetry for hybris mri-radiotherapy systems,” *Medical Physics*, vol. 35, no. 3, pp. 1019–1027, 2008.

[35] B. M. Oborn, P. E. Metcalfe, M. J. Butson, and A. B. Rosenfeld, “High resolution entry and exit monte carlo dose calculations from a linear accelerator 6 mv beam under the influence of transverse magnetic fields,” *Medical Physics*, vol. 36, pp. 3549–3559, August 2009.

[36] ICRU, *Determination of dose equivalents resulting from external radiation sources.* ICRU Report 39, Washington DC: ICRU, 1985.

[37] A. J. E. Raaijmakers, B. W. Raaymakers, S. van der Meer, and J. J. W. Lagendijk, “Integrating a mri scanner with a 6 mv radiotherapy accelerator: impact of the surface orientation on the entrance and exit dose due to the transverse magnetic field,” *Physics in Medicine and Biology*, vol. 52, pp. 929–939, 2007.

[38] A. J. E. Raaijmakers, B. Hardemark, B. W. Raaymakers, C. P. J. Raaijmakers, and J. J. W. Lagendijk, “Dose optimization for the mri-accelerator: Imrt in the presence of a magnetic field,” *Physics in Medicine and Biology*, vol. 52, pp. 7045–7054, 2007.

[39] S. W. Ramahi, S. A. Naqvi, and J. Chu, “Achieving a smaller penumbra region for better planning in conformal radiotherapy by using a longitudinal magnetic field,” *Proc. World Congress on Medical Physics and Biomedical Engineering*, 2000.

[40] D. W. Litzenberg, B. A. Fraass, D. L. McShan, T. W. O’Donnell, D. A. Roberts, F. D. Becchetti, A. F. Bielajew, and J. M. Moran, “An apparatus for applying strong longitudinal magnetic fields to clinical photon and electron beams,” *Physics in Medicine and Biology*, vol. 46, pp. N105–N115, 2001.

[41] C. Kirkby, B. Murray, S. Rathee, and B. G. Fallone, “Lung dosimetry in a linac-mri radiotherapy unit with a longitudinal magnetic field,” *Medical Physics*, vol. 37, no. 9, pp. 4722–4732, 2010.

[42] B. M. Oborn, Y. Ge, N. Hardcastle, P. E. Metcalfe, and P. J. Keall, “Dose enhancement in radiotherapy of small lung tumors using inline magnetic fields: A monte carlo based planning study,” *Medical Physics*, vol. 43, no. 1, pp. 368–377, 2016.

[43] B. M. Oborn, P. E. Metcalfe, M. J. Butson, A. B. Rosenfeld, and P. J. Keall, “Electron contamination modeling and skin dose in 6 mv longitudinal field mrigrt: Impact of the mri and mri fringe field,” *Medical Physics*, vol. 39, no. 2, pp. 874–890, 2012.

[44] A. Keyvanloo, B. Burke, B. Warkentina, T. Tadic, S. Rathee, C. Kirkby, D. M. Santos, and B. G. Fallone, “Skin dose in longitudinal and transverse linac-mris using monte carlo and realistic 3d mri field models,” *Medical Physics*, vol. 39, no. 10, pp. 6509–6521, 2012.

[45] B. M. Oborn, M. Williams, M. Bailey, and M. G. Carolan, “Imrt treatment monitor unit verification using absolute calibrated beamnrc and geant4 monte carlo simulations,” *Journal of Physics: Conference Series*, vol. 489, no. 1, p. 012020, 2014.

[46] F. Khan, *The physics of radiation therapy.* Lippincott Williams and Wilkins, 2010.

[47] IAEA, “The use of plane-parallel ionization chambers in high-energy electron and photon beams. an international code of practice for dosimetry,” Technical Report Series 381, IAEA, Vienna, 1997.

[48] I. Meijsing, B. W. Raaymakers, A. J. E. Raaijmakers, J. G. M. Kok, L. Hogeweg, B. Liu, and J. J. W. Lagendijk, “Dosimetry for the mri accelerator: the impact of a magnetic field on the response of a farmer ne2571 ionization chamber,” *Physics in Medicine and Biology*, vol. 54, pp. 2993–3002, April 2009.

[49] K. Smit, B. van Asselen, J. G. M. Kok, A. H. L. Aalbers, J. J. W. Lagendijk, and B. W. Raaymakers, “Towards reference dosimetry for the mr-linac: magnetic field correction of the ionization chamber reading,” *Physics in Medicine and Biology*, vol. 58, pp. 5945–5957, August 2013.

[50] D. J. O’Brien, J. Dolan, S. Pencea, N. Schupp, and G. O. Sawakuchi, “Relative dosimetry with an mr-linac: Response of ion chambers, diamond, and diode detectors for off-axis, depth dose, and output factor measurements,” *Medical Physics*, 2017.

[51] M. Reynolds, B. G. Fallone, and S. Rathee, “Dose response of selected ion chambers in applied homogeneous transverse and longitudinal magnetic fields,” *Medical Physics*, vol. 40, no. 4, pp. 042102–4 – 042102–7, 2013.

[52] K. Smit, J. G. M. Kok, J. J. W. Lagendijk, and B. W. Raaymakers, “Performance of a multi-axis ionization chamber array in a 1.5 t magnetic field,” *Physics in Medicine and Biology*, vol. 59, pp. 1845–1855, March 2014.

[53] V. N. Malkov and D. W. O. Rogers, “Sensitive volume effects on monte carlo calculated ion chamber response in magnetic fields,” *Medical Physics*, vol. 44, no. 9, pp. 4854–4858, 2017.

[54] D. J. O’Brien, D. A. Roberts, G. S. Ibbott, and G. O. Sawakuchi, “Reference dosimetry in magnetic fields: formalism and ionization chamber correction factors,” *Medical Physics*, vol. 43, no. 8, pp. 4915–4927, 2016.

[55] S. L. Hackett, B. van Asselen, J. W. H. Wolthaus, J. G. M. Kok, S. J. Woodings, J. J. W. Lagendijk, and B. W. Raaymakers, “Consequences of air around an ionisation chamber: are existing solid phantoms suitable for reference dosimetry on an mr-linac,” *Medical Physics*, vol. 43, no. 7, pp. 3961–3968, 2016.

[56] D. J. O'Brien and G. O. Sawakuchi, "Monte carlo study of the chamber-phantom air gap effect in a magnetic field," *Medical Physics*, vol. 44, no. 7, 2017.

[57] J. P. Agnew, F. O'Grady, R. Young, S. Duane, and G. Budgell, "Quantification of static magnetic field effects on radiotherapy ionization chambers," *Physics in Medicine and Biology*, vol. 62, no. 5, p. 1731, 2017.

[58] P. Mayles, A. Nahum, and J. Rosenwald, *Handbook of Radiotherapy Physics: Theory and Practice.* Taylor and Francis Group, 2007.

[59] K. Eklund, *Modelling Silicon Diode Response in Radiotherapy Fields using Fluence Pencil Beams.* PhD thesis, Uppsala University, Faculty of Medicine, 2010.

[60] G. Rikner and E. Grussel, "Effect of radiation damage on p-type silicon detectors," *Physics in Medicine and Biology*, vol. 28, pp. 1261–1267, 1983.

[61] M. Reynolds, B. G. Fallone, and S. Rathee, "Dose response of selected solid state detectors in applied homogeneous transverse and longitudinal magnetic fields," *Medical Physics*, vol. 41, August 2014.

[62] H. H. Li, V. L. Rodriguez, O. L. Green, Y. Hu, R. Kashani, O. Wooten, D. Yang, and S. Mutic, "Patient specific quality assurance for the delivery of (60)co intensity modulated radiation therapy subject to a 0.35 t lateral magnetic field," *International Journal of Radiation Oncology Biology Physics*, vol. 91, pp. 66–72, 2015.

[63] S. T. Ellefson, W. S. Culberson, B. P. Bednarz, L. A. DeWerd, and J. E. Bayouth, "An analysis of the arccheck-mr diode array's performance for viewray quality assurance," *Journal of Applied Clinical Medical Physics*, vol. 18, no. 4, pp. 161–171, 2017.

[64] A. C. Houweling, J. H. W. de Vries, J. Wolthaus, S. Woodings, J. G. M. Kok, B. van Asselen, K. Smit, A. Bel, J. J. W. Lagendijk, and B. W. Raaymakers, "Performance of a cylindrical diode array for use in a 1.5 t mr-linac," *Physics in Medicine and Biology*, vol. 61, pp. N80–N89, 2016.

[65] J. H. D. Wong, I. Fuduli, M. Carolan, M. Petasecca, M. L. F. Lerch, V. L. Perevertaylo, P. Metcalfe, and A. B. Rosenfeld, "Characterization of a novel two dimensional diode array the "magic plate" as a radiation detector for radiation therapy treatment," *Medical Physics*, vol. 39, pp. 2544–2558, May 2012.

[66] A. Espinoza, B. Beeksma, M. Petasecca, I. Fuduli, C. Porumb, D. Cutajar, S. Corde, M. Jackson, M. L. F. Lerch, and A. B. Rosenfeld, "The feasibility study and characterisation of a two-dimensional diode array in "magic phantom" for high dose rate brachytherapy quality assurance," *Medical Physics*, vol. 40, pp. 111702–1–10, 2013.

[67] A. Espinoza, M. Petasecca, I. Fuduli, A. Howie, J. Bucci, S. Corde, M. Jackson, M. L. F. Lerch, and A. B. Rosenfeld, “The evaluation of a 2d diode array in ”magic phantom” for use in high dose rate brachytherapy pretreatment quality assurance,” *Medical Physics*, vol. 42, no. 2, pp. 663–673, 2015.

[68] I. Fuduli, M. Newall, A. Espinoza, C. Porumb, M. Carolan, M. Lerch, P. Metcalfe, A. Rosenfeld, and M. Petasecca, “Multichannel data acquisition system comparison for quality assurance in external beam radiation therapy,” *Radiation Measurements*, vol. 71, pp. 338–341, 2014.

[69] I. Fuduli, C. Porumb, A. Espinoza, A. Aldosari, M. Carolan, M. L. F. Lerch, P. Metcalfe, A. B. Rosenfeld, and M. Petasecca, “A comparative analysis of multichannel data acquisition systems for quality assurance in external beam radiation therapy,” *Journal of Instrumentation*, vol. 9, p. T06003, 2014.

[70] A. H. Aldosari, M. Petasecca, A. Espinoza, M. Newall, I. Fuduli, C. Porumb, S. Alshaikh, Z. A. Alrowaili, M. Weaver, P. Metcalfe, M. Carolan, M. L. F. Lerch, V. Perevertaylo, and A. B. Rosenfeld, “A two dimensional silicon detectors array for quality assurance in stereotactic radiotherapy: Magicplate-512,” *Medical Physics*, vol. 41, pp. 091707–1, 2014.

[71] N. Stansook, K. Utitsarn, M. Petasecca, M. K. Newall, M. Duncan, K. Nitschke, M. Carolan, P. Metcalfe, M. L. F. Lerch, V. L. Perevertaylo, W. A. Tome, and A. B. Rosenfeld, “Angular dependence of a 2d monolithic silicon diode array for small field dosimetry,” *Medical Physics*, vol. 44, no. 8, pp. 4313–4321, 2017.

[72] M. Petasecca, M. K. Newall, J. T. Booth, M. Duncan, A. H. Aldosari, I. Fuduli, A. A. Espinoza, C. S. Porumb, S. Guatelli, P. Metcalfe, E. Colvill, D. Cammarano, M. Carolan, B. Oborn, M. L. F. Lerch, V. L. Perevertaylo, P. J. Keall, and A. B. Rosenfeld, “Magicplate-512: A 2d silicon detector array for quality assurance of stereotactic motion adaptive radiotherapy,” *Medical Physics*, vol. 42, no. 6, pp. 2992–3004, 2015.

[73] M. J. Williams and P. E. Metcalfe, “Radiochromic film dosimetry and its applications in radiotherapy,” *AIP Conference Proceedings*, vol. 1345, pp. 75–99, 2011.

[74] M. J. Butson, P. K. N. Yu, T. Cheung, and P. E. Metcalfe, “Radiochromic film for radiation dosimetry,” *Materials Science and Engineering: Reports*, vol. 41, pp. 61–120, 2003.

[75] N. Suchowerska, P. Hoban, M. Butson, A. Davision, and P. Metcalfe, “Directional dependence in film dosimetry: radiographic and radiochromic film,” *Physics in Medicine and Biology*, vol. 46, no. 5, pp. 1391–1397, 2001.

[76] L. J. van Battum, D. Hoffmans, H. Piersma, and S. Heukelom, “Accurate dosimetry with gafchromic ebt film of a 6mv photon beam in water: What level is achievable?,” *Medical Physics*, vol. 35, no. 2, pp. 704–716, 2008.

[77] B. D. Lynch, J. Kozelka, M. K. Ranade, J. G. Li, W. E. Simon, and J. F. Dempsey, “Important considerations for radiochromic film dosimetry with flatbed ccd scanners and ebt gafchromic film,” *Medical Physics*, vol. 33, no. 12, pp. 4551–4556, 2006.

[78] M. J. Butson and T. Cheung, “Scanning orientation effects on gafchromic ebt film dosimetry,” *Australas. Phys. Eng. Sci. Med.*, vol. 29, no. 3, pp. 281–284, 2006.

[79] S. Reinhardt, M. Hillbrand, J. J. Wilkens, and W. Assman, “Comparison of gafchromic ebt2 and ebt3 films for clinical photon and proton beams,” *Medical Physics*, vol. 39, no. 8, pp. 5257–5262, 2012.

[80] P. Lindsay, A. Rink, M. Muschin, and D. Jaffray, “Investigation of energy dependence of ebt and ebt-2 gafchromic film,” *Medical Physics*, vol. 37, no. 2, pp. 571–576, 2010.

[81] S. Devic, J. Seuntjens, E. Sham, E. B. Podgorsak, C. R. Schmidtlein, A. S. Kirov, and C. G. Soares, “Precise radiochromic film dosimetry using a flat-bed document scanner,” *Medical Physics*, vol. 32, no. 7, pp. 2245–2253, 2005.

[82] L. Paelinck, W. D. Neve, and C. D. Wagter, “Precautions and strategies in using a commercial flatbed scanner for radiochromic film dosimetry,” *Physics in Medicine and Biology*, vol. 52, no. 1, pp. 231–242, 2007.

[83] S. Saur and J. Frengen, “Gafchromic ebt film dosimetry with flatbed ccd scanner: a novel background correction method and full dose uncertainty analysis,” *Medical Physics*, vol. 35, no. 7, pp. 3094–3101, 2008.

[84] S. Devic, Y. Z. Wang, N. Tomic, and E. B. Podgorsak, “Sensitivity of linear ccd array nased film scanners used for film dosimetry,” *Medical Physics*, vol. 33, no. 11, pp. 3993–3996, 2006.

[85] L. Menegotti, A. Delana, and A. Martignano, “Radiochromic film dosimetry with flatbed scanners: a fast and accurate method for dose calibration and uniformity correction with single exposure film,” *Medical Physics*, vol. 35, no. 7, pp. 3078–3085, 2008.

[86] H. Miras and R. Arrans, “An easy method to account for light scattering dose dependence in radiochromic films,” *Medical Physics*, vol. 36, no. 9, pp. 3866–3869, 2009.

[87] J. F. Dempsey, D. A. Low, S. Mutic, J. Markman, A. S. Kirov, G. H. Nussbaum, and J. F. Williamson, “Validation of a precision radiochromic film dosimetry system for quantitative two-dimensional imaging of acute exposure dose distributions,” *Medical Physics*, vol. 27, no. 10, pp. 2462–2475, 2000.

[88] A. Rink, I. A. Vitkin, and D. A. Jaffray, "Characterization and real-time optical measurements of the ionizing radiation dose response for a new radiochromic medium," *Medical Physics*, vol. 32, no. 8, pp. 2510–2516, 2005.

[89] W. L. McLaughlin, J. M. Puhl, M. Al-Sheikhly, C. A. Christou, A. Miller, A. Kovacs, L. Wojnarovits, and D. F. Lewis, "Novel radiochromic films for clinical dosimetry," *Radiation Protection Dosimetry*, vol. 66, pp. 263–268, 1996.

[90] I. Ali, C. Costescu, M. Vicic, J. F. Dempsey, and J. F. Williamson, "Dependence of radiochromic film optical density post-exposure kinetics on dose and dose fractionation," *Medical Physics*, vol. 30, no. 8, pp. 1958–1967, 2003.

[91] C. M. Ma, E. Mok, A. Kapur, T. Pawlicki, D. Findley, S. Brain, K. Forester, and A. L. Boyer, "Clinical implementation of a monte carlo treatment planning system," *Medical Physics*, vol. 26, pp. 2133–2143, 1999.

[92] M. R. Arnfield, C. H. Siantar, J. V. Siebers, P. Garmon, L. Cox, and R. Mohan, "The impact of electron transport on the accuraacy of computed dose," *Medical Physics*, vol. 27, pp. 1266–1274, 2000.

[93] T. Krieger and O. A. Sauer, "Monte carlo- versus pencil-beam-/collapsed-cone-dose calculation in a heterogeneous multi-layer phantom," *Physics in Medicine and Biology*, vol. 50, pp. 859–868, 2005.

[94] L. Paelinck, N. Reynaert, H. Thierens, W. D. Neve, and C. D. Wagter, "Experimental verification of lung dose with radiochromic film: comparison with monte carlo simulations and commercially available treatment planning systems," *Physics in Medicine and Biology*, vol. 50, pp. 2055–2069, 2005.

[95] S. Agostinelli, J. Allison, K. Amako, J. Apostolakis, H. Araujo, P. Arce, M. Asai, D. Axen, S. Banerjee, G. Barrand, F. Behner, L. Bellagamba, J. Boudreau, L. Broglia, A. Brunengo, H. Burkhardt, S. Chauvie, J. Chuma, R. Chytracek, G. Cooperman, G. Cosmo, P. Degtyarenko, A. Dell'Acqua, G. Depaola, D. Dietrich, R. Enami, A. Feliciello, C. Ferguson, H. Fesefeldt, G. Folger, F. Foppiano, A. Forti, S. Garelli, S. Giani, R. Giannitrapani, D. Gibin, J. G. Cadenas, I. González, G. G. Abril, G. Greeniaus, W. Greiner, V. Grichine, A. Grossheim, S. Guatelli, P. Gumplinger, R. Hamatsu, K. Hashimoto, H. Hasui, A. Heikkinen, A. Howard, V. Ivanchenko, A. Johnson, F. Jones, J. Kallenbach, N. Kanaya, M. Kawabata, Y. Kawabata, M. Kawaguti, S. Kelner, P. Kent, A. Kimura, T. Kodama, R. Kokoulin, M. Kossov, H. Kurashige, E. Lamanna, T. Lampén, V. Lara, V. Lefebure, F. Lei, M. Liendl, W. Lockman, F. Longo, S. Magni, M. Maire, E. Medernach, K. Minamimoto, P. M. de Freitas, Y. Morita, K. Murakami, M. Nagamatu, R. Nartallo, P. Nieminen, T. Nishimura, K. Ohtsubo, M. Okamura, S. O'Neale, Y. Oohata,

K. Paech, J. Perl, A. Pfeiffer, M. Pia, F. Ranjard, A. Rybin, S. Sadilov, E. D. Salvo, G. Santin, T. Sasaki, N. Savvas, Y. Sawada, S. Scherer, S. Sei, V. Sirotenko, D. Smith, N. Starkov, H. Stoecker, J. Sulkimo, M. Takahata, S. Tanaka, E. Tcherniaev, E. S. Tehrani, M. Tropeano, P. Truscott, H. Uno, L. Urban, P. Urban, M. Verderi, A. Walkden, W. Wander, H. Weber, J. Wellisch, T. Wenaus, D. Williams, D. Wright, T. Yamada, H. Yoshida, and D. Zschiesche, "Geant4—a simulation toolkit," *Nuclear Instruments and Methods in Physics Research Section A: Accelerators, Spectrometers, Detectors and Associated Equipment*, vol. 506, no. 3, pp. 250 – 303, 2003.

[96] D. W. O. Rogers, B. A. Faddegon, G. X. Ding, C. M. Ma, J. We, and T. R. Mackie, "Beam: A monte carlo code to simulate radiotherapy treatment units," *Medical Physics*, vol. 22, no. 5, pp. 503–524, 1995.

[97] R. Loevinger, "Distribution of absorbed energy around a point source of beta radiation," *Science*, vol. 112, pp. 530–531, 1950.

[98] R. Loevinger, "The dosimetry of beta sources in tissue: the point source function," *Radiology*, vol. 66, pp. 55–62, 1956.

[99] A. Ahnesjo and M. M. Aspradakis, "Dose calculations for external photon beams in radiotherapy," *Physics in Medicine and Biology*, vol. 44, no. R99-R155, 1999.

[100] T. R. Mackie, J. W. Scrimger, and J. J. Battista, "A convolution method of calculating dose for 15-mv x rays," *Medical Physics*, vol. 12, pp. 188–196, 1985.

[101] R. Mohan, C. Chui, and L. Lidofsky, "Differential pencil beam dose computation model for photons," *Medical Physics*, vol. 13, pp. 64–73, 1986.

[102] A. Ahnesjo and T. R. Mackie, "Analytical description of monte carlo generated photon dose convolution kernels," in *IX ICCR (Scheveningen, The Netherlands)*, 1987.

[103] T. R. Mackie, A. F. Bielajew, D. W. O. Rogers, and J. J. Battista, "Generation of photon energy deposition kernels using the egs monte carlo code," *Physics in Medicine and Biology*, vol. 33, pp. 1–20, 1988.

[104] A. Ahnesjo, "Collapsed cone convolution of radiant energy for photon dose calculation in heterogeneous media," *Medical Physics*, vol. 16, pp. 577–592, 1989.

[105] A. Ahnesjo, M. Saxner, and A. Trepp, "A pencil beam model for photon dose calculation," *Medical Physics*, vol. 19, pp. 263–273, 1992.

[106] A. L. Boyer and E. C. Mok, "A photon dose distribution model employing convolution calculations," *Medical Physics*, vol. 12, pp. 169–177, 1985.

[107] A. Ahnesjo, P. Andreo, and A. Brahme, "Calculaiton and application of point spread functions for treatmet planning with high energy photon beams," *Acta Oncology*, vol. 26, pp. 49–56, 1987.

[108] T. Han, J. K. Mikell, M. Salehpour, and F. Mourtada, "Dosimetric comparison of acuros xb deterministic radiation transport method with monte carlo and model-based convolution methods in heterogeneous media," *Medical Physics*, vol. 38, no. 5, pp. 2651–2664, 2011.

[109] S. Hissoiny, A. J. Raaijmakers, B. Ozell, P. Despres, and B. W. Raaymakers, "Fast dose calculation in magnetic fields with gpumcd," *Physics in Medicine and Biology*, vol. 56, no. 16, pp. 5119–5129, 2011.

[110] Geant4 Collaboration, *Geant4 User's Guide for Application Developers*, geant4 10.0 ed., December 2013.

[111] H. Q. Woodard and D. R. White, "The composition of body tissues," *The British Institute of Radiology*, vol. 59, pp. 1209–1218, 1986.

[112] J. V. Dyk, T. J. Keane, and W. D. Rider, "Lung density as measured by computerized tomography: implications for radiotherapy," *International Journal of Radiation Oncology Biology Physics*, vol. 8, pp. 1363–1372, 1982.

[113] H. Nettelbeck, G. J. Takacs, and A. B. Rosenfeld, "Effect of transverse magnetic fields on dose distribution and rbe of photon beams: comparing penelope and egs4 monte carlo codes," *Physics in Medicine and Biology*, vol. 53, pp. 5123–5137, 2008.

[114] H. Nettelbeck, A. B. Rosenfeld, G. J. Takacs, and M. L. F. Lerch, "Magneto-radiotherapy: effect of magnetic fields on dose distribution and rbe," *Australas. Phys. Eng. Sci. Med.*, vol. 28, no. 4, pp. 276–277, 2005.

[115] I. Das, G. Ding, and A. Ahnesjo, "Small fields: Nonequilibrium radiation dosimetry," *Medical Physics*, vol. 35, no. 1, pp. 206–215, 2007.

[116] M. M. Aspradakis, J. Byrne, H. Palmans, J. Conway, K. Rosser, J. Warrington, and S. Duane, "Small field mv photon dosimetry," Tech. Rep. Report Number 103, IPEM, 2010.

[117] H. Bouchard, J. Seuntjens, S. Duane, Y. Kamio, and H. Palmans, "Detector dose response in megavoltage small photon field beams i. theoretical concepts," *Medical Physics*, vol. 42, p. 6033, 2015.

[118] H. Bouchard, Y. Kamio, H. Palmans, J. Seuntjens, and S. Duane, "Detector dose response in megavoltage small photon field beams ii. pencil beam perturbation effects," *Medical Physics*, vol. 42, p. 6048, 2015.

[119] E. Pappas, T. Maris, F. Zacharopoulou, and A. Papadakis, “Small srs photon field profile dosimetry performed using a pinpoint air ion chamber, a diamond detector, a novel silicon-dode array (dosi), and polymer gel dosimetry. analysis and intercomparison,” *Medical Physics*, vol. 35, p. 4640, 2008.

[120] M. Tyler, P. Liu, K. W. Chan, A. Ralston, D. McKenzie, A. Downes, and N. Suchowerska, “Characterisation of small-field stereotactic radiosurgery beams with modern detectors,” *Physics in Medicine and Biology*, vol. 58, pp. 7595–7608, 2013.

[121] J. H. D. Wong, D. Cutajar, M. L. F. Lerch, M. Petasecca, T. Knittel, M. Carolan, V. L. Perevertaylo, P. Metcalfe, and A. B. Rosenfeld, “From hep to medical radiation dosimetry - the silicon strip detector dose magnifying glass,” *Radiation Measurements*, vol. 46, pp. 1615–1618, 2011.

[122] T. S. A. Underwood, J. Thompson, L. Bird, A. J. D. Scott, P. Patmore, H. C. Winter, M. A. Hill, and J. D. Fenwick, “Validation of a prototype diodeair for small field dosimetry,” *Physics in Medicine and Biology*, vol. 60, pp. 2939–2953, 2015.

[123] P. Andreo and H. Benmakhlouf, “Role of the density, density effect and mean excitation energy in solid-state detectors for small photon fields,” *Physics in Medicine and Biology*, vol. 62, pp. 1518–1532, 2017.

[124] A. Niroomand-Rad, C. R. Blackwell, B. M. Coursey, K. P. Gall, J. M. Galvin, W. L. McLaughlin, A. S. Meigooni, R. Nath, J. E. Rodgers, and C. G. Soares, “Radiochromic film dosimetry: Recommendations of aapm radiation therapy committee task group 55,” *Medical Physics*, vol. 25, pp. 2093–2115, 1998.

[125] T. Causer, B. Oborn, M. Gargett, A. B. Rosenfeld, and P. Metcalfe, “Experimental verification of the magnetic field of a new apparatus for performing experiments in mri-linac dosimetry,” in *Engineering and Physical Sciences in Medicine Conference*, 2016.

[126] P. Metcalfe, S. J. Alnaghy, M. Newall, M. Gargett, M. Duncan, G. Liney, J. Begg, B. Oborn, M. Petasecca, M. Lerch, and A. Rosenfeld, “Introducing dynamic dosimaging: potential applications for mri-linac,” *Journal of Physics: Conference Series*, vol. 777, no. 012007, 2017.

[127] P. J. Keall, E. Colvill, R. O’Brien, J. A. Ng, P. R. Poulsen, T. Eade, A. Kneebone, and J. T. Booth, “The first clinical implementation of electromagnetic transponder-guided mlc tracking,” *Medical Physics*, vol. 41, no. 2, 2014.